

Mobility and Translocation of TAT Peptides in Model Membranes

Dissertation
zur
Erlangung des Doktorgrades (Dr. rer. nat)
der
Mathematisch-Naturwissenschaftlichen Fakultät
der
Rheinischen Friedrich-Wilhelms-Universität Bonn

vorgelegt von
Corina Ciobanu
aus
Roman (Rumänien)

Bonn Juni 2010

Angefertigt mit Genehmigung der Mathematisch-Naturwissenschaftlichen Fakultät der
Rheinischen Friedrich-Wilhelms-Universität Bonn

1. Gutachter Prof. Dr. Ulrich Kubitscheck

2. Gutachter Prof. Dr. Beate Klösgen

Tag der Promotion: 23 September 2010

To my husband, Alin

Learn from yesterday, live for today, hope for tomorrow.

The important thing is not to stop questioning.

Albert Einstein

Table of contents

Abstract.....	5
Abbreviations	8
1. Introduction and general objectives.....	11
1.1. TAT peptide.....	14
1.1.1. Active mechanism of TAT peptide.....	16
1.1.2. Internalization of cargoes conjugated to TAT peptide	16
1.1.3. Independence of receptor mediated uptake.....	17
1.1.4. Non-endocytotic uptake of TAT peptide	17
1.2. Antimicrobial peptides.....	19
1.2.1. The antibacterial peptide NK-2	20
1.3. Biological and model lipid membranes.....	22
1.3.1. Evolving membrane models.....	22
1.3.2. Bacterial membranes	27
1.3.3. Membrane dynamics and physical properties.....	28
1.3.4. Membrane proteins	29
1.3.5. Model membranes	30
1.3.5.1.Giant unilamellar vesicles (GUVs)	31
1.4. Motivation of the study.....	33
2. Materials and Methods.....	35
2.1. Peptides.....	35
2.2. Lipids.....	35
2.3. Fluorescent tracers.....	36
2.4. Chemicals.....	36
2.5. Electroformation of giant unilamellar vesicles.....	37
2.6. Confocal fluorescence microscopy.....	39
2.7. Single molecule microscopy	41
2.7.1. Trajectory analysis.....	45

Table of contents

2.7.2. Jump distance analysis.....	47
2.8. Sample preparation for light microscopy.....	48
2.9. Monte Carlo simulations.....	48
 3. Results and discussion.....	52
3.1. TAT peptide interaction with neutral and anionic membranes.....	52
3.1.1. Imaging and tracking of single lipid analogs within anionic and neutral GUVs	52
3.1.2. Confocal imaging of TAT peptide-GUV interaction.....	58
3.1.3. Lateral mobility of single TAT peptides on the GUV surface at low concentration.....	60
3.1.4. Lateral mobility of single TAT on the GUV surface at high concentration.....	65
3.1.5. Monte Carlo simulations.....	65
3.1.6. Discussion.....	66
3.2. Interaction of TAT peptides with high content of anionic lipid PS.....	68
3.2.1. Neutral membranes with 20 mol % cholesterol.....	68
3.2.1.1. CLSM imaging of TAT peptide-membrane interaction using neutral GUVs	69
3.2.1.2. Lateral mobility of single TAT on neutral GUV surfaces.....	70
3.2.2. Interaction of TAT peptides with anionic model membranes.....	71
3.2.2.1. Imaging and tracking of single lipid analogs within anionic GUVs ...	71
3.2.2.2. CLSM imaging of TAT peptide-membrane interaction using anionic GUVs	72
3.2.3. Monte Carlo simulations.....	77
3.2.4. Discussion.....	79
3.3. Interaction of TAT peptides with model membranes containing lipids inducing a negative curvature (PE).....	81

Table of contents

3.3.1. Diffusion of single lipid analogs in model membranes containing PE.....	82
3.3.2. CLSM imaging of TAT peptide-GUVs interaction.....	83
3.3.3. Lateral mobility of single TATs on the GUVs surface.....	86
3.3.4. Discussion.....	89
3.4. Interaction of TAT peptides with model membranes at physiological salt concentration.....	91
3.4.1. Diffusion of single lipid analogs in model membranes in presence of 100 mM NaCl.....	91
3.4.2. CLSM imaging of TAT peptide- GUVs interaction in NaCl solution.....	93
3.4.2.1.Influx of tracers in presence of TAT peptide.....	94
3.4.2.2.Efflux of tracers in presence of TAT peptide.....	97
3.4.2.3.Influence of cholesterol on TAT peptide translocation.....	99
3.4.2.4.Influence of other ion types on TAT peptide translocation.....	101
3.4.3. Lateral mobility of TAT peptide on GUVs in NaCl solution.....	102
3.4.3.1. Diffusion of single lipid analogs in GUVs in presence of 2 μ M B-TAT.....	103
3.4.3.2. Tracking of single lipid analogs in GUVs in presence of 2 μ M B-TAT and 100 mM NaCl.....	104
3.4.4. Monte Carlo simulations.....	106
3.4.5. Discussion.....	107
4. NKCS- A study extended to antimicrobial peptides.....	112
 4.1. Results and discussion.....	112
4.1.1. Diffusion of single lipids analogs in model membranes.....	112
4.1.2. CLSM imaging of NKCS peptide-GUVs interaction.....	113
4.1.3. Lateral mobility of single NKCS on the GUVs surface.....	116
4.1.4. Discussions.....	112
5. Summary and Outlook.....	121

Table of contents

6. Acknowledgments.....	123
7. References	124
Curriculum vitae and list of publications.....	135
List of figures.....	136
List of tables.....	139

Abstract

Cell penetrating peptides (CPPs) like HIV1-TAT have the special property to traverse the cell membrane and to function as vectors for various macromolecular cargoes such as fluorophores, nucleotides, drugs, proteins, DNA, and peptide-nucleic acids, and even liposomes and magnetic nanoparticles. In spite of the fact that TAT peptides were intensively investigated, the exact internalization mechanism is still controversial. Descriptions of the internalization process range from energy-independent cell penetration of membranes to endocytic uptake: clathrin-independent endocytosis, caveolae-mediated endocytosis or macropinocytosis. The uptake mechanisms identified for TAT alone are valid also for cargoes that are introduced into the cells through coupling to the peptide. Experiments with genetically modified systems to suppress the endocytic internalization demonstrated that the transduction of TAT into living cells is not dependent on any endocytic or pinocytic events. Also, TAT was not excluded from cells that were transferred to 4 °C, a state where all potential endocytic pathways are inhibited. Recently, a pore formation, similar to the antibiotic peptides, was suggested by molecular dynamics simulations and black lipid experiments for TAT peptides.

Altogether, a consensus regarding the uptake mode has not been reached. Despite the controversy and uncertainty regarding the uptake mechanism, the property of TAT to deliver non-permeable molecules into living cells makes it an attractive tool for biological sciences as well as medicine and biotechnology. It is therefore essential to identify precisely the criteria which can yield an efficient cell penetration with a high degree of drug transfer. To elucidate the non-endocytic entry routes and the transduction mechanism, one possibility is to analyse interaction of TAT peptides with model membrane systems. In this study we use giant unilamellar vesicles (GUVs) as cytomimetic model system since the micrometer scale of the GUVs enables microscopic observation of these liposomes.

A parameter, which directly would reflect possible aggregate formation preceding internalization, is the mobility of CPPs on the membrane surface. Aggregation, pore nucleation and micelle formation should be reflected in gross changes of the diffusion properties of the peptide within the membranes. These can most conveniently be studied by single molecule observation using fluorescence microscopy employing electron

Abstract

multiplying CCD camera systems. Single fluorescently labelled molecules can be imaged microscopically as diffraction-limited spots. The intensity distribution of these spots may be approximated by a 2D Gaussian function. Thus, the position of the molecule at the very centre of the Gaussian can be determined with high precision by a fitting process. The localization precision may reach a few nanometers under optimal conditions. Thereby, fluorescence microscopy allows following the traces of single molecules in time with a very high spatial precision. The technique has mostly been applied to analyse the movement of single receptors and lipid molecules in biological membranes, but was recently extended to study single-molecule mobility within solution and the interior of mammalian cells. In this study we applied high-speed single-particle tracking (SPT) and confocal laser scanning microscopy to systematically examine factors that affect membrane binding, mobility and penetration of fluorescence labelled TAT peptides in the GUVs with different composition.

To focus onto interaction between TAT and lipids the first experiments were performed in sucrose/glucose solution with all ions excluded from the media. As a reference we first examined the mobility of fluorescent lipids within the GUV bilayer. As expected, lipid mobility varied clearly with the phase state of the membranes, whereas peptide mobility was independent on membrane hydrophobic core, but dependent on headgroup of lipids in the bilayer.

CLSM experiments revealed that in GUVs formed by phosphatidylcholine (PC) and cholesterol no translocation of TAT peptides but just accumulation on the membrane. The same effect was observed also for anionic GUVs containing 15-30 mol % phosphatidylserine (PS). Additional SPT experiments and evaluation of diffusion coefficients revealed that TAT peptides “float” on neutral membranes and they are partially inserted in the headgroup of anionic bilayers. The “floating” of peptides on neutral membranes and the slight immersion in the anionic bilayers were confirmed by Monte Carlo simulations. Introduction of a significant amount of anionic lipids (40 mol %) or lipids inducing locally a negative curvature into the membranes (20 mol %) affected TAT translocation across these membranes. Notably, we discovered that TAT peptides were not only able to directly penetrate such membranes in a passive manner, but they were also capable of forming physical pores, which could be passed by small but not large dye tracer molecules.

Abstract

For the physiological relevance of the study, additional experiments in the presence of salt solutions were performed. CLSM experiments showed that physiological salt solution dramatically changed the TAT interaction with the GUV membrane. Binding of TAT to GUVs of all employed compositions was completely lost, and the peptides now efficiently translocated into the GUV interior. In confocal images no membrane staining was observable and dye release indicated again pore formation. Also the sensitive single molecule microscope did not detect any trace of peptides on the GUV surface. This result was obtained for neutral or anionic, liquid-ordered or liquid-disordered membranes. Also, there was no difference for GUVs without cholesterol or in case of other salt solutions at the same concentration, 100 mM (CaCl₂, CaCO₃ or PBS).

The last chapter of this thesis comprises a study on the antimicrobial peptide NKCS, which supposedly acts by membrane pore formation. The experiments revealed similitudes in the action of antimicrobial NKCS with the cell penetrating TAT, but also certain differences. We observed that TAT peptides behave similar to NKCS, inducing pores in PE and anionic membranes (PS for TAT and PG for NKCS). A clear difference for these peptides was observed for GUVs prepared from phosphatidylcholine. CLSM experiments showed accumulation of TAT, but no interaction of NKCS with PC membranes. While for the CPP-TAT the ions from medium seemed to play a very important role for peptide translocation, NKCS activity was not affected by 100 mM salt solution.

Abbreviations

AFM	Atomic Force Microscopy
AF-TAT	Alexa Fluor 647-RRRQRRKKRG
AF488	Alexa Fluor 488
AOTF	Acousto-Optic Tuneable Filters
Bodipy-PC	2-(4,4-difluoro-5,7-dimethyl-4-bora-3a, 4a-diaza-s-indacene-3-pentanoyl)-1-hehadecanoyl- <i>sn</i> -glicero-3-phosphocholine
B-TAT	Biotin-Ahx-YGRKKRRQRRR (biotinylated TAT)
CaCl ₂	calcium chloride
CaCO ₃	calcium carbonate
CCD	Charge Coupled Device
CD	Circular Dichroism
chol	cholesterol
CLSM	Confocal Laser Scanning Microscope
CF	carboxyfluorescein
CPPs	Cell-Penetrating Peptides
CPZ	chlorpromazine
DIC	Differential Interference Contrast
DiI-C ₁₈	1,1'-dioctadecyl-3,3,3',3'-tetramethylindocarbocyanine
DOPC	1,2-dioleyl- <i>sn</i> -glycero-3-phosphocholine
DOPE	1,2-dioleyl- <i>sn</i> -glycero-3-phosphoethanolamine
DOPS	1,2-dioleoyl- <i>sn</i> -glycero-3-phospho-L-serine
DPPC	1,2-dipalmitoyl- <i>sn</i> -glycero-3-phosphatidylcholine
DPPE	1,2-dipalmitoyl- <i>sn</i> -glycero-3-phosphoethanolamine
DPPS	1,2-dipalmitoyl- <i>sn</i> -glycero-3-phospho-L-serine
DSC	Differential Scanning Calorimetry
Dy-NKCS	KILRGVSKKIMRTFLRRISKDILTGKK-C(Dy647-ME)-NH ₂
Dy-NKCS[15-27]	LRRISKDILTGKK-C(Dy647-ME)-NH ₂
Dy-NKCS[15-27S]	LRGISKKIDRTLK-C(Dy647-ME)-NH ₂
EIPA	5-(N-ethyl-N-isopropyl)amiloride

Abbreviations

EGFP	Enhanced Green Fluorescent Protein
EPR	Electron Paramagnetic Resonance
FCS	Fluorescence Correlation Spectroscopy
FITC	fluorescein isothiocyanate
FRAP	Fluorescence Recovery After Photobleaching
FRET	Fluorescence Resonance Energy Transfer
FTIR	Fourier transformed infrared spectroscopy
FWHM	Full Width at Half Maximum
GPI	glycosylphosphatidylinositol
GSLs	glycosphingolipids
GUVs	Giant Unilamellar Vesicles
ITO	Indium-Tin-Oxide
LUVs	Large Unilamellar Vesicles
LPS	lipopolysaccharides
LY	Lucifer Yellow
M β CD	methyl- β -cyclodextrin
MgCl ₂	magnesium chloride
MLVs	multilamellar vesicles
MSD	Mean Square Displacement
NA	Numerical Aperture
NaCl	sodium chloride
NMR	Nuclear Magnetic Resonance
PA	phosphatidic acid
PI	phosphatidylinositol
PMT	photomultiplier tube
POPE	1-palmitoyl-2-oleoyl- <i>sn</i> -glycero-3-phosphoethanolamine
POPG	1-palmitoyl-2-oleoyl - <i>sn</i> -glycero-3-[phospho- <i>rac</i> -(1-glycerol)]
PS	phosphatidyl serine
PTDs	Protein Transduction Domains
PBS	phosphate buffered saline
R-TAT	TAMRA-RRRQRRKKRG (rhodamine-labelled TAT)

Abbreviations

SANS	Small Angle Neutron Scattering
SAXS	Small Angle X-ray Scattering
SM	sphingomyelin
SMF	single molecule fluorescence microscopy
SNR	signal-to-noise ratio
SPT	Single Particle Tracking
SUVs	Small Unilamellar Vesicles
TAMRA	tetramethyl-6-carboxyrhodamine
TR-DHPE	Texas Red-1,2-dihexadecanoyl- <i>sn</i> -glycero-3-phosphoethanolamine
TRITC	tetramethyl rhodamine iso-thiocyanate
ULVs	unilamellar vesicles
UV-VIS	ultraviolet-visible

1. Introduction and general objectives

In the past decade, specific peptides and proteins have been shown to penetrate cell membranes by a process called transduction [1], [2]. The peptide sequences, which could be identified as responsible for the translocation capability, were designated as protein transduction domains (PTDs) [3], cell-penetrating peptides (CPPs) [4] or Trojan horse peptides [5].

CPPs have been demonstrated to enter a large number of cell types [3] and to function as vectors for various macromolecular cargoes such as fluorophores, nucleotides, drugs, proteins, DNA, and peptide-nucleic acids and even liposomes and magnetic nanoparticles [6].

Descriptions of the internalization process range from energy-independent cell penetration of membranes to endocytic uptake: clathrin-independent endocytosis [7]; [8], caveolae-mediated endocytosis [9]; [2] or macropinocytosis [10]; [11]; [12]. Figure 1.1 shows the main endocytic pathways of CPPs internalization.

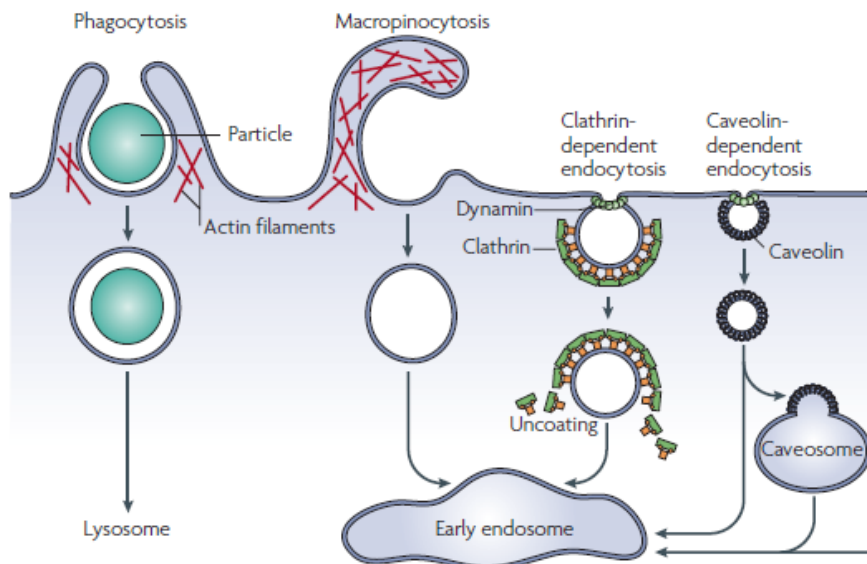


Figure 1.1: Pathways of active entry into cells (adapted from [13]). Details are given in the text.

1. Introduction and general objectives

Active uptake of fluids and small particles occurs by **macropinocytosis**. This process consists in formation of large endocytic vesicles (macropinosomes) generated by actin-driven circular ruffles of the plasma membrane. Most internalized cargoes are delivered to the early endosome via vesicular (clathrin- or caveolin-coated vesicles) or tubular intermediates (known as clathrin- and dynamin dependent carriers) that are derived from the plasma membrane. **Clathrin** is a cytosolic protein which has the property to form domains of the plasma membrane termed clathrin-coated pits. Dynamin is a GTPase involved in the scission of newly formed vesicles from the membrane (Figure 1.1). **Caveolae** are the most common reported non-clathrin coated plasma membrane vesicles and they consist of the cholesterol-binding protein caveolin with a bilayer enriched in cholesterol and glycolipids.

Obviously, the internalization process varies for different CPPs. In general, however, the biophysical mechanism of the plasma membrane translocation of the CPPs is not well understood in its entire complexity. A highly charged cationic domain is common for most CPPs and essential for translocation. However, it is known that charged molecules usually do not cross the lipid bilayer by passive diffusion due to the high Born charging energy encountered in a medium with a low dielectric constant. Cells usually utilize special transport systems such as ion carriers, channels, and ATP-coupled pumps to regulate the flow of ions and charged molecules across their membranes. From a physico-chemical point of view, it is therefore very surprising that short peptides containing a high percentage of cationic amino acids can nevertheless cross the plasma membrane of living cells by pathways, which mostly appear to function without energy consumption. Complex formation of the cationic peptide with anionic cell surface components such as **anionic lipid** head groups or the **proteoglycan heparan sulphate**, which is present on the surface of most cell plasma membranes, could result in an electrically neutral complex, which might subsequently be taken up by adsorptive **endocytosis** [14], [15].

Three mechanisms were suggested for charged peptides to cross the hydrophobic barrier of a biological membrane without utilizing an active transport system [16]. One possibility is **direct membrane penetration**. An alternative hypothesis invokes the binding of CPPs to negatively charged lipids and disruption of the bilayer structure by formation of **inverted micelles** resulting in their traversing into the cytoplasm [17]. Translocation may either involve entrapment of the peptide within the micelle and release on the other side of

1. Introduction and general objectives

the plasma membrane, or formation of micelles locally perturbs the bilayer and thereby induces the insertion of the peptide into the bilayer and the membrane transfer (Figure 1.2).

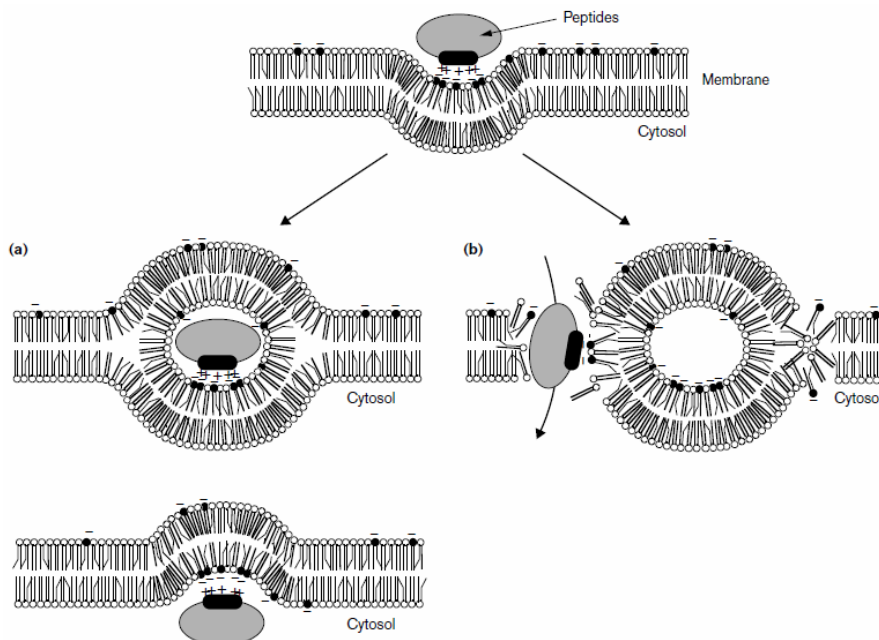


Figure 1.2: Translocation mediated by the formation of inverted micelles. In the model (a), the peptides are entrapped in micelles, which can release them inside the cell. In the model (b), the micelles perturb the structure of the bilayer, allowing peptide translocation. (Figure taken from [17]).

Thirdly, a translocation similar to the action of antibiotic peptides has been suggested for CPPs [18]; [19]; [20]. The classical models that describe the transport of antimicrobial peptides across biomembranes are the **toroidal pore**, **barrel-stave model** and the **carpet model** [21], [6], [22] (Figure 1.3). Almost all antimicrobial peptides are organized into an amphipathic structure composed of hydrophilic and hydrophobic aminoacids [23]. The peptides reach the membrane either as monomers or oligomers and then bind to the surface of the membrane with their hydrophobic surfaces facing the membrane and their hydrophilic surfaces facing the solvent. In the **pores** model a limited number of peptides first assemble on the lipid bilayer and then inserts into the bilayer with the hydrophilic regions of the peptides associating with the phospholipid head groups while the hydrophobic regions associate with the lipid core, and when a threshold concentration of peptide is reached, transient pores can be formed (Figure 1.3(a)).

1. Introduction and general objectives

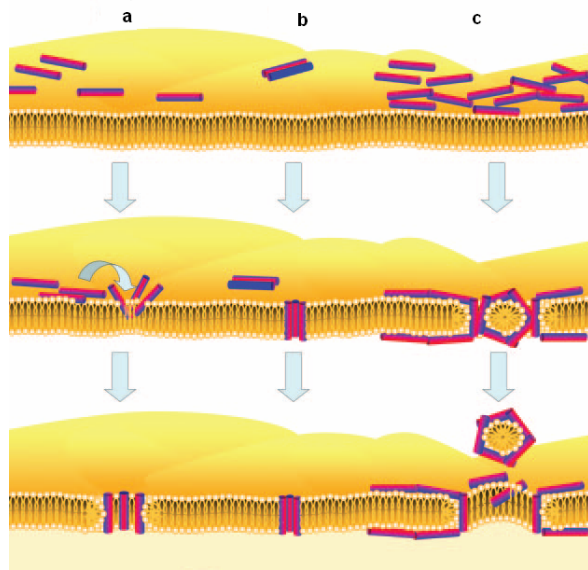


Figure 1.3: Models proposed for the membrane permeation of membrane-active antimicrobial peptides: (a) toroidal pore model, (b) barrel-stave model, and (c) carpet model. Color designation: blue, hydrophobic surface; red, hydrophilic surface. Figure modified from [22]

In the **barrel-stave** model (Figure 1.3(b)), the peptides insert in a perpendicular orientation to the plane of the bilayer, forming the “staves” in a “barrel”-shaped cluster, with the hydrophilic regions of the peptides facing the lumen of the pore and the hydrophobic regions interacting with the lipid bilayer. In the **carpet** model, peptides accumulate on the membrane surface until the membrane is disintegrated (Figure 1.3 (c)). The real mechanisms behind passive translocation of the CPPs are still mostly unknown, although it is clear that the attractive peptide–membrane interactions are important for the internalization process.

1.1. TAT peptide

In 1988, during the research in the field of AIDS, the remarkable ability to traverse a cell plasma membrane of a protein involved in the replication of HIV-1 was revealed [24], [25]. Later it was shown that the minimal length required for the biological cell-penetration of this molecule was much shorter. The TAT regulatory protein is an 86-

1. Introduction and general objectives

amino-acid-long nuclear protein, of which the 48–57 aminoacid residues (Gly-Arg-Lys-Lys-Arg-Arg-Gln-Arg-Arg-Arg), designated as HIV1 TAT peptide (Figure 1.4), are responsible for translocating across the cell plasma membrane [26], [27], [28]. Thus TAT became known as the first cell-penetrating peptide.

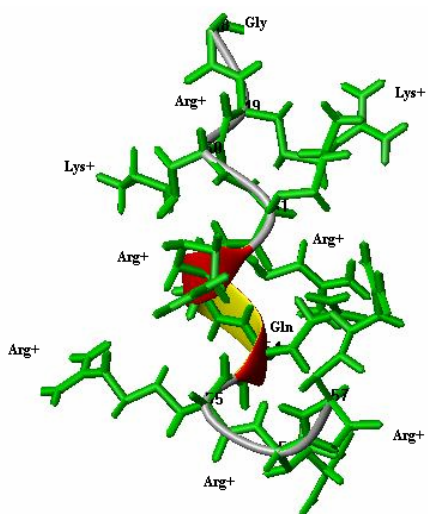


Figure 1.4: Secondary structure of TAT peptide. Illustration was prepared with the software MolMol (<http://ftp.mol.biol.ethz.ch/software/MOLMOL/>)

The HIV1 TAT peptide can provide a powerful tool for biologically active molecule delivery [29]. Its cell membrane penetration capacity was applied to transport fluorophores, nucleotides, proteins [30], drugs, supermagnetic nanoparticles [31], imaging and radiotherapeutic agents [32] and genes into cells [33], [16]. Proteins with a mass exceeding 100 kDa, 40 nm magnetic nanoparticles, quantum dots [34], [35] and even 200 nm liposomes [36], [37], [38] have been delivered to the cellular interior using TAT peptides [39]; [40]. The TAT-CPP contains 10 amino acids comprising six arginine and two lysine residues making the peptide highly cationic. It has been shown that the amount and rate of cellular uptake strongly depends on the component number of basic residues, specifically the number of arginines [41]; [42]. Also, substitution of a non-charged glutamine residue with alanine has no effect on cellular uptake, but substitution of any of the basic residues (arginine or lysine) significantly decreases cellular uptake.

1.1.1. Active mechanism of TAT peptide

In spite of the fact that up to now the TAT peptide was under intense investigation, the exact internalization mode, intracellular routing and destination are still controversial. It is now accepted that the entry to cells by an endocytotic mechanism is achieved by macropinocytosis, caveolae-mediated and clathrin dependent endocytosis.

An evidence for a macropinocytotic mechanism of TAT uptake in live mouse cells was published in 2004 and shown by co-localization of an endosome marker with TAT [43]. Latter, experiments with methyl- β cyclodextrin, which is used as an inhibitor of lipid raft formation, suggested that internalization of fluorescently labelled TAT peptide is mediated by lipid raft dependent macropinocytosis in Namalwa cells [10]. They showed that TAT-fusion proteins (30 kDa) entered cells by macropinocytosis, too. In addition, early studies using a caveolae-mediated endocytosis inhibitor failed to inhibit TAT internalization [44]. Caveolin-dependent endocytosis in HeLa and HL3T1 cells was shown for TAT-avidin and fusion protein of TAT with enhanced green fluorescent protein (EGFP) [8]. In HeLa, HepG2 and CHO cells, the internalization of fluorescently labelled TAT peptide was suggested to result from clathrin dependent endocytosis [45], [46].

In 2007 was observed that TAT and other arginine-rich CPPs were internalized by means of all three endocytotic pathways, depending on peptide concentration [12]. Chlorpromazine (CPZ) was used for the inhibition of clathrin mediated internalization, 5-(N-ethyl-N-isopropyl) amiloride (EIPA) for inhibition of macropinocytosis and methyl- β -cyclodextrin (M β CD) for disruption of import through caveolae/lipid rafts. At low concentrations below 10 μ M TAT entered through caveolae/lipid-raft-mediated endocytosis and macropinocytosis. Interestingly, at higher peptide concentrations, clathrin mediated internalization was more probable.

1.1.2. Internalization of cargoes conjugated to TAT peptide

The uptake mechanisms identified for TAT alone retain their validity also for cargoes that are introduced into the cells through coupling to the peptide. Tünnemann et al. [29] showed that TAT carries cargoes across cell membranes with high efficiency by at least

1. Introduction and general objectives

two functionally distinct mechanisms according to whether the cargo is big or small. Big cargoes, such as proteins or quantum dots, enter via caveolae endocytosis and macropinocytosis. Small cargoes, such as peptides of less than 30–40 amino acids, enter both slowly by endocytosis and rapidly by an unknown mechanism, called transduction, that utilises the membrane potential [29], [17], [47].

1.1.3. Independence of receptor mediated uptake

Although there were some early reports indicating the existence of specific cell surface receptors for the TAT protein [48], experiments with L- and D-enantiomeric peptides [42], [49] do not support the idea of CPPs binding to specific receptors. Instead, in some cases, the initial association with the plasma membrane was attributed to multivalent interactions with cell surface heparan sulphate proteoglycans. Contrary to the uptake through endocytosis, for a fluorescein-labelled TAT peptide, Ziegler et al. [50] observed a rapid cellular import into fibroblasts that was heparan sulphate dependent. Other studies [12] showed that at low peptide concentrations (1 μ M) removal of cell surface heparin sulphates had no effect on TAT peptide uptake but for 100 μ M, a requirement for cell surface heparan sulphate for peptide internalization was necessary.

1.1.4. Non –endocytotic uptake of TAT peptide

Recently, systems genetically modified to inhibit the endocytotic uptake were used to clarify the role of endocytosis in the translocation of TAT peptide [51]. The potential side effects and lack of specificity of inhibitors for endocytosis made the previous studies difficult to interpret. For example, methyl- β -cyclodextrin affects both lipid raft [10] and caveolin-coated vesicle formation. Hence it is difficult to distinguish between macropinocytosis and caveolin-dependent endocytosis. Also, the inhibitors could have other side effects that may influence the import of TAT, *e.g.* chlorpromazine was shown to interface with a number of Ca^{2+} -dependent signalling pathways [52]. Thus, genetically modified systems or physical methods seem to be more promising to clarify the

1. Introduction and general objectives

translocation mechanism of TAT because they avoid possible side effects of chemical inhibitors for endocytosis. The results with such systems demonstrated that the transduction of TAT into living cells is not dependent on any endocytic or pinocytic events and most importantly, TAT was not excluded from cells that were transferred to 4 °C, a state where all potential endocytic pathways are inhibited [51].

To elucidate the non-endocytic entry routes and the transduction mechanism, one possibility is the study of TAT peptide interaction with model membrane systems. In all models the first step for the translocation is the association of the peptide with components of the outer membrane leaflet. It is generally agreed that electrostatic forces between the positively charged peptide TAT and negative charges of phospholipids play a major role in the membrane binding of the peptide [53]. In addition, non-electrostatic forces, such as hydrogen bonding and hydrophobic or van der Waals forces, support the contact of TAT with the membrane by contributing about ~20% to the binding energy [54]. Recent results showed that the efficient binding of TAT requires a fluid membrane with lipids in the liquid-disordered state for the peptide-induced selective segregation of the negatively charged lipids, which is necessary to neutralize the positive charges on the peptide [53], [55]. Also, the interaction between TAT peptide and the membrane remains unaffected by changing the chemical nature of the negative charge, such as replacing PG with PS, but it is attenuated in the presence of a high salt concentration [54].

There are experimental reports that indicate that TAT peptides labelled by fluorophores can directly traverse the lipid bilayers of giant unilamellar vesicles (GUVs) but not large unilamellar vesicles (LUVs) of the same composition [56]. Besides the size, the composition of the membrane seems to play an important role in TAT peptide translocation. Mishra and al. [19] showed internalization of the peptide in GUVs (diameters of 5–30 μm) with high content of DOPE (40%). They observed also from SAXS experiments that the cationic CPP interacts strongly with localized negative charges in both anionic and neutral zwitterionic lipids (DOPS and DOPC) but does not interact directly with DOPE. Besides that, SAXS pointed to a pore formation mechanism similar to the antibiotic peptides. On the other hand, the pore mechanism was also suggested by molecular dynamics simulation [18] and black lipids experiments [20]. But the results of [51] argue against the formation of nonselective pores in membranes of genetically modified cells to suppress endocytosis. The authors observed that the fluorophore FITC

1. Introduction and general objectives

applied to the cells together with the TAT peptide, remained outside of the cells, whereas TAT transduced selectively into the cells.

In any case, a consensus regarding the uptake mode has not been reached. Despite the controversy and uncertainty regarding the uptake mechanism, the property of TAT to deliver nonpermeable molecules into living cells makes it an attractive tool for biological sciences as well as medicine and biotechnology. It is therefore essential to identify precisely the criteria which can define an efficient cell penetration with a high degree of cargo transfer.

1.2. Antimicrobial peptides

Bacterial resistance to conventional antibiotics has become a major problem worldwide due to their extensive use. There are already strains of bacteria resistant to all available drugs [57]. The development of new families of antibiotics that can overcome the resistance problem has become a very important task.

Antimicrobial peptides are an abundant and diverse group of molecules (see <http://www.bbcm.univ.trieste.it/~tossi/pag1.htm> for database) that are produced by many tissues and cell types in a variety of invertebrate, plant and animal species to defend themselves against invading pathogenic microorganisms [23], [22]. The peptides differ in size, sequence, charge, hydrophobicity and their ability to interact with membranes. But they all are amphipathic, charged molecules which can kill bacteria and fungi. The following four features are required of antimicrobial peptides [58]:

- (1) Selective toxicity; the peptides should discriminate between host and microbial cells.
- (2) Fast killing; the time needed for bacterial killing should be much shorter than the doubling time of the target bacteria, which is 20 min in the case of *Escherichia coli*.
- (3) Broad antimicrobial spectra; desirably a single peptide species should be effective against many species of microorganisms.
- (4) No resistance development; the peptide should have such a mechanism of action that the bacteria cannot easily develop resistance against it.

1. Introduction and general objectives

The killing mechanism of antimicrobial peptides is different from that of conventional antibiotics, so antimicrobial peptides are considered as attractive substitute for additional drugs. However, most antimicrobial peptides are toxic not only to a variety of microorganisms, but also to healthy cells [59].

Their aminoacid composition, amphipathicity, cationic charge and size influence the attachment of the antimicrobial peptides and insertion into membrane bilayers. Subsequently these peptides contact the anionic surface of the cytoplasmic membrane and insert initially in the interface of the hydrophilic head groups of membrane phospholipids. After insertion into the membrane, antimicrobial peptides act by either disrupting the physical integrity of the bilayer, or via membrane thinning, to form pores by “carpet”, “barrel-stave” or “toroidal-pore” mechanisms.

1.2.1. The antibacterial peptide NK-2

The peptide NK-2 is derived from the natural occurring 78 amino acid residue protein NK-lysin, isolated from porcine small intestine [60]. Investigations on a broader selection of bacteria, fungi and mammalian cells showed a high selectivity against pathogens and NK-2 was suggested to be a potent member of peptide antibiotics [60]. Also, it is not toxic for human cells. The NK-2 peptide is mainly unstructured in phosphate buffer but adopts an amphipathic, α -helical secondary structure in membranes and it interacts specifically with negatively charged lipids. The α -helical structure of NK-2 was confirmed by circular dichroism (CD) and Fourier transformed infrared spectroscopy (FTIR) measurements [61].

All antimicrobial peptides investigated in this study are derived from NK-2 (Table 1.1). The first modification of NK-2 is the substitution of the aminoacid cysteine by a serine (NK-CS) to inhibit the dimerisation of NK-2 by disulfide bridges. This substitution is expected to improve the stability by reducing the peptide sensitivity to oxidation. The replacement also leads to a significant increase of the antibacterial activity of the peptide NKCS against both Gram negative and Gram positive bacteria [62]. Figure 1.5 shows the secondary structure of NKCS.

1. Introduction and general objectives

Table 1.1: Comparison of the amino acid sequences of the antibiotic peptides NK-2 and 3 derivatives used in this study. The modified amino acids are highlighted in red.

39 40 41 42 43 44 45 46 47 48 49 50 51 52 53 54 55 56 57 58 59 60 61 62 63 64 65 K I L R G V C K K I M R T F L R R I S K D I L T G K K	NK-2
K I L R G V S K K I M R T F L R R I S K D I L T G K K	NK-CS
L R R I S K D I L T G K K	NKCS-[15-27]
L R G I S K K I D R T L K	NKCS-[15-27S]

To study the partial activity of the NK-CS peptide and to determine the function and the importance of different sections of the peptide, short derivatives were analysed: NKCS-[15-27] and NKCS-[15-27S]. Figure 1.6 shows the structure of NKCS-[15-27], which is similar to NKCS-[15-27S]. The properties of NKCS and its derivatives are summarized in Table 1.2.

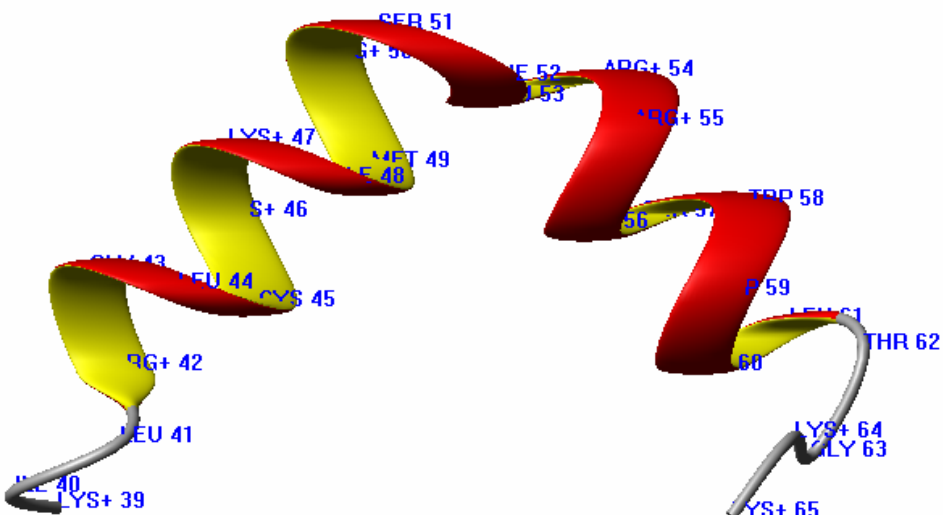


Figure 1.5: The secondary structure of NKCS with two α -helices (prepared with the software MolMol). The hydrophobic face is shown in yellow.

1. Introduction and general objectives

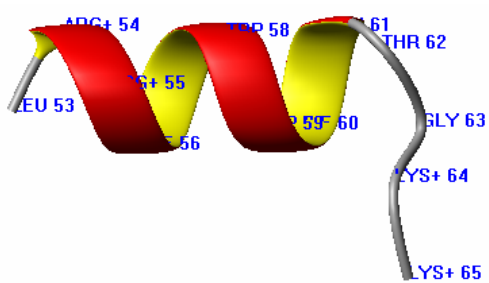


Figure 1.6: The secondary structure of NKCS-[15-27] (prepared with the software MolMol). The hydrophobic face is shown in yellow.

Table 1.2: Properties of the peptides as determined by the calculator based on Hoop-Woods scale from <http://www.innovagen.se/custom-peptide-synthesis/peptide-property-calculator.asp>

Peptide	Mass (Da)	Net charge	Hydrophobicity	Iso-electric point, pI
NKCS	3186	+10	6.76	12.4
NKCS-[15-27]	1527.9	+5	4.36	11.6
NKCS-[15-27S]	1527.9	+5	4.36	11.6

1.3. Biological and model lipid membranes

1.3.1. Evolving membrane models

The cell is the fundamental unit in biology. Each cell is spatially defined by its cytoplasmic membrane which acts as a protective wall to exclude most molecules that are not actively imported by living cells. This is an efficient way for a cell to prevent uncontrolled influx or efflux of solutes, which otherwise could be harmful to it. Lipids are a fundamental part of all cellular membranes, organized in bilayer form. Most membranes contain around 40% lipids, the internal mitochondrial membrane around 20% only, and the myelinic membranes even up to 70% lipids [63].

The bilayer nature of biomembranes was first suggested in 1925 by Gorter and Grendel [64] and an important step forward was the fluid mosaic model by Singer and Nicholson

1. Introduction and general objectives

in 1972 [65]. According to this model, the cell membrane was characterized as: “a two-dimensional oriented solution of integral proteins (or lipoproteins) in the viscous phospholipids bilayer solvent” [65].

The modern view for molecular architecture of cell membrane is a composite model. The first shell is a multi-component lipid-protein bilayer called plasma membrane, followed on the cytoplasmatic side, by a two-dimensional macromolecular network called membrane cytoskeleton (Figure 1.7). The extra-cellular side of plasma membrane is covered by a densely packed macromolecular film formed by the head groups of cell surface glycoproteins. The membrane-associated cytoskeleton is a rubber-like network composed of semi-flexible spectrin interconnected with actin filaments [66].

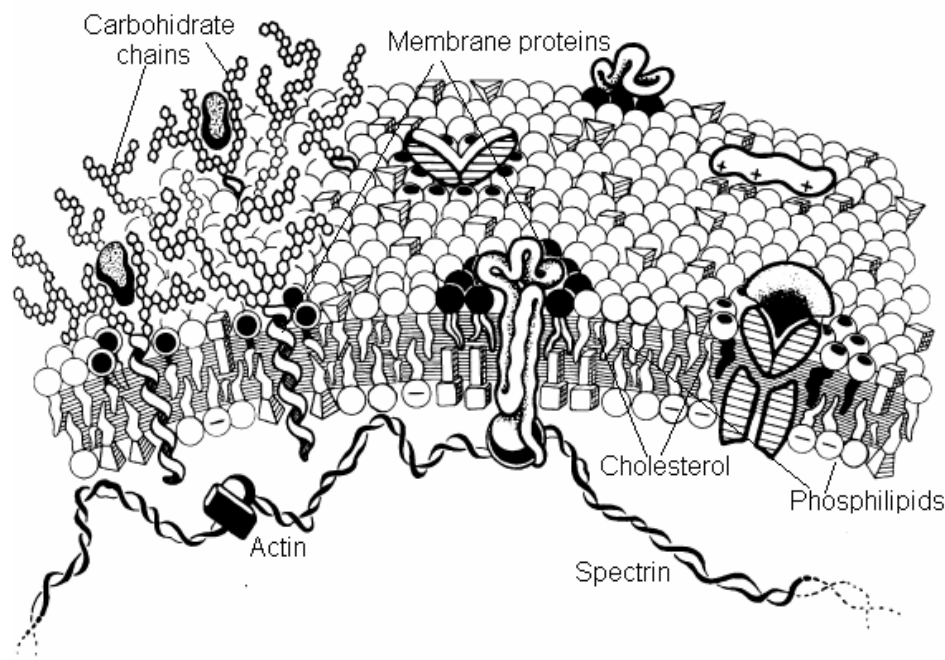


Figure 1.7: A schematic representation of plasma membrane (modified from [66])

The eukaryotic lipid membrane is unique in its great diversity of lipid species. The three main lipid constituents of the cellular membrane are **phospholipids**, **cholesterol**, and **glycolipids** (Table 1.3) [67]. The major structural lipids in eukaryotic membranes are the **phospholipids** (Figure 1.8): phosphatidylcholine (PC), phosphatidylethanolamine (PE), phosphatidylserine (PS), phosphatidylinositol (PI) and phosphatidic acid (PA). A typical

1. Introduction and general objectives

phospholipid consists of four components: fatty acid(s) which contains saturated or *cis*-unsaturated acyl chains of varying lengths, the platform to which the fatty acids are attached (glycerol), a phosphate, and an alcohol attached to the phosphate [63] which determines the name of the hydrophilic head group. In glycerophospholipids, the fatty acid in *sn*-1 position of the glycerol backbone is usually saturated and the fatty acid in *sn*-2 position unsaturated. Phosphatidylcholine accounts for >50% of the phospholipids in most eukaryotic membranes.

Table 1.3: Approximate lipid composition of different cell membranes, [67]

Lipid	Percentage of total lipid by weight					
	Liver cell plasma membrane	Erythrocyte plasma membrane	Myelin	Mitocondrion (inner and outer membrane)	Endoplasmatic reticulum	<i>E. coli</i>
Cholesterol	17	23	22	3	6	0
Phosphatidylethanolamine	7	18	15	35	17	70
Phosphatidylserine	4	7	9	2	5	(trace)
Phosphatidylcholine	24	17	10	39	40	0
Sphingomyelin	19	18	8	0	5	0
Glicolipids	7	3	28	(trace)	(trace)	0
Others	22	13	8	21	27	30

Glycolipids are derived from sphingosine. Instead of phosphoryl choline, glycolipids contain one or more sugars attached to the primary hydroxyl group of the sphingosine backbone. The major sphingolipids in mammalian cells are sphingomyelin (SM) and the glycosphingolipids (GSLs), which contain mono-, di- or oligosaccharides based on glucosylceramide and sometimes galactosylceramide.

The third major constituent of the eukaryotic biomembranes is **cholesterol**, accounting up to 30-50 mol % of the total lipids in plasma membrane. It has a tetracyclic ring structure with a double bond in one of the rings and one free hydroxyl group (Figure 1.8).

The distribution of lipids between intra- and extracellular leaflets of the plasma membrane is asymmetric and maintained by ATP-dependent systems [68]. For instance, PE and the negatively charged phospholipid PS are mainly located in the intracellular leaflet of the bilayer, making the membrane electrically polarized. In contrast, PC and SM reside predominantly in the outer leaflet [69]. Glycolipids are oriented with the sugar residues on

1. Introduction and general objectives

the extracellular side of the membrane [70]. The distribution of cholesterol may also be asymmetric between the cytoplasmic and ectoplasmic leaflets [71].

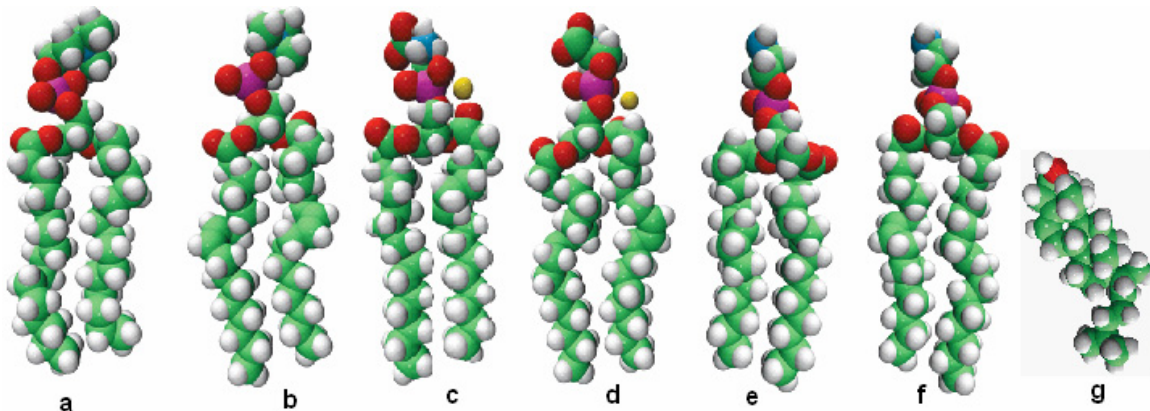


Figure 1.8: Examples of membrane lipids, (a) DPPC, (b) DOPC, (c) DPPS, (d) DOPS, (e) DPPE, (f) DOPE and (g) cholesterol (structural formulas from <http://avantilipids.com>)

Lipid packing into small scale 3D structures is governed by the effective shape of the lipid that is determined by van der Waals volume and geometry of the molecule as well as hydration shell, conformation, intermolecular forces acting on a molecule or electrostatic interactions. The final shape of a lipid aggregate is generally described by the so-called shape factor or packing parameter p defined as [72]

$$p = \frac{v}{al},$$

where v is the volume of hydrocarbon chain(s), a is area occupied by the headgroup, and l the maximum length of hydrocarbon chains.

The simplest lipid structures are spherical micelles, formed by molecules preferentially adopting conical shape, *i.e.* $p < 1/3$ (Figure 1.9). Non-spherical (*e.g.* rod-like or discoidal) micelles are possible when molecular geometry of molecules resembles to a truncated cone with $1/3 < p < 1/2$. The biologically most important mode of lipid packing requires nearly cylindrical molecular shape with $1/2 < p < 1$ for lipids. In this case a bilayer is formed. In a planar bilayer, the hydrophobic chains in the middle of the structure are very well accommodated as they are in a hydrophobic environment and the hydrophilic heads are exposed to water. But at the edge, the hydrocarbon chains are exposed to water and the structure will tend to shield them by connecting open edges with each other. This will

1. Introduction and general objectives

result in vesicles (Figure 1.10) and the lipid bilayer is thus held together efficiently by non-covalent interaction. When $p > 1$ inverted structures with a negative spontaneous curvature (*e.g.* inverted micelles or inverted hexagonal phase) are favoured (Figure 1.9).

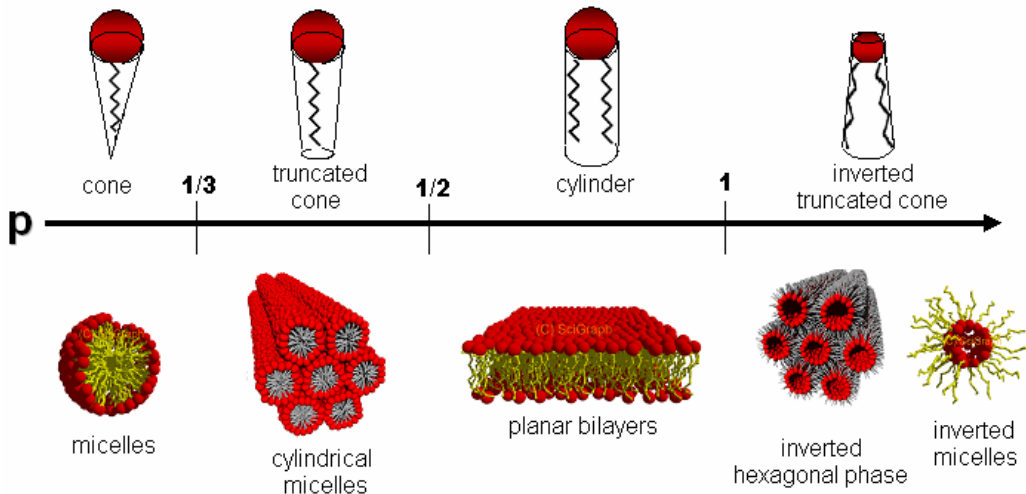


Figure 1.9: Schematic illustration of the impact of packing parameter p on lipid aggregate structures

Membrane curvature plays an important role in cellular function. The proper function of neurons, for example, requires both the highly curved synaptic vesicles of the axons and the more planar plasma membrane [63]. The bilayer-forming lipids have a spontaneous curvature close to zero (Figure 1.9), whereas the curvature of the non-bilayer forming ones may be either positive or negative [72]. A significant fraction of eukaryote cell lipids are non-bilayer forming [73]. These lipids may facilitate fusion and transport by increasing membrane flexibility. Membrane curvature also affects the penetration and activity of certain membrane-bound enzymes [74]; [75].

1. Introduction and general objectives

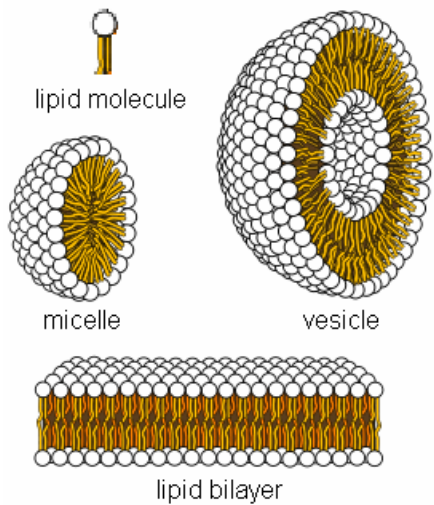


Figure 1.10: Lipid structures. Figure modified from <http://www.pharmainfo.net/reviews/overview-brain-targeting-drug-delivery-system>

Phosphatidylcholine (PC) and phosphatidylserine (PS) have a nearly cylindrical molecular geometry, with the lipidic tails facing each other and the polar headgroups interfacing with the aqueous phase. Phosphatidylethanolamine (PE) assumes a conical molecular geometry because of the relatively small size of its polar headgroup (Figures 1.8 and 1.9). The inclusion of phosphatidylethanolamine in phosphatidylcholine bilayers imposes a curvature stress onto the membrane, which is used for budding, fission and fusion [76]. **Sphingolipids** have saturated (or *trans*-unsaturated) tails so they are able to form taller, narrower cylinders than phosphatidylcholine lipids of the same chain length and they pack more tightly, adopting the solid “gel” phase; they are fluidized by sterols.

1.3.2. Bacterial membranes

The cell membranes of bacteria (Gram positive and Gram negative) differ in their composition significantly from mammalian cell membranes (see Table 1.3). Gram positive bacteria like *Bacillus subtilis* or *Staphylococcus carnosus* possess only one lipid bilayer connected to a peptidoglycan network, but Gram negative bacteria like *Escherichia coli* have a second lipid bilayer consisting of lipopolysaccharide reaching into the extracellular space [77]. The lipopolysaccharides (LPS) are relevant in bacterial infections. When LPS

1. Introduction and general objectives

is released from the membrane it can cause sepsis depending on the location and eliberalated amounts. In consequence a potent antimicrobial peptide should inhibit the release of LPS by Gram negative bacteria, either by killing the bacteria very fast before the LPS is secreted or by neutralizing the bacterial endotoxin after its release [78].

Bacterial plasma membranes mainly consist of phosphoethanolamine (PE) and a high amount of anionic lipids like phosphatidylglycerol (PG) (see Table 1.3 for *E. coli*).

1.3.3. Membrane dynamics and physical properties

According to the solid-liquid composite model [66] the lipid matrix of cell membranes is a fluid structure at physiological temperature. The membrane lateral pressure profile is an essential concept of lipid dynamics. This is in part determined by the repulsive interactions between the hydrated headgroups and in the acyl-chain region of the bilayer, leading to a tendency for lateral expansion. Conformational, translational, and vibrational membrane dynamics take place on various time- and length-scales. In addition, several factors affect lipid dynamics: temperature, hydration, pressure, as well as the structure and number of lipid species involved [79].

Techniques that offer insight into structure and diffusion processes in cellular membranes include fluorescence recovery after photobleaching (FRAP) [80], single particle tracking (SPT) [81], fluorescence correlation spectroscopy (FCS) [82], fluorescence resonance energy transfer (FRET) [83] and nuclear magnetic resonance (NMR), infrared and Raman spectroscopy, electron paramagnetic resonance (EPR) on spin labels, differential scanning calorimetry (DSC), X-ray and neutron diffraction and molecular simulations [84], [85].

Lipids can adopt a variety of phases and the phase transition (Figure 1.11) is mostly thermally induced. In the **gel phase (L_β)**, the hydrocarbon chains are ordered in all-trans configurations and there is a long-range translational order, impeding lateral movement. Increasing of the temperature above the melting point, T_m , result the **liquid-crystalline phase (L_a)**. This is characterized by low conformational order in the carbon chains (lower internal order) and by low translational order (lower packing order, higher translational diffusion). For this reason this state has also been termed **liquid-disordered phase (L_d)**.

1. Introduction and general objectives

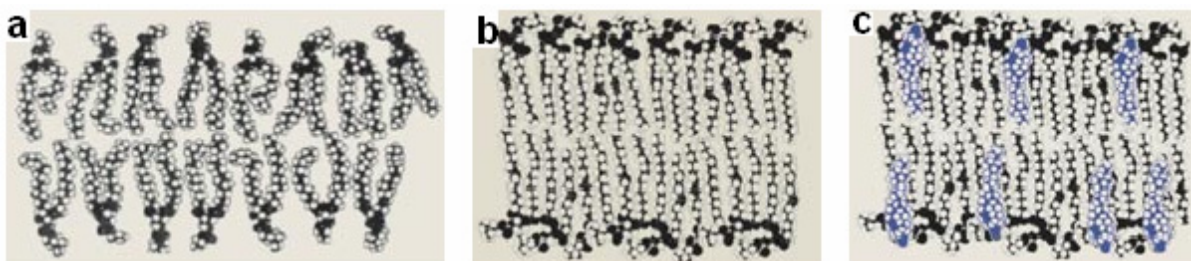


Figure 1.11: Lipid bilayer phases: (a) liquid-crystalline or liquid-disordered, (b) solid gel, (c) liquid-ordered. Representation modified from [63]

The steroid structure of cholesterol molecule is rather stiff and smooth favouring a gel-like ordered conformation of vicinal lipid acyl chains, but on the other hand its molecular shape is clearly different from other lipids thus disrupting the packing order of neighbouring phospholipids. As a consequence, to accommodate better into phospholipid bilayer cholesterol induces a so-called **liquid-ordered (Lo)** phase which is an intermediate between L β and L α phases (Figure 1.11) demonstrating rapid lateral diffusion of lipids similar to fluid bilayers and conformational order of acyl chains resembling that of gel phase membranes [86], [63]. Furthermore, incorporation of cholesterol into phospholipid membranes increases the thickness of bilayers, reduces its elasticity and the permeability to small water-soluble molecules [87]. Without cholesterol -such as in bacteria- a cell would need a cell wall. Cholesterol prevents crystallization of hydrocarbons and phase shifts in the membrane. The affinity of cholesterol for membrane lipids varies significantly with the polar headgroup and backbone structure of the lipid molecule, generally decreasing in the order SM>PS>PC>PE [88], [89].

1.3.4. Membrane proteins

Membrane proteins are long-chained polypeptide polymers consisting of amino acid residues [72]. Compared to membrane lipids, membrane proteins are structurally rigid. Membrane proteins can be divided into two classes: integral proteins and peripheral proteins. The integral proteins penetrate the bilayer and can be directly integrated into the membrane by exposure of hydrophobic aminoacid residues, either in a transmembrane

1. Introduction and general objectives

manner (single pass α -helix, multi pass α -helices, β -barrel) or by embedding of a α -helix only in the cytosolic leaflet, *i.e.* in plane with the membrane. Their functional domains may be located within the hydrophilic head group or within the hydrophobic core. Examples of the former class are cell adhesion molecules, and of the second ion pumps, hormone receptors, photosynthetic reaction centres or enzymes generating extracellular matrix proteins such as hyaluronic acid synthase [66].

Peripheral proteins are associated with membranes indirectly by lipidic anchors, *i.e.* fatty acids (myristic acid, palmitic acid), prenyl groups (farnesyl, geranylgeranyl) or a C-terminally linked glycolipid (glycosylphosphatidylinositol-(GPI)-anchor). Examples include many receptors, and proteins involved in membrane based signal transduction processes, such as phospholipases or GTPases [66]. A second major coupling mechanism is through electrostatic interaction. A peculiar mode of binding is through amphiphatic α -helices, which exhibit a hydrophobic and hydrophilic face in the axial direction. They can switch between a horizontal and a normal position by charging the hydrophilic ends. The transition between membrane and cytoplasmic proteins is not very distinct. Thus, proteins involved in formation of coats such as clathrin and caveolin may also be considered as membrane associated proteins.

1.3.5. Model membranes

Because of the high complexity of natural biomembranes, simplified model membranes are used to characterize properties of lipids, their supramolecular aggregates or their interaction with a broad variety of peptides. Liposomes are artificial lipid vesicles composed of concentric lipid bilayers that enclose an intravesicular water compartment. These model membranes were first produced in 1965 by Bangham and co-workers [90]. When exposed to water, bilayer-forming lipids spontaneously form multilamellar bilayers with diameter varying from 200 nm to several microns. Multilamellar vesicles (MLVs) are heterogeneous both in size and shape and thus are undesirable for many applications. Generally more homogenous liposome populations are achieved by exposing the lipid dispersion to either ultrasonication so as to obtain small unilamellar vesicles (SUVs,

1. Introduction and general objectives

diameters < 50 nm) or extrusion through polycarbonate filters with small pores to produce large unilamellar vesicles (LUVs), with diameters approx. 50-200 nm depending on the filter pore diameter .

Eukaryotic cells have typically diameters of approximately 10-100 μm being much larger than SUVs or LUVs. Size difference may cause misinterpretations in experiments, which are sensitive to membrane curvature and lipid packing conditions. From this point of view, the giant unilamellar vesicles (GUVs), prepared by electroformation [91] or by solid hydration method [92], with diameters from 5 to 200 μm represent more cytomimetic model system [93], [94].

1.3.5.1. Giant unilamellar vesicles (GUVs)

Giant unilamellar vesicles (GUVs) have been extensively used in recent years as model systems to study, *e.g.*, the lateral structure and mechanical properties of membranes, considering the effect of lipid-lipid, lipid-DNA, lipid-peptide and lipid-protein interactions. GUVs have the advantage of being geometrically analogue to living cells, due to their size of a few tens of micrometers [94]. Due to the possibility of visualizing single GUV, the problem of shape and size heterogeneity and the presence of multilamellar vesicles are excluded. Because of their similarity to cells, they are used to study mechanical and elastically properties of membranes [95]. GUVs can also be used as micro reactors; for instance, by the microinjection technique, targeted enzymatic-catalyzed reactions can take place inside the vesicles [96].

GUVs are also applied in medicine and physiology, to study muscular activity, by building GUVs from muscle tissue membranes, and monitoring the activity of glucose transporters. Also, signal transduction pathways and the influence of toxins could be studied with the aid of GUVs. Native membranes can build GUVs too, *e.g.* pulmonary surfactants [97].

Several preparation methods for GUVs have been tested over the years: freeze-thawing and dehydration-rehydration of small vesicles followed by fusion in bigger vesicles or the largely applied electroformation method [92]. In all cases the lipid film is swollen in an aqueous environment (Figure 1.12). In the electroformation method a low-voltage electric field can induce lipid swelling and liposome formation. The disadvantage of this method

1. Introduction and general objectives

is the fact that the yield of GUVs and their size decrease strongly when ions (salt) are present in the aqueous solution.

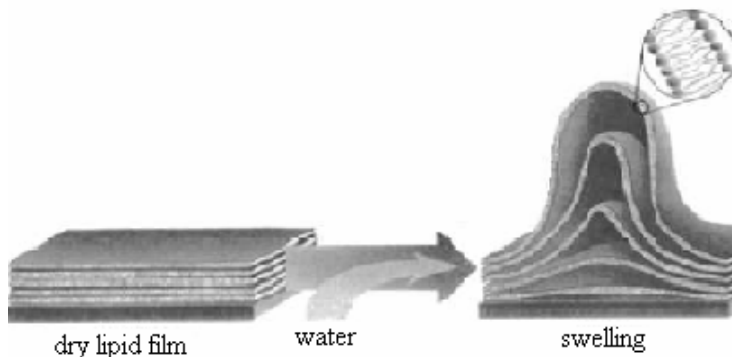


Figure 1.12: Principle of lipid swelling (taken from www.avantlipids.com)

The mechanism of GUVs electroformation is not totally clarified, although several effects of the external electric field on lipid swelling and vesicle formation have been suggested. The diameter of the electroformed GUVs highly depends on the lipid composition, swelling medium and the external AC field parameters (0.2-10 V), which give the amplitude of the electro-osmotic vibration and subsequently the membrane tension of a GUV immediately upon its formation [98]. For example, for POPC/cholesterol, the optimal conditions for the formation of GUVs were 1.5 V at 10 Hz. In addition, presence of more than 50 mol % cholesterol drastically inhibits the formation of GUVs [98]. The addition of high salt concentrations strongly reduces the formation of giant vesicles. In case of LiCl, NaCl, or KCl, the limiting concentration seems to be 10 mM, while the maximal concentrations for MgCl₂, CoCl₂, and CaCl₂ are 1.7, 1.0, and 0.2 mM, respectively [99]. The predominating mechanism of electroformation is most likely the electro-osmotic periodic movement of the water medium at the water-electrode interface. These vibrations are directed perpendicularly to the electrode surface, where the initial lipid film is deposited. The vibrations pull lipid lamellae off the electrode causing their separation and growth (Figure 1.12). At this stage the contact area is increased, and destabilizing due to the AC-field through electro osmotic vibrations takes place. Thus, the neighbour vesicles fuse together into larger ones [97], become spherical and within a few minutes some of them will eventually separate from the electrode.

1.4. Motivation of the study

TAT peptide is a promising tool for biological sciences, medicine and technology due to its attractive property to deliver cargoes molecules into living cells. Hence, it is important to clarify the mechanism of membrane translocation in order to control and develop this property.

The starting point and the motivation for the present study rely on the controversy regarding the possible mechanisms of TAT peptide internalization. Descriptions of the internalization process vary from energy-independent cell penetration of membranes to endocytic uptake: clathrin-independent endocytosis [7], caveolae-mediated endocytosis [9] or macropinocytosis [10]. Regarding the passive translocation, three mechanisms were suggested for charged peptides to cross the hydrophobic barrier of a biological membrane without utilizing an active transport system. One possibility is direct membrane penetration. An alternative hypothesis is the binding of TAT to negatively charged lipids and disruption of the bilayer structure by formation of inverted micelles resulting in their traversing into the cytoplasm [17]. Thirdly, a translocation similar to the action of antibiotic peptides has been suggested for TAT: the toroidal pore, barrel-stave model or the carpet model [21], [6], [22]. Experiments with genetically modified systems to suppress the endocytic internalization demonstrated that the transduction of TAT into living cells is not dependent on any endocytic or pinocytic events. Also, TAT was not excluded from cells that were transferred to 4 °C, a state where all possible endocytic pathways are inhibited. Recently, a pore formation, similar to the antibiotic peptides, was suggested by molecular dynamics simulations and black lipid experiments for TAT peptides.

In any case, a consensus regarding the uptake mode has not been reached. Therefore, the present study attempted to identify the factors defining an efficient membrane penetration and thus to elucidate the passive mechanism of TAT peptides translocation.

The interaction of the peptide with membranes was studied previously with different techniques [100]. Circular dichroism (CD), Fourier transform infrared spectroscopy (FTIR) or nuclear magnetic resonance (NMR) were applied to identify the secondary structure of the peptides in membranes. Mass spectrometry was used to observe the non-

1. Introduction and general objectives

covalent complexes between lipids and peptides or proteins. Atomic force microscopy (AFM) allows the observation of nanometre-sized particles and provides information on the topological organization of lipids membrane after peptide addition. Electrophysiological measurements offer information about the ability of CPPs to induce pore formation when incorporated into lipid bilayers. Also fluorescence measurements as fluorescence transfer and quenching were used to find information on the positioning of the fluorophore within the hydrophobic phase of the membrane bilayer [100].

In spite of the fact that numerous studies exist on the structures which are adopted by peptides in solution and in or at membranes, not much is known about their mobility on or within membranes. This thesis applies for the first time single molecule tracking using high-speed video fluorescence microscopy to analyse TAT dynamics on well defined membrane model systems. Obviously, cell membranes and GUVs are systems very different, but the experiments in this thesis attempt to create a model system with biological relevance. Mammalian cell membranes are comprised mainly from PC, PE, PS and cholesterol, so the same phospholipids were chosen for the GUVs composition. At the same time, the system was kept as simple as possible to answer specific questions concerning the basic principles of peptide-membrane interaction and translocation mechanism of TAT peptide through the membranes.

2. Materials and Methods

2.1. Peptides

Probe	Company
Biotin-Ahx-YGRKKRRQRRR molecular mass, 1.87 kDa	Peptide Specialty Laboratories GmbH (Heidelberg, Germany)
5,6-TAMRA-RRRQRRKKRG molecular mass, 1.81 kDa	Peptide Specialty Laboratories GmbH (Heidelberg, Germany)
Alexa Fluor 647-RRRQRRKKRG molecular mass 2.2 kDa	Peptide Specialty Laboratories GmbH (Heidelberg, Germany)
KILRGVSKKIMRTFLRRISKDILTGKK-C (Dy647-ME)-NH ₂ , molecular mass 4.05 kDa	Biosyntan (Berlin, Germany).
LRRISKDILTGKK-C(Dy647-ME)-NH ₂ molecular mass 2.4 kDa	Biosyntan (Berlin, Germany)
LRGISKKIDRTLK-C(Dy647-ME)-NH ₂ molecular mass 2.4 kDa	Biosyntan (Berlin, Germany).
Purity of TAT peptides > 97%; Purity of NKCS peptides > 95%	

2.2. Lipids

The phospholipids 1,2-dipalmitoyl-*sn*-glycero-3-phosphocholine, 1,2-dioleoyl-*sn*-glycero-3-phosphocholine, 1,2-dipalmitoyl-*sn*-glycero-3-phospho-L-serine, 1,2-dioleoyl-*sn*-glycero-3-phospho-L-serine, 1,2-dioleoyl-*sn*-glycero-3-phosphoethanolamine, 1,2-dipalmitoleoyl-*sn*-glycero-3-phosphoethanolamine, 1-palmitoyl-2-oleoyl-*sn*-glycero-3-phosphoethanolamine, 1-palmitoyl-2-oleoyl-*sn*-glycero-3-[phospho-*rac*-(1-glycerol)] and cholesterol were purchased from Sigma-Aldrich (Germany).

2.3. Fluorescent tracers

Probe	Company
TR-DHPE	Invitrogen GmbH (Karlsruhe, Germany)
DiI-C ₁₈	Sigma-Aldrich (Schnelldorf, Germany)
Bodipy-PC	Invitrogen GmbH (Karlsruhe, Germany)
FITC-dextran, molecular mass, 4 kDa and 40 kDa	Invitrogen GmbH (Karlsruhe, Germany)
Lucifer Yellow molecular mass, 386 Da	Invitrogen GmbH (Karlsruhe, Germany)
Alexa Fluor 488-maleimide molecular mass 643 Da	Invitrogen GmbH (Karlsruhe, Germany)
Alexa Fluor 546 molecular mass, 1.08 kDa	Invitrogen GmbH (Karlsruhe, Germany)
Alexa Fluor 647-maleimide molecular mass, 1.3 kDa	Invitrogen GmbH (Karlsruhe, Germany)
Dextrans molecular mass, 3 kDa and 70 kDa	Invitrogen GmbH (Karlsruhe, Germany)

2.4. Chemicals

The sugars glucose and sucrose were purchased from Sigma-Aldrich (Schnelldorf, Germany). The salts sodium chloride (>99% purity), calcium chloride, calcium carbonate and magnesium chloride, were obtained from Carl Roth (Karlsruhe, Germany) and PBS from Biochrom AG (Berlin, Germany). The solvents chloroform and methanol were purchased from Merck (Darmstadt, Germany) and from Acros Organics (United Kingdom) respectively.

2.5. Electroformation of giant unilamellar vesicles

In this study, GUVs were created by electroformation according to [91], [94]. All phospholipids were dissolved in chloroform or chloroform/ methanol 2:1 at a concentration of 1.27 mM. The lipids were mixed in different compositions and ratios to obtain GUVs with different properties (see Results for mixtures details). 20 μ l of the respective lipid mixture dissolved in chloroform (or chloroform/methanol) were deposited on an indium tin oxide (ITO) coated cover slip (from SPI Supplies, West Chester, PA, USA), which was then dried in a desiccator under vacuum. The dried lipid film was swollen with 235 μ l of 250 mM sucrose in bidestilled water and then covered with a second ITO cover slide. The latter was fixed on a rubber ring at a distance of 2 mm from the first one, thus creating a chamber (Figure 2.1).

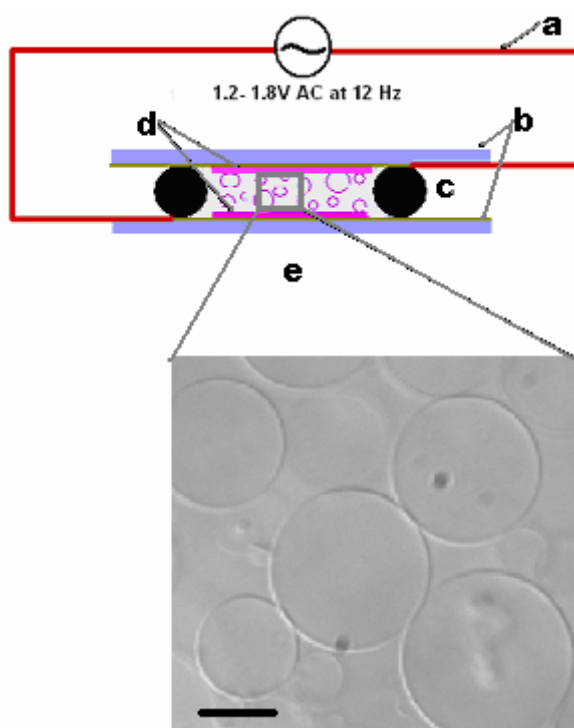


Figure 2.1: A cartoon of the electroformation chamber:
 a. copper conductive tape
 b. ITO coated slides
 c. rubber ring
 d. lipid film
 e. DIC image of GUVs.
 Scale bar, 20 μ m
 Details are given in the text.

For efflux experiments, the glucose solution from the electroformation chamber was mixed with fluorescent tracers in a concentration of 5-10 μ M.

2. Materials and Methods

For electroformation of GUVs an alternating voltage of 1.2 V at 12 Hz provided by a pulse generator was applied for 2.5 h across the chamber. Then, the voltage was raised to 1.8 V for 30 min to detach the giant vesicles from the glass slides. 100 µl of vesicles in the bulk volume were transferred with a pipette in the measurements chamber, a MatTek dish containing 300 µl of 250 mM glucose solution. The density difference between the outside (glucose) and the inside (sucrose) of the vesicles caused their sedimentation allowing their optical analysis using an inverted light microscope. Addition of 0.1 mol % of the fluorescent lipid analogs DiI-C₁₈ or Bodipy-PC to the lipid mixture before swelling allowed an observation of the vesicle formation by confocal laser scanning microscope. In case of lipid mixtures with different phases, as expected confocal imaging (Figure 2.2) of GUVs revealed a domain structure [101], because both Bodipy-PC and DiI-C₁₈ preferentially localized in DOPC-rich liquid-disordered lipid domains [102].

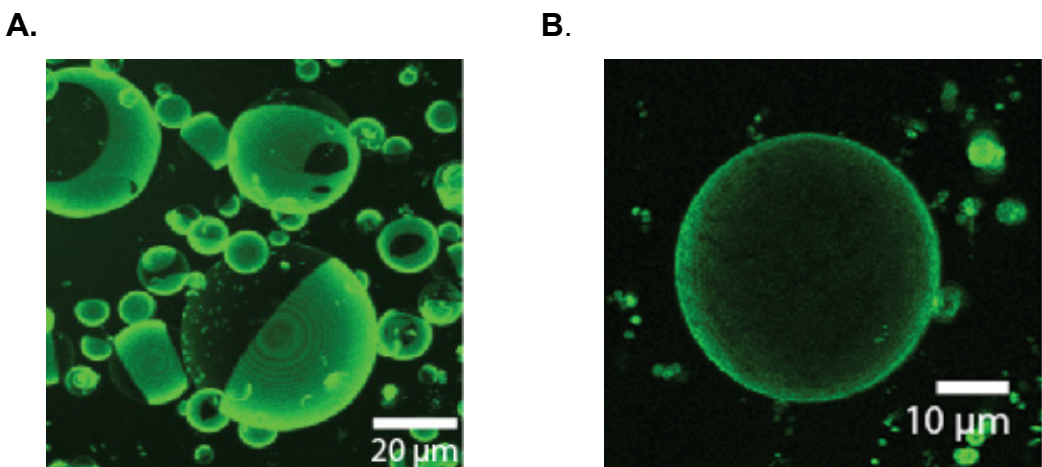


Figure 2.2: Confocal images of GUVs labelled by Bodipy-PC

(A) Confocal imaging of lipid domains in a GUV prepared from lipid mixture DOPC/DPPC/chol. Bodipy-PC was used as marker for unsaturated lipid chains; therefore, the bright domains correspond to those comprising mostly DOPC. (B) GUV prepared from lipid mixture DOPC/DPPE/chol labelled with Bodipy-PC. The thin dark stripes correspond to DPPE rich domains.

2.6. Confocal fluorescence microscopy

Confocal microscopes are integrated electronic systems, in which the light microscope is part of the imaging system containing a photon detector or camera, a computer and computer software, and electronic devices for image display, printing and storage. Epi-illumination is used, so for sample illumination and fluorescence detection, the light follows the same optical path through the objective lens. This means that the objective lens function as both condenser and objective. The optical principle of the method is presented in Figure 2.3. A laser provides a light beam that scans the specimen from top to bottom in a pattern called raster.

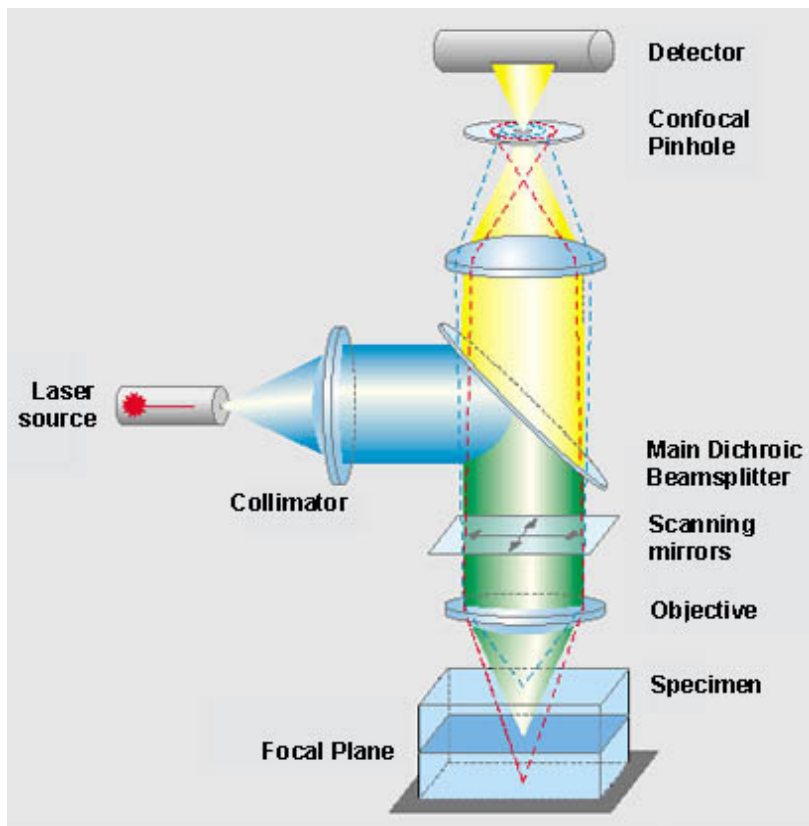


Figure 2.3: Principle of confocal microscopy, picture taken from <http://www.zeiss.de>

The fluorescence emitted by the specimen is separated from the incident light by a dichroic mirror and focused by the tube lens through a pinhole on a photomultiplier tube (PMT) [103]. A confocal image is not generated in the microscope but it is built up electronically, point by point and over time, from fluorescent signals received by the PMT

2. Materials and Methods

and accumulated in the image memory board of the computer [104]. Fluctuations in light intensity are converted into a continuously changing voltage (an analogue signal) by the PMT detector. The analogue signal is then digitized in pixels which are stored in an image frame. The computer holds the image in an image memory board until it is processed and displayed on a computer monitor. The major advantage of this technique is that fluorescence from out-of-focus planes above and below the specimen is blocked and does not contribute to the final image. This effect is due to pinhole configuration in the focal plane.

The quality of a confocal image is determined by four principal factors: spatial resolution, resolution of light intensity, signal-to-noise ratio and temporal resolution. Spatial resolution describes the smallest resolvable distance between two points in the image plane and along the z-axis. It depends on the pinhole aperture, the zoom factor, and the scan rate which are adjusted using the software. Resolution of light intensity is defined as the number of grey levels that are assigned to an image and can be controlled by adjusting the photon signal using the electronic gain and offset controls of the PMT. Signal-to-noise ratio defines the degree of image visibility or clarity and is determined mainly by the intensity of the object and background. Image brightness is affected by laser power, fluorochrome density in the specimen, numerical aperture (NA) of objective lens, confocal zoom factor, raster scan rate and fluorescence filters. Temporal resolution depends on the raster scan rate, processing rates of the detector, the analogue-to-digital converter and the computer [104].

One of the main features of confocal microscope is the ability to produce thin (0.5 to 1.5 micrometers) optical sections through fluorescent specimens [105]. Thus, by moving the specimen up and down, a 3D image can be recorded. Image information is restricted to a well-defined plane and the contrast is dramatically improved due to the reduction of background fluorescence. Furthermore, optical sectioning eliminates artefacts that occur during physical sectioning and fluorescent staining of tissue specimens for traditional forms of microscopy.

The non-invasive confocal optical sectioning technique enables the examination of both living and fixed specimens under a variety of conditions with enhanced clarity. However, it should be noted that, because confocal microscopy collects only a fraction of the total fluorescence emitted by a sample, the excitation energy required to image this

2. Materials and Methods

fluorescence must be higher than in conventional fluorescence microscopy. Therefore, the amount of photobleaching per detected photon is higher. Photobleaching should be minimized by using stable fluorophores and by operating the confocal microscope at low laser power, high detector sensitivity, and maximum objective numerical aperture.

Confocal fluorescence microscopy has been widely used in cell biology; single living cells and cellular processes can be studied by this technique, *e.g.* for visualization of organelles, distribution of electrical potential, pH imaging, calcium imaging, etc. [106].

In this study, GUV formation and peptide binding to GUVs were examined by a confocal laser scanning microscope (LSM 510 Meta from Carl Zeiss, Jena, Germany) equipped with a water immersion plan apochromat 63X objective lens (NA 1.2) at room temperature. DiI-C₁₈, TR-DHPE and R-TAT were excited with the 543 nm line of a He-Ne laser, while AF-TAT was excited using a red He-Ne laser emitting at 633 nm. For detection of AF 488 or fluorescein, the 488-nm line of an argon ion laser was directed over an HFT UV/488 beam splitter, and fluorescence was detected with a BP 505–550 band pass filter. For the simultaneous detection of fluorescein-labelled dextran molecules and Alexa Fluor 647 labelled peptides, the 488 nm light of an argon ion laser and the light of a 647 nm He-Ne laser were directed over an HFT UV/488/543/633 beam splitter, and fluorescence was detected using an NFT 545 beam splitter in combination with a BP 505–530 band pass filter for fluorescein detection and an LP 650 long pass filter for Alexa Fluor 647 detection.

2.7. Single molecule microscopy

The first single particle tracking (SPT) experiments were done on cell membranes [107] and devices for the detection and observation of signals emitted by single dye molecules have been developed in the last 20 years. In SPT, computer-enhanced video microscopy is used to track the motion of proteins, peptides or lipids on the membrane surface. Active transport in living cells occurs at the speed of several micrometers per second, Brownian motion of cell components ranges from diffusion constants of ~100 $\mu\text{m}^2/\text{s}$ for proteins in solution, over ~1 $\mu\text{m}^2/\text{s}$ for lipids in bilayers, to values smaller than 10^{-4} $\mu\text{m}^2/\text{s}$ for

2. Materials and Methods

immobilized membrane proteins [108]. In most cases, a millisecond time-resolution is required to resolve sub-micrometer displacements. In single molecule fluorescence microscopy (SMF) the achievable localisation precision depends only on the signal-to-noise ratio (SNR) and the stability of the optical setup in our case being between 20 and 40 nm [109].

Central component of the custom-built microscope set-up used in this thesis is a conventional wide-field epifluorescence microscope from Zeiss (Axiovert 200TV, Carl Zeiss, Jena, Germany, Figure 2.4). The illumination is achieved by three lasers: a Sapphire 100 DPSS-laser with 488 nm (Coherent, Santa Clara, CA, USA), a frequency doubled Nd-YAG laser and a HeNe-Laser emitting at 532 and 635 nm, respectively and their beams are coupled into an optical mono-mode fibre (Pointsource, Hamble, UK) after passage through an acoustic-optical tuneable filter (AA Opto-Electronic, Orsay, France) [109].

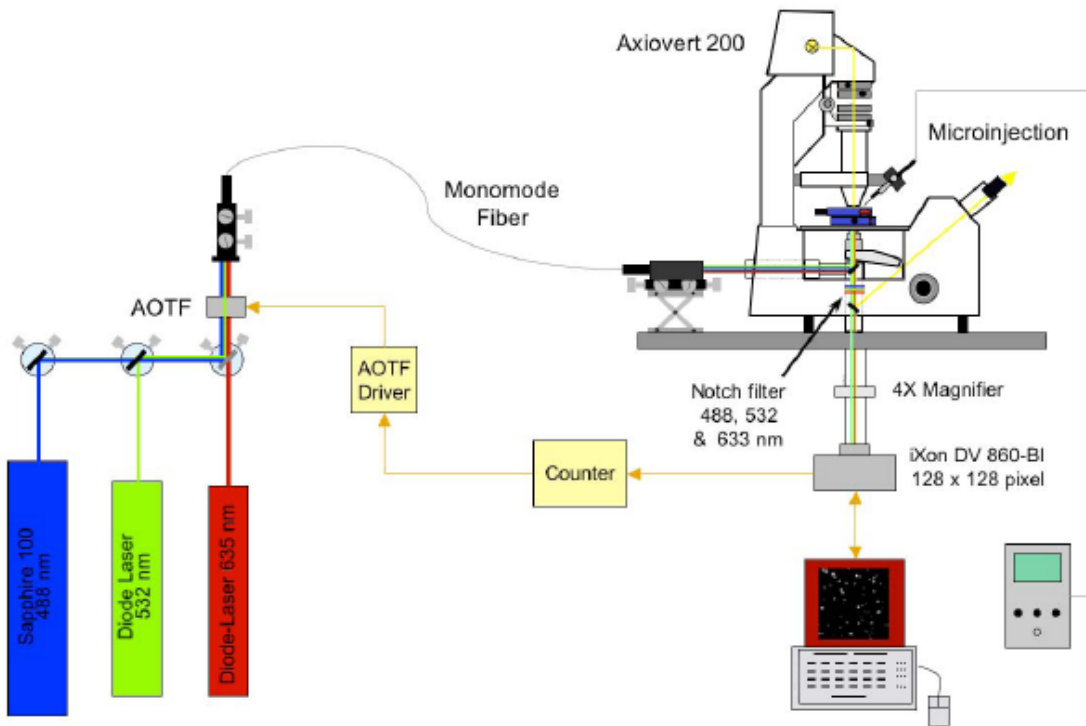


Figure 2.4: Setup for single molecule fluorescence microscope [109]

A high pressure HBO lamp can be used for illumination of the complete field of view. The emitted fluorescence light is separated from the excitation light by a triple dichromatic beam splitter, which reflects the three excitation lines onto the sample, while the three

2. Materials and Methods

fluorescence bands are transmitted to the detection system via three Notch filters extinguishing remaining excitation light (Semrock, Rochester, NY, USA) [109]. An iXon BI DV-860 (Andor Technology, Belfast, Northern Ireland) electronmultiplying CCD camera is used for image acquisition with a pixel size of $24 \times 24 \mu\text{m}^2$. The microscope is equipped with a 63X NA 1.2 water immersion objective lens in combination with a 4X magnifier in front of the camera. The pixel size is 95.2 nm and the total observation field has a size of $(12.2 \mu\text{m})^2$. Laser illumination can be adjusted so the bleaching of the sample is minimised with a custom-built, programmable electronic counter, which allows modulating the laser power via the AOTF driver. In our experiments fluorescence was excited with laser light (irradiance of 0.5 kW/cm^2), which was coupled into the epi-illumination light path of the microscope by an optical monomode fibber.

Single fluorescently labelled molecules can be imaged microscopically as diffraction-limited spots. Their intensity distribution can be approximated by a two-dimensional Gaussian function [110], [111]. Thus, the localization of the very centre of the Gaussian corresponding to fluorescent molecule position can be determined with high precision by a fitting process (Figure 2.5). In this way, the localization precision may reach a few nanometres under optimal conditions. Thereby, fluorescence microscopy allows us to follow the traces of single molecules in time with a very high spatial precision.

The technique has mostly been applied in analyzing the movement of single receptors and lipid molecules in biological membranes ([108], [81]). It was recently extended to study single-molecule mobility within solution and the interior of mammalian cells, like nucleocytoplasmic transport of single fluorescent cargo molecules or the mobility of specific intranuclear proteins [111].

In contrast to conventional techniques applied to study molecular mobility such as fluorescence correlation spectroscopy (FCS) or fluorescence recovery after photobleaching (FRAP) techniques, SMF microscopy can well discriminate multiple forms of mobility in heterogeneous systems. For high single molecule detection, the reduction of background fluorescence, optimisation of light transmission in the microscope, and high-speed CCD camera systems for signal detection in combination with digital image processing are required [109].

2. Materials and Methods

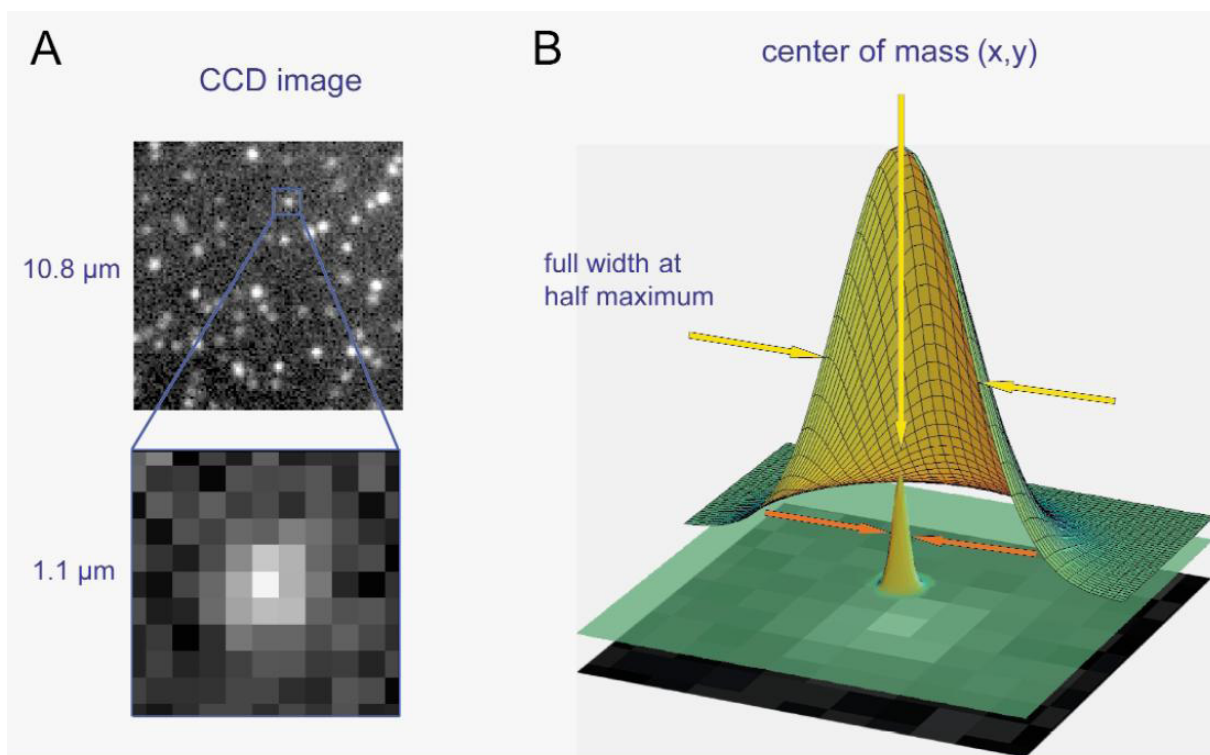


Figure 2.5: Nanolocalization of single molecules: (A) Image of single surface-attached fluorescence labelled Oyster 565 protein molecules, image size $10.8 \times 10.8 \mu\text{m}^2$. (B) The surface plot of 2D-Gaussian corresponding to intensity distribution (greyed image, below) localise the centre of mass with a precision (orange arrows) significantly smaller than the half-width of the diffraction limited spot size (yellow arrows), [112]

The aim of SPT experiments was to follow the single molecule trajectories of lipid tracer molecules (DiI-C₁₈ and TR-DHPE), and labelled TAT and NKCS peptides in order to find their diffusion coefficients. All the experiments were performed at room temperature. For R-TAT and AF-TAT peptide analysis a single frame integration time of 10 ms at a frame rate of 100 Hz was used, whereas an integration time of 33 ms at a frame rate of 30 Hz was used for lipid tracers and Dy-NKCS imaging. All single-molecule tracking experiments were performed on the top surface of freshly prepared GUVs. To adjust the correct focal plane the radius of the GUV at the equatorial level was measured employing DIC and a grid with known dimensions within the eyepiece. Then, the focus was shifted with a distance corresponding to the GUV radius to reach the top plane of the spherical GUV. Only on top surface single molecule signals could be observed using fluorescence mode. In solution the particles have a very high diffusion which can not be detected by the camera. Since the radius of the GUVs was at least 20 μm , the curvature of the surface was

small enough to allow the imaging of an extended region of top GUV. The axial resolution was about 1 μm . The circular region on the GUV top starts from a diameter of about 14 μm , so larger than the observation field (12.2 μm). From this field usually 1000-2000 single frames were recorded in a single movie. For each experimental situation a total of three independent experiments comprising 10-15 movies were obtained and the trajectory data were pooled.

2.7.1. Trajectory analysis

A major advantage of SPT is the ability to sort the trajectories into various modes of motion of individual molecules. Diffusion coefficients depend on size and shape of molecules, their interaction with the medium (solvent) and the viscosity of medium. The mean square displacement (MSD) is a measure of the averaged distance that a molecule travels. A linear relationship between MSD and time indicates free Brownian motion. In most cases motion in the biological membranes is not limited to pure diffusion. That is due to domain and possibly rafts formation. So, anomalous or confined diffusion to the point of immobile fractions are also observed (Figure 2.6). In this case, MSD dependence on time is characterized by a sublinear increase. FRAP experiments on phospholipids membrane revealed anomalous diffusion and for two components, mobile and immobile fractions were identified [81]. The lipids diffusion in GUVs depends strongly on membrane composition and FCS was used to evaluate the role of cholesterol in changing the lipid mobility in raft-like domains [113], [102].

In this thesis single molecule signals from individual frames were identified and tracked with Diatrack 3.02 (Semasophot, Chavannes, Switzerland). This is a commercial image processing program for the localization of single objects and construction of their trajectories. All further data processing was performed with ImageJ [114] and Origin 8.0 (OriginLab Corp., Northampton, MA, USA).

2. Materials and Methods

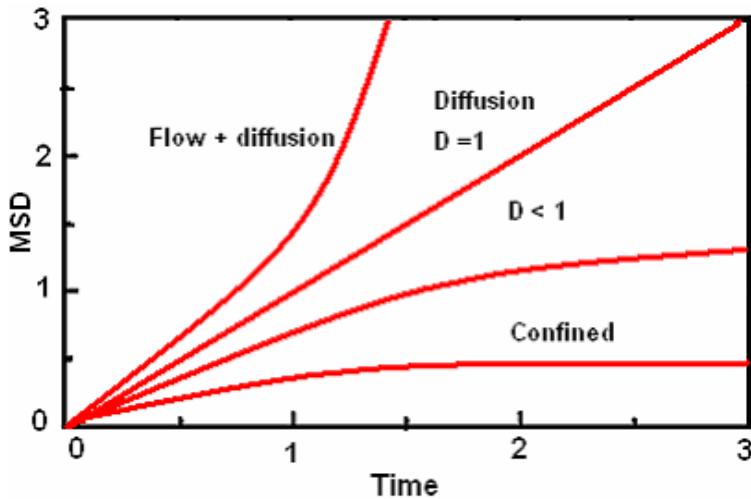


Figure 2.6: MSD as a function of time t for simultaneous diffusion and flow, pure diffusion, diffusion in the presence of obstacles, and confined motion (modified from [108])

Each single-molecule trajectory was defined by coordinates (x_i, y_i) . The running frame number was denoted by i , where $1 \leq i \leq N$ and N stands for the number of frames in which the molecule was observed. For each trajectory the squared displacements $r^2(n t_c)$ were computed with t_c representing the imaging cycle time (inverse frame rate), and n the difference of the running index. Therefore, $n t_c$ was the time between two observations of the same molecule. By averaging the square displacements for identical values $n t_c$ the mean square displacements (MSD), $\langle r^2(n t_c) \rangle$ were obtained.

For two-dimensional Brownian motion the MSD is given by:

$$\langle r^2(n t_c) \rangle = 4D(n t_c) \quad (1)$$

Plotting MSD against time, the diffusion coefficients can be derived from single molecule trajectories, if they are long enough to generate significant mean values. Generally, the MSD values of many different trajectories were averaged for identical values of $n t_c$ to improve statistics. When the population contains different mobility fractions, a joint analysis of the trajectories according to Eq. 1 is not suitable and a jump distance analysis is more appropriate.

2.7.2. Jump distance analysis

The jump distance analysis is a method adequate to analyse heterogeneous populations. When a particle starts at a given position, the probability that it will be encountered in a distance r within a shell of width dr from the start position at time t is given by:

$$p(r,t)dr = \frac{1}{4\pi Dt} e^{-r^2/4Dt} 2\pi r dr \quad (2)$$

Eq. 2 is valid for a single particle species diffusing in two dimensions [115]. Experimentally, this probability distribution function can be approximated by a frequency distribution, quantifying the jump distances within respective intervals $[r, r+dr]$ travelled by single particles after $n t_c$. When several particle subspecies with different mobilities are present or particles change their diffusion speed during their trajectory, the jump distance distributions cannot be described by eq. 2 with a single diffusion coefficient. However, such particle populations can be analysed by curve fitting using more than one term according to eq. (3). A jump distance distribution containing contributions from two different subspecies is described by,

$$p'(r,t)dr = \sum_{j=1}^2 \frac{M f_j}{2D_j t} e^{-r^2/4D_j t} r dr \quad (3),$$

where M is the total number of jumps considered in the analysis, and f_1 and f_2 denote the relative fractions with diffusion constants D_1 and D_2 , respectively.

In this study, in analysed jump distributions the distances between molecular positions in successive frames were evaluated.

2.8. Sample preparation for light microscopy

To study mobility of lipids in the bilayer, GUVs labelled with TR-DHPE or DiI-C₁₈ at 10⁻⁷ mol % were diluted (1:4) in the experimental chamber (MatTek dish) containing glucose or glucose/NaCl solution. To verify the changes induced by peptides the labelled GUVs were added in a glucose or glucose/NaCl solution containing B-TAT or unlabelled NKCS.

For measurements focusing on the interaction of TAT or NKCS with the GUVs, the glucose or glucose/NaCl solutions were mixed with the peptides before adding the GUVs. Fluorescent R-TAT or AF-TAT was used at a concentration of 250 pM, or at a concentration of 100 pM in a mixture with unlabelled B-TAT at a total concentration 2 μM. Dy-NKCS peptides were used at a concentration of 500 pM for single molecule experiments. The freshly prepared GUVs in glucose solution were added with a pipette in the experimental chamber. The sample chamber had a total volume of 400 μl, and the final molar ratio of lipids to peptides in the experiment with 2 μM was 27.5/1. In the experiments using 250 pM TAT the respective molar ratio was 220000/1. For 500 pM the molar ratio NKCS/lipids is 1/110000. Incubation time of GUVs in the peptide-glucose solution before image acquisition was 30 min.

For the efflux experiments, GUVs loaded with fluorescent tracers were diluted 1:10 in glucose solution and 100 μl from the final dilution were added in the MatTek dish containing peptides solution. In case of tracers influx experiments, the dyes were mixed together with the peptide in glucose or glucose/NaCl solution.

2.9. Monte Carlo simulations

Computer simulation has become an established method of research in science and a useful tool in complementing both analytical theory and experiment. Monte Carlo is a computational model used for simulation of atomic and molecular assemblies. In our study this method is applied to analyse the interaction between peptides and lipid membranes

2. Materials and Methods

[116]. Typically, the Monte Carlo methods are based on reduced representation of the peptide-membrane system, in contrast to the all-atom representation used in molecular dynamics simulations. The reduced representation enables comprehensive sampling of peptide conformations and locations in the membrane in an accelerated manner.

The Monte Carlo simulations were performed with the help of Yana Gofman from GKSS Research Center, Geesthacht, Germany. The used model assumes that the hydrocarbon region of the membrane bilayer is represented as a smooth hydrophobic profile of 40 Å width (Figure 2.7). For anionic membranes, a negative surface charge, representing the molecular fraction of PS, is located on both sides of the membrane at a distance of 15 Å from the midplane, corresponding to the location of the lipid phosphate groups.

The peptide structure is taken from Protein Data Bank (PDB) and it is represented by two interaction sites (α -carbon atom and side chain interaction centre) based on specific structure and energy characteristic of the aminoacids [117].

The total free energy of membrane association (ΔG_{total}) is calculated as the difference between the free energies of a peptide in the aqueous phase and in the membrane, using the following equation [116]:

$$\Delta G_{\text{total}} = \Delta G_{\text{con}} + \Delta G_{\text{sol}} + \Delta G_{\text{imm}} + \Delta G_{\text{lip}} + \Delta G_{\text{def}} + \Delta G_{\text{coul}} \quad (4), \text{ where}$$

ΔG_{con} is the change in the free energy due to membrane-induced conformational changes,
 ΔG_{sol} is the free energy of transfer of the peptide from the aqueous environment to the membrane,

ΔG_{imm} represents the immobilization of the peptide in the membrane,

ΔG_{lip} is the free energy due to the change in the conformational freedom of the lipid chains,

ΔG_{def} accounts for the membrane deformation associated with peptide incorporation into the membrane,

ΔG_{coul} is the Coulombic attraction between charged amino acids and the (negative) membrane surface charge.

2. Materials and Methods

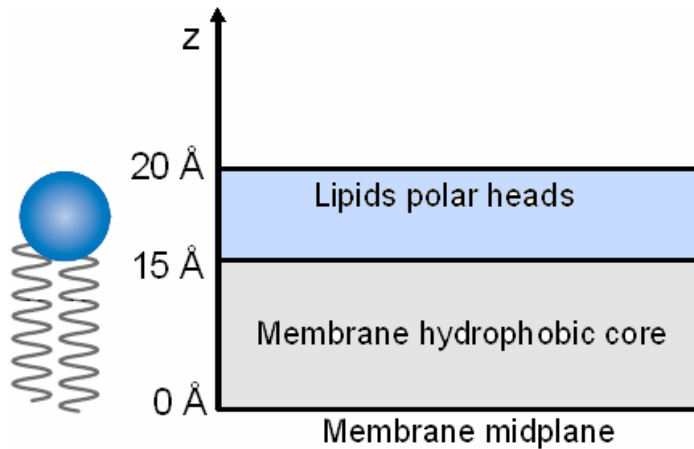


Figure 2.7: The model of membrane structure employed in Monte Carlo simulations

ΔG_{con} can be decomposed into contribution from short- and long-range interactions and can be calculated (in kT units) as

$$\frac{\Delta G_{con}}{kT} = \frac{\Delta H_{con}}{kT} - \frac{\Delta S_{con}}{k} \quad (5),$$

where ΔH_{con} and ΔS_{con} are the enthalpy and the entropy changes associated with the transition of the peptide from the aqueous phase into the lipid bilayer, k is the Botzamann constant, and T is the simulation temperature [117].

ΔG_{con} , ΔG_{sol} , ΔG_{imm} are calculated based on a hydrophobicity scale [117], which includes free-energy contribution from peptide solvation, immobilization and perturbation effects.

ΔG_{def} results from compression or expansion of the lipids chains after insertion of the peptide into lipid bilayer. The ΔG_{def} value is calculated based on a statistical-thermodynamic molecular model of the lipid chains and fitted a harmonic potential:

$$\Delta G_{def} = \omega(z_m - z_0)^2 \quad (6),$$

where z_m and z_0 are the actual and native widths of a monolayer, ω is a harmonic force constant related to membrane elasticity. In this case it is $z_0 = 20 \text{ \AA}$, according to the model and $\omega = 0.22 \text{ kT/ \AA}^2$ [117].

The Coulombic interactions between the peptide and the membrane are calculated using the Gouy-Chapman theory that describes the electrostatic potential in the aqueous phase near the membrane.

2. Materials and Methods

It should be noted that the Monte Carlo computational model has inherent limitations due to its simplification of the peptide-membrane interaction. First, the model treats the interaction of a single peptide molecule with the lipid bilayer and is not suitable in this form to study peptide concentration effects. Second, the model membrane is planar and membrane curvature effects, which are anticipated in the presence of *e.g.* PE lipids, cannot be simulated. Third, the model describing both the peptide and membrane is simplified to a representation computationally accomplishable. Also, it does not allow studies of specific peptide-lipid interactions in atomic details. Hydrogen bonds and salt bridges between the peptide and lipid, as well as the exact stereochemistry of the interaction, are not taken into account explicitly.

3. Results and discussion

The experimental results providing the framework of this thesis are divided in two intertwining parts. The first part analyses the direct interaction between TAT peptide and lipids and therefore the experiments were performed in sucrose/glucose solution with all ions excluded from the medium. Mammalian cell membranes are composed mainly from PC, PE, PS and cholesterol [70], so the same phospholipids were chosen for the GUV composition. At the same time, the system was kept as simple as possible to find specific answers concerning the basic principles of peptide-membrane interaction and the translocation mechanism of the TAT peptide through the membranes. Considering the physiological relevance of salt ions, the second part of the thesis is focused on the influence of different ions on TAT translocation efficiency.

The literature suggested and also our findings pointed to a pore formation mechanism for TAT, similar to antimicrobial peptides. Therefore, an additional study on the interaction of antimicrobial peptide NKCS with GUVs is included, too.

3.1. TAT peptide interaction with neutral and anionic membranes

To study gradually the effect of TAT peptide on model membranes of different compositions, we started with GUVs comprising neutral PC with saturated or unsaturated chains and anionic comprising PC/chol and a low content of PS (15 %).

3.1.1. Imaging and tracking of single lipid analogs within anionic and neutral GUVs

In order to obtain a reference for the measurements on neutral and anionic membranes, the dynamics of the chosen model bilayer systems was studied. For that, the lipid mobility in

3. Results and discussion

GUVEs of different lipid compositions was measured. Lipid diffusion in model membranes can well be analysed by imaging and tracking single dye-coupled lipid analogs [118], [119]. The fluorescent TR-DHPE and Dil-C18 were used as tracer molecules. Six different sets of experiments were performed using liquid-ordered GUVEs formed by DPPC and cholesterol (S_N), liquid-disordered GUVEs formed by DOPC and cholesterol (U_N), and GUVEs formed by equimolar ternary mixtures of DOPC, DPPC and cholesterol (M_N). In addition to these mixtures of neutral components we examined anionic GUVEs created by inclusion of 15 mol % DOPS or DPPS (indicated by the subscript “A” instead of “N”, see Table 3.1). The cholesterol was added to better mimic mammalian cell membranes. Besides that, it contributes to a clearer distribution of the domains in GUVEs [102]. Furthermore, incorporation of cholesterol into phospholipid membranes increases the thickness of a bilayer, reduces its elasticity, and diminishes the permeability to small water-soluble molecules [87]. Anyway, it was shown that cholesterol could induce modifications in physical properties of the membrane [120]. Therefore incorporation of cholesterol would mimic better the biomembranes.

Table 3.1: Composition of giant unilamellar vesicles (GUVEs). The designation of the respective lipid composition is given in the first column

GUVEs	Lipid Molar Ratio				
	DPPC	DOPC	Chol	DPPS	DOPS
S_N	0.5	-	0.5	-	-
M_N	0.33	0.33	0.33	-	-
U_N	-	0.5	0.5	-	-
S_A	0.425	-	0.425	0.15	-
M_A	0.283	0.283	0.283	0.15	-
U_A	-	0.425	0.425	-	0.15

3. Results and discussion

The tracer molecules were added at a ratio of 10^{-7} mol % to the lipids mixture before preparation of the GUVs. After electroformation, 100 μl of the vesicles were transferred to the microscope sample chamber containing glucose solution 250 mM. Single diffraction-limited spots of fluorescence could be observed in the single-molecule microscope, when the focal plane was adjusted to the GUVs top. Movies comprising 1000 frames were taken at a frame rate of 30 Hz. A sequence of successive movie frames is shown in Figure 3.1, which illustrates the motions of several single lipid tracer molecules within the GUV membrane. In 3.1(A) nine subsequent movie frames illustrate the motions of four single TR-DHPE molecules (marked by arrows) in a total time of 300 ms in the two-component GUVs (DOPC, DPPC and cholesterol at a molar ratio of 0.33/0.33/0.33). The field of view of a single frame was $(12.2 \mu\text{m})^2$, and contained the upper plane of a single GUV. In (B) are presented the trajectories of two-dimensional diffusion of the same four particles in GUVs membrane as determined by the tracking software. The shown area corresponds to the microscopic field of view.

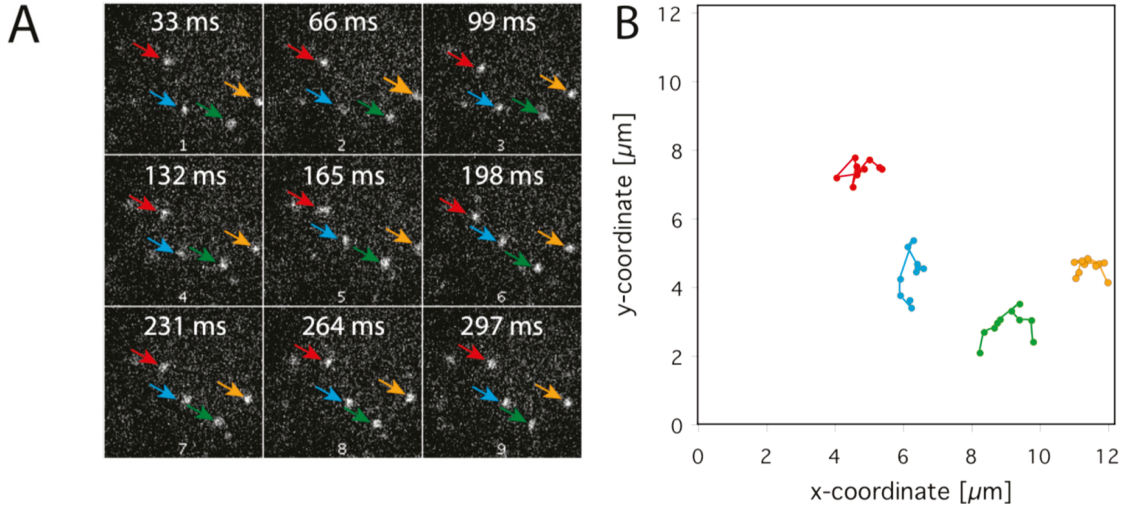


Figure 3.1: Single TR-DHPE molecules diffusing within the GUV membrane [121].

The mobility of the DHPE-TR and DiI-C₁₈ tracer molecules within the model bilayers were analysed by quantifying the single molecule mean square displacements (MSD) as a function of time according to eq. 1 from chapter 2.7.1. A linear fit to the MSD values yielded the average diffusion coefficients of the tracer molecules in the respective GUV membrane (see Figure 3.2.A). As expected, the lipid analogs diffused faster within GUVs

3. Results and discussion

known to have a disordered phase ($D = 2.7 \pm 0.05 \mu\text{m}^2/\text{s}$) compared to GUVs known to comprise an ordered phase ($D = 0.6 \pm 0.02 \mu\text{m}^2/\text{s}$). The diffusion of TR-DHPE in the M_N GUVs yielded an intermediate value of $D = 1.0 \pm 0.03 \mu\text{m}^2/\text{s}$. All results were summarized in Table 3.2.

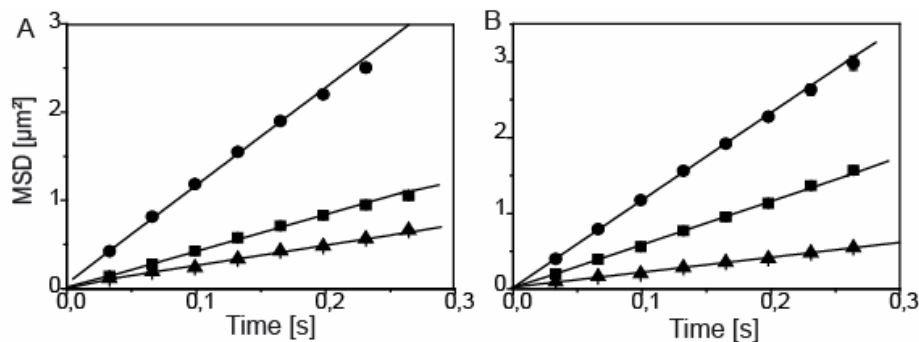


Figure 3.2: TR-DHPE diffusion on neutral and anionic GUVs

(A) MSDs of TR-DHPE molecules plotted as a function of time for neutral membranes: (\blacktriangle) data from GUVs created by DPPC/cholesterol, S_N ; (\blacksquare) DPPC/DOPC/cholesterol, M_N ; (\bullet) DOPC/cholesterol, U_N . (B) MSDs of TR-DHPE plotted as a function of time for anionic membranes: (\blacktriangle) data for GUVs generated from DPPC/cholesterol/DPPS, S_A ; (\blacksquare) DPPC/DOPC/cholesterol/DPPS, M_A ; (\bullet) DOPC/cholesterol/DOPS, U_N .

Table 3.2: TR-DHPE mobility within GUVs

Sample	D_{MSD} [$\mu\text{m}^2/\text{s}$]	$D_{1,SPT}$ [$\mu\text{m}^2/\text{s}$]	Fraction 1	$D_{2,SPT}$ [$\mu\text{m}^2/\text{s}$]	Fraction 2
S_N	0.6 ± 0.02	0.66 ± 0.02	1	-	-
M_N	1.0 ± 0.03	0.70 ± 0.02	0.82	2.55 ± 0.07	0.18
U_N	2.7 ± 0.05	2.53 ± 0.05	1	-	-
S_A	0.49 ± 0.03	0.55 ± 0.01	1	-	-
M_A	1.43 ± 0.07	0.87 ± 0.06	0.64	2.48 ± 0.04	0.36
U_A	2.90 ± 0.11	2.54 ± 0.05	1	-	-

Similar values for the diffusion coefficients in liquid-ordered and liquid-disordered GUVs were obtained with the tracer Dil-C₁₈. The results are presented in Table 3.3.

3. Results and discussion

Table 3.3: DiI-C₁₈ mobility within GUVs

Sample	D _{MSD} [μm ² /s]	D _{1,SPT} [μm ² /s]	Fraction 1	D _{2,SPT} [μm ² /s]	Fraction 2
S _N	0.5±0.02	0.44±0.01	1	-	-
M _N	1.4±0.05	0.60±0.02	0.4	1.83±0.05	0.6
U _N	2.1±0.03	1.84±0.03	1	-	-
S _A	0.65±0.01	0.50±0.02	1	-	-
M _A	2.85±0.02	0.64±0.02	0.3	2.44±0.03	0.7
U _A	2.98±0.05	1.88±0.05	1	-	-

However, confocal analysis of GUVs with mixed lipids suggested a phase separation of the ordered and disordered domains (see Figure 2.2 for a M_A GUV from chapter 2). In this case the lipid dynamic is not properly described by one component and two different diffusion coefficients are expected.

In an MSD analysis molecules with distinct mobility cannot be differentiated, but this can be achieved by a so-called jump distance analysis. In this analysis the jumps performed by a molecule from frame to frame are evaluated. The distribution of jump distances follows a "stretched" Gaussian distribution according to eq. 2 (see chapter 2.7.1) for a single diffusive species. Figures 3.3 (A) and (C) show the jump distance distributions for the neutral liquid-ordered and -disordered single component GUVs, respectively. The distributions could well be described by eq. 2, and yielded comparable diffusion coefficients as the MSD analysis for single species (see Table 3.2). However, for the jump distance distribution of the neutral M_N GUV a fit according to eq. 2 did not match the data. If differently mobile molecules or molecules with different mobility in domains with distinct viscosity occur, more than one expression according to eq. 2 must be evaluated. In the case of the M_N GUVs we yielded an excellent description of the data with two diffusion terms according to eq. 3 (Figure 3.3 (B)).

3. Results and discussion

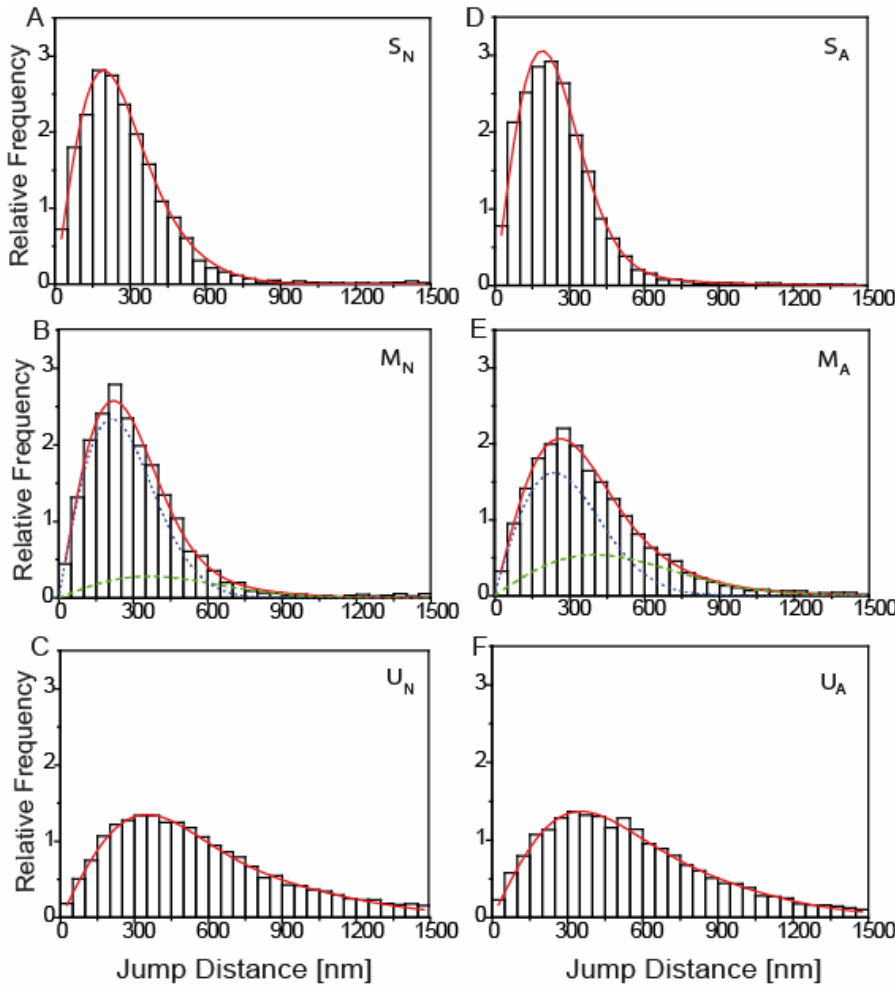


Figure 3.3: Analysis of TR-DHPE diffusion on neutral and anionic GUVs [121] (A, B and C) Jump distance analysis for TR-DHPE in neutral GUVs. (D, E and F) Jump distance analysis for TR-DHPE in anionic GUVs.

As suggested by the confocal analysis of the mixed GUVs it could be concluded that TR-DHPE and Dil-C₁₈ were moving in two different spatially separate domains exhibiting different viscosities corresponding to two diffusion coefficients. These were $D_1 = 0.70 \pm 0.02 \text{ } \mu\text{m}^2/\text{s}$ and $D_2 = 2.55 \pm 0.07 \text{ } \mu\text{m}^2/\text{s}$, respectively, for TR-DHPE. Since about 80% of the jumps were observed in the more viscous liquid-ordered and only about 20% were observed in the more liquid-disordered domain, one can assume that TR-DHPE localizes preferentially in the liquid-ordered lipid domain [102]. By comparing the two diffusion constants determined in the M_N GUVs to the results of the single component GUVs, one can conclude that tracer diffusions were observed in the two spatially separated liquid-ordered and liquid-disordered lipid phases. This was in good agreement with the results of

3. Results and discussion

[101], which detected micron-scale coexisting liquid phases in GUVs. Unfortunately, it was not possible to visualize the domain structure microscopically in the GUVs used below for single-molecule imaging of TAT peptides, because of a significant spectral overlap of the available dyes for marking the domains and the spectrum of the employed fluorescent tracer molecule.

Following the analysis of lipid tracer mobility in neutral GUVs comparable measurements were performed for anionic GUVs. We imaged TR-DHPE and DiI-C₁₈ within anionic liquid-ordered (S_A) and liquid-disordered (U_A) two-component GUVs, as well as anionic four components GUVs (M_A). We found that the presence of 15 mol % of the charged lipid did neither change the phase behaviour nor the lipid tracer mobility considerably compared to neutral GUVs (see Figure 3.3 (D-F), and Table 3.2). Also in this case, TR-DHPE diffuse faster within GUVs with an unordered phase with a diffusion coefficient of D= 2.54 ± 0.05 μm²/s compared to GUVs, which exhibit an ordered phase, D= 0.55 ± 0.02 μm²/s. The small changes observed compared to neutral GUVs were probably due to the fact that the cholesterol mole fraction was altered to a minor extent [102].

The similar results obtained with two different lipid tracers, TR-DHPE and DiI-C₁₈ led to the conclusion that the lipid model system is stable and well described.

3.1.2. Confocal imaging of TAT peptide-GUVs interaction

To analyse the general aspects of TAT peptide's interaction with the model membranes, we incubated pre-formed GUVs with peptide/glucose solution, in different concentration of TAT. These samples were observed by confocal laser scanning microscopy for extended periods of time.

For anionic GUVs, R-TAT fluorescence at the GUV surface strongly increased upon incubation with 1 μM peptide within 30 min. After 5 min a distinct labelling of anionic GUVs by R-TAT already could be recognized. Figure 3.4 shows images of exemplary M_A GUVs at time points of 5, 15 and 30 min. In order to simplify the detection of the GUVs Figure 3.4 (A) displays images obtained with DIC. Figure 3.4 (B) shows the sample in the

3. Results and discussion

rhodamine fluorescence channel. R-TAT does not translocate the M_A GUVs, but just accumulates on the GUV membranes. Similar results were obtained for AF-TAT and GUVs made from all lipid mixtures used in this study.

A surface labelling due to TAT binding could also be observed for neutral GUVs, although the fluorescence intensity was clearly weaker. When the R-TAT concentration was increased to 2 μ M, a distinct labelling of the GUVs was already clearly visible after 3 min for anionic and neutral GUVs. Again the labelling of the anionic GUVs was stronger than that of the neutral GUVs. 2 μ M TAT was a concentration well above the threshold found for the import of TAT into living cells [29]. 1 μ M is the threshold for C2C12 myoblast cells. However, we did not detect any R-TAT fluorescence within neutral or anionic GUVs in the glucose solution. Obviously, the peptides were not able to translocate across the membrane at concentrations up to 2 μ M under the given experimental conditions.

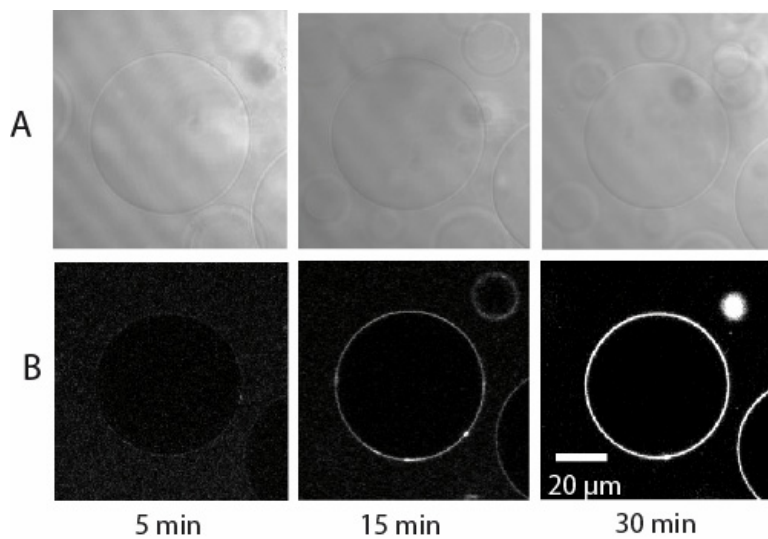


Figure 3.4: Time series of TAT peptide interaction with anionic GUVs in glucose

(A) DIC images showing the M_A GUVs; (B) Confocal fluorescence images of the GUVs incubated with 1 μ M R-TAT in the rhodamine channel.

3.1.3. Lateral mobility of single TAT peptides on the GUV surface at low concentration

In order to study mobility of TAT peptides on the membrane's surface, we incubated neutral and anionic GUVs with 0.25 nM R-TAT. Single molecule imaging was started after 30 min incubation. The concentration of the R-TAT was so low that single diffraction-limited spots of R-TAT fluorescence became visible at the GUV surface, which could well be tracked resulting in trajectories of TAT peptides on the GUV surface. The small fluorescent spots displayed a higher mobility than the lipid tracers, so the imaging rate was increased from 30 Hz to 100 Hz to catch the fast motions without blurring the single molecule signals.

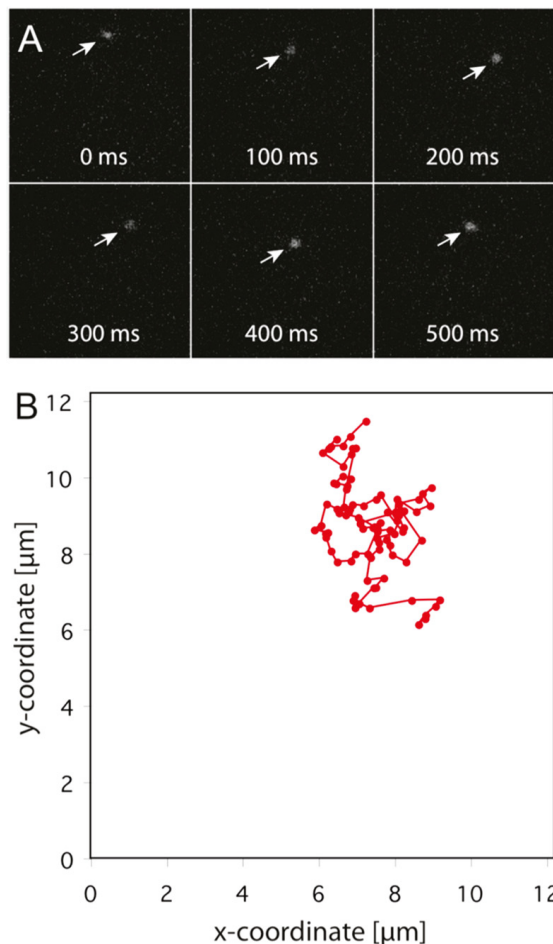


Figure 3.5: Single R-TAT peptide on the GUV surface [121]

(A) sequence of six successive movie frames illustrating the motions of R-TAT; (B) plot of the corresponding two-dimensional diffusion trajectory of R-TAT molecule

3. Results and discussion

Figure 3.5 (A) shows a sequence of six successive movie frames illustrating the motions of R-TAT over a time span of 0.51 s on anionic GUVs (DOPC/cholesterol/DOPS at a molar ratio of 0.425:0.425:0.15). Single frame integration time was 10 ms. Only every 10th image of the image sequence is presented. The field of view of a single frame was (12.2 μm)². In (B) is shown the plot of the corresponding complete two-dimensional diffusion trajectory of R-TAT molecule.

To evaluate TAT peptide mobility on the GUV surface based on single particle tracking, out-of-focus signals were sorted out using a size threshold, which was set to restrict the analysis to diffraction limited signals only corresponding to single TAT peptide molecules in focus. As described above for lipid tracer mobility, a MSD and a jump distance analysis of R-TAT dynamics on the GUV surface was performed for the same lipid compositions. The results of this analysis are shown in Figures 3.6 and 3.7. Short trajectories are problematic for the MSD analysis, because only relatively few data points contribute to the calculation of the MSD at longer times causing strong data fluctuation. Therefore, only the first 5 time points were used to determine the diffusion constant corresponding to times up to 80 ms.

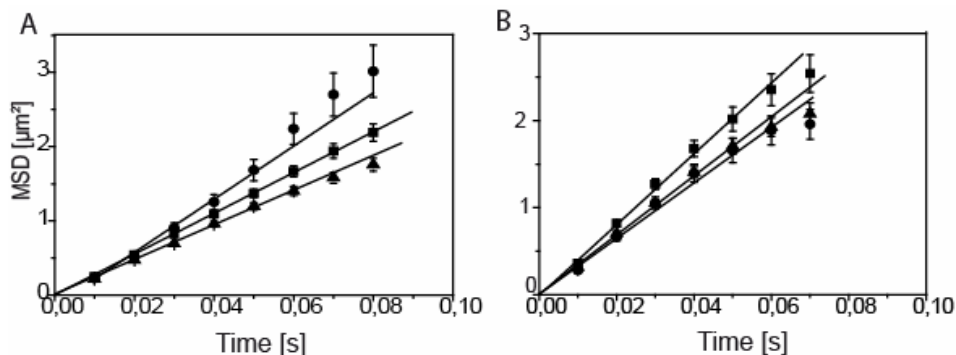


Figure 3.6: Analysis of R-TAT diffusion on neutral and anionic GUVs at low concentration (0.25 nM) (A) Plot of MSD versus time for of R-TAT on neutral membranes: (▲) represents GUVs made from DPPC/cholesterol (S_N); (■) DPPC/DOPC/cholesterol (M_N); (●) DOPC/cholesterol (U_N); (B) Plot of MSD versus time for of R-TAT on anionic membranes: (▲) represents GUVs generated from DPPC/cholesterol/DPPS (S_A); (■) DPPC/DOPC/cholesterol/DPPS (M_A); (●) DOPC/cholesterol/DOPS (U_A).

3. Results and discussion

Table 3.4: R-TAT peptide mobility on GUVs

Sample	0.25 nM R-TAT		0.1 nM R-TAT and 2 μM B-TAT	
	D_{MSD} [μm ² /s]	D_{SPT} [μm ² /s]	D_{MSD} [μm ² /s]	D_{SPT} [μm ² /s]
S _N	6.8±0.6	5.7±0.3	5.5±0.2	5.3±0.1
M _N	5.6±0.6	4.9±0.3	5.7±0.3	4.8±0.2
U _N	6.4±0.7	5.0±0.1	5.1±0.2	4.9±0.1
S _A	3.6±0.5	3.7±0.1	4.0±0.1	3.4±0.1
M _A	4.0±0.4	3.3±0.1	4.3±0.2	3.3±0.2
U _A	3.3±0.4	3.0±0.2	4.0±0.1	3.2±0.2

The MSD plot and also the jump distance histogram clearly demonstrated a significantly higher mobility of the R-TAT than the membrane-embedded tracer molecules in all GUV systems examined (Fig. 3.6, 3.7 and Table 3.4). The mobility of the R-TAT peptide on the GUV surface was virtually identical for all examined GUV compositions within the precision of the measurements, and all jump distance histograms could well be fitted by a single diffusion component. This result was in agreement with the CLSM visualization of vesicle-attached R-TAT, which was uniform on GUVs made from M_A and M_N mixtures (Figure 3.8).

3. Results and discussion

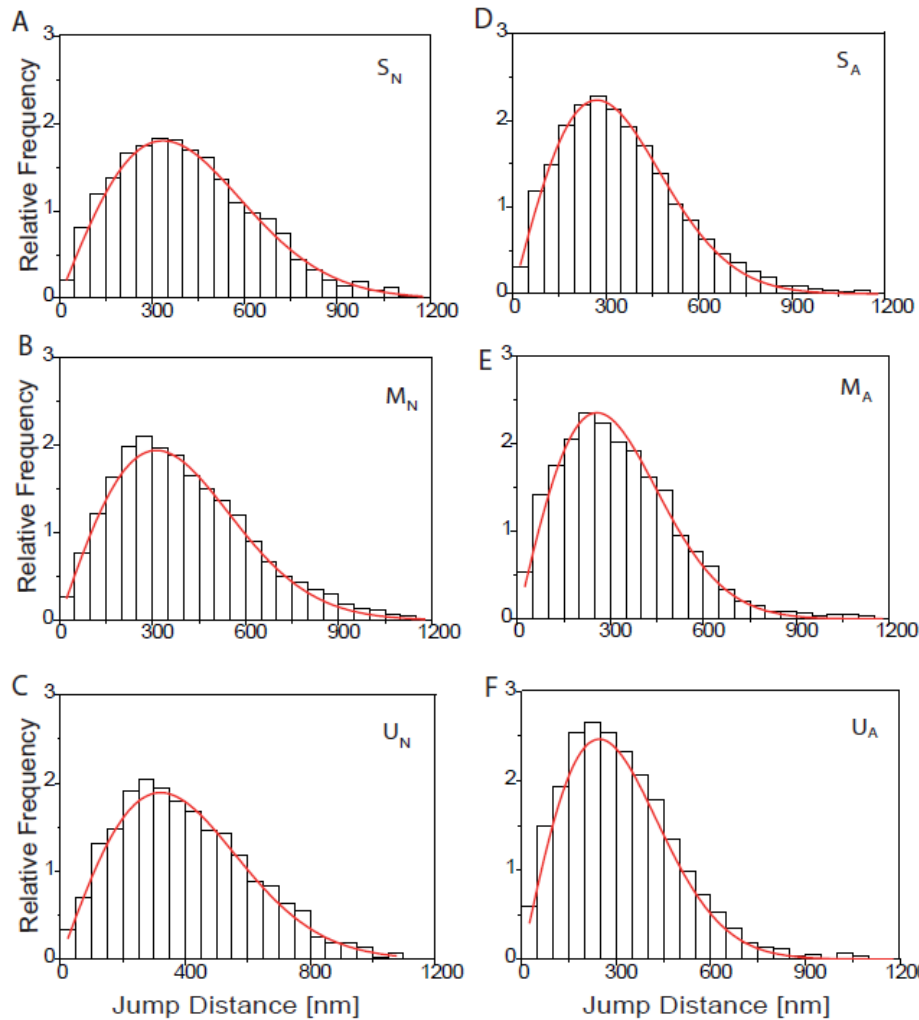


Figure 3.7: Analysis of R-TAT diffusion on neutral and anionic GUVs at low concentration (0.25 nM) (A, B and C) Jump distance analysis for R-TAT in neutral GUVs for the different GUV compositions as indicated in the plots. (D, E and F) Jump distance analysis for R-TAT in anionic GUVs for the different GUV compositions as indicated in the plots [121].

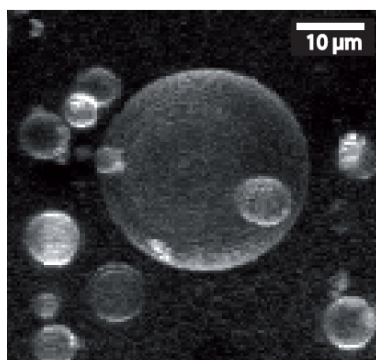


Figure 3.8 : Confocal images of GUVs labelled by R-TAT

Incubation of M_A GUVs with R-TAT in salt-free medium yielded a uniform distribution of the peptide on GUVs, independent on lipid domains.

3. Results and discussion

Obviously, TAT peptide mobility was independent of the lipid bilayer structure. A distinct difference, however, was observed for the mobility on neutral versus anionic GUVs. The diffusion coefficient of TAT on neutral GUV surfaces, $D_{N,SPT} = 6.2 \pm 0.6 \text{ } \mu\text{m}^2/\text{s}$, was significantly higher than on anionic GUVs, $D_{A,SPT} = 3.5 \pm 0.5 \text{ } \mu\text{m}^2/\text{s}$. This suggested a stronger interaction of the positively charged TAT peptide with anionic membranes.

Also, the TAT peptide trajectories were considerably shorter than those of the lipid tracers in terms of the average number of frames, in which single molecules were observed sequentially. This indicated a rapid exchange of TAT peptides with the solution phase of neutral and anionic GUVs. The binding duration of the R-TAT molecules to neutral GUVs was shorter compared to anionic GUVs. We assume that this was due to an increased binding strength of the cationic TAT to the anionic GUVs in comparison to the neutral ones, which was already observed in the confocal microscope. Figure 3.9 shows the histograms quantifying the trajectory length of R-TAT molecules on neutral and anionic GUVs. The track length distributions showed a rapid decrease, which was approximately exponential. By fitting mono-exponential decay functions to these binding time distributions, we determined in the case of the neutral GUVs an average interaction duration of 13 milliseconds and 20 ms in case of the anionic GUVs.

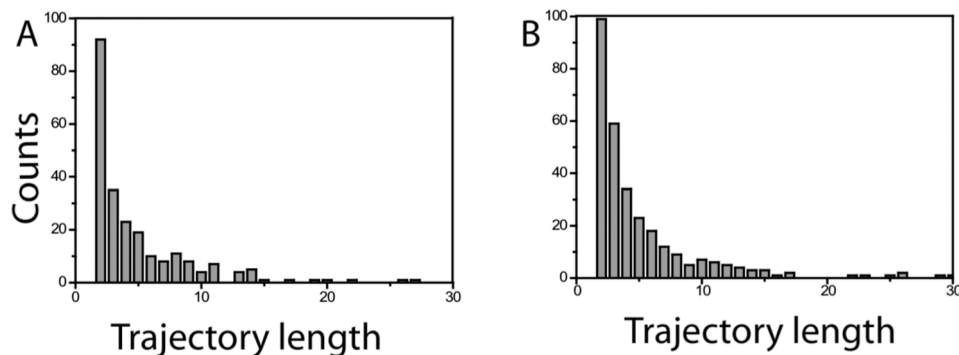


Figure 3.9: Distribution of the trajectory lengths [121] on neutral (A) and (B) anionic GUVs.

3.1.4. Lateral mobility of single TAT on the GUV surface at high concentration

The confocal experiments of R-TAT binding to GUVs revealed that at a concentration of at least 0.5 μM TAT peptides efficiently accumulate on the vesicle surface, especially in the case of anionic GUVs. In order to study the dynamics of TAT peptides within such a “peptide layer” we incubated the GUVs with 2 μM non-fluorescent B-TAT supplemented with traces of R-TAT (0.1 nM) for 30 min prior to experiments. This guaranteed that even in the presence of a high overall TAT concentration single fluorescent TAT peptides would still be sparse enough to be discerned on the GUV surface with single molecule microscopy. As above, movies revealing single TAT peptide mobility on the GUV surface were acquired and their diffusion coefficients were analysed. We found that the mobility of R-TAT peptides on the GUV surface for all examined GUV compositions could well be fitted by a single diffusion component in jump distance histograms. The analysis revealed no reduction in the mobility of R-TAT in comparison to the low concentration situation (see Table 3.4), so the possibility of peptide aggregates could be excluded. Also, there was a difference between diffusion coefficients of neutral and anionic GUVs as in previous case with low concentration of TAT peptides.

3.1.5. Monte Carlo simulations

The Monte Carlo simulations were performed according to the model presented in chapter 2.9. In neutral membranes, theoretical calculations showed that TAT peptides are located at distances higher than 20 Å from the midplane so, according to model, on membrane surface or next to it (Figure 3.10 (A)). In anionic GUVs the peptides are partially inserted in the headgroup of lipids, being located at 15 Å from the midplane (Figure 3.10 (B)). Also the hydrophobicity (p) is increased for anionic membranes compared to neutral ones, so the probability for peptides to be in the vicinity of hydrophobic core is higher.

3. Results and discussion

Simulations suggested that the peptide does not translocate the bilayer neither in neutral nor in anionic model membranes.

Thus, the theoretical simulations were in a good agreement with the experimental results. These showed a stronger interaction of TAT peptide with anionic membranes, reflected by a reduced value for diffusion coefficients comparing to neutral GUVs. Also there was detected any translocation of the peptide.

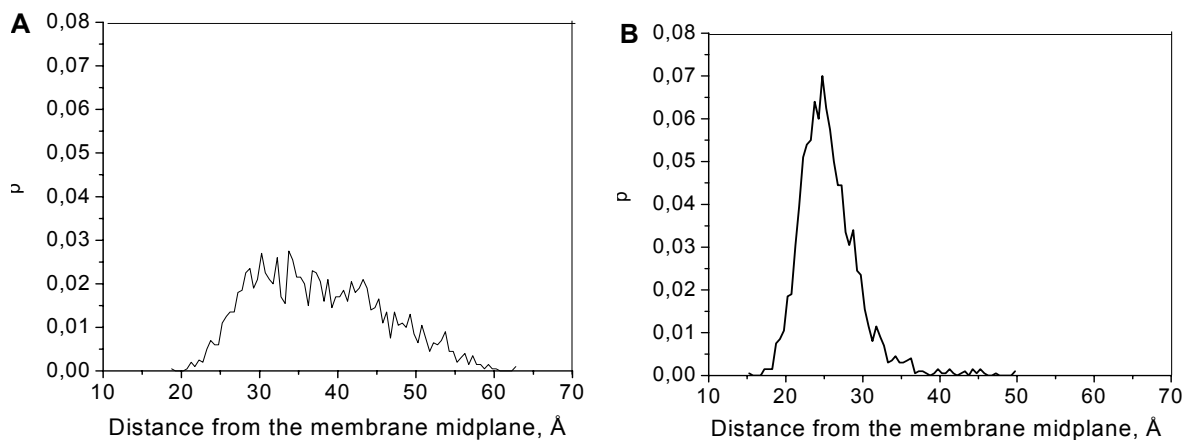


Figure 3.10: Distance distribution of TAT peptide from the membrane midplane. Hydrophobicity is denoted as p. (A) The membrane is neutral; (B) The membrane contains 15% anionic lipids.

3.1.6. Discussion

The diffusion coefficients of a lipid tracer molecule, TR-DHPE, within GUV membranes made from lipid mixtures known to form liquid-ordered, liquid-disordered membranes were measured. This part of the study provided us with reference mobility values for lipids within the employed model membranes. We found that the mobility of TR-DHPE varied from 0.5 to 2.5 $\mu\text{m}^2/\text{s}$ for liquid-ordered and liquid-disordered membranes respectively. Furthermore, the addition of 15 mol % anionic lipids did not change the tracer mobility considerably. Similar as in experiments using FCS, we detected two different diffusion

3. Results and discussion

coefficients when systems of lipids were employed, which are known to exhibit micrometer-sized domains of different composition and mobility [101].

We observed a strong and fast labelling of the GUV surface, depending on peptide concentration, which was more efficient for anionic GUVs compared to neutral GUVs. The binding did not show any lipid domain correspondence. GUVs were labelled within minutes, but no TAT was detected within the GUV interior.

The mobility of TAT peptides on the vesicle surface was significantly higher than that of the membrane-immersed tracer molecules and independent on the hydrophobic phase of the model bilayer. In contrast to the lipid mobility the diffusion of the cationic TAT peptides was clearly slowed down in membranes containing 15 mol % anionic lipids. Altogether, these observations suggested that the TAT peptides were not immersed within the viscous hydrophobic domain of the membrane, but were rather “floating” on the head-group domain of the bilayer. In the presence of anionic lipids in the membrane, the cationic TAT peptides are attracted by the negatively charged lipid head-groups causing prolonged attachments and a reduced mobility of peptides in comparison to neutral membranes. The latter observation suggested a deeper insertion of the cationic peptide into the anionic lipid head group region. The “floating” of peptides on neutral membranes and the slightly immersion in the anionic bilayers were confirmed by Monte Carlo simulations. Theoretical calculations localized the peptides at 20 Å in neutral membranes and at 15 Å in anionic membranes from the midplane, so in the lipid headgroup. Quantitative studies of TAT-mediated cell translocation of cargo molecules suggested the existence of a limiting concentration, at which effective penetration would occur [29]. We also detected a strong concentration-dependent tendency of the TAT peptides to accumulate on the model bilayers. Therefore we studied the peptide mobility also at a concentration, at which extensive TAT-membrane association would lead in cells to peptide uptake ($\sim 2 \mu\text{M}$). However, we found no significant change in TAT mobility even in this situation. One should mention that no glycosaminoglycans were present in the GUV membranes, which were suggested to play an important role in mediating interactions between TAT and cell membranes ([14], [15]), but still a strong binding, probably due to charge interaction, was obvious.

3.2. Interaction of TAT peptides with high content of anionic lipid PS

In previous experiments, we observed that electrostatic interactions plays an important role in interaction of TAT with model membranes and probably also in the penetration process. Therefore, we studied the peptide binding to vesicles prepared from anionic and zwitterionic lipids as function of surface charge density. Anionic GUVs were prepared from mixtures of DOPC/DOPS/cholesterol or DPPC/DPPS/cholesterol with a gradually increased content of PS in order to follow the effect of the anionic charge on TAT mobility and possibly translocation.

3.2.1. Neutral membranes with 20 mol % cholesterol

The literature contains numerous studies about influence of cholesterol on membrane dynamics or domain distributions. It still seems that between 20 and 33 mol % cholesterol there are no major changes in dynamics of model membranes [102]. Therefore, in the next experiments the amount of cholesterol was always 20 mol % for a more comprehensible expose of the results. The experiments of lipid mobility in GUVs with 20 mol % chol, this time were repeated to have a reference for membrane dynamics also at this content of cholesterol. GUVs with liquid-ordered phase formed by DPPC and cholesterol or liquid-disordered formed by DOPC and cholesterol were prepared for these experiments. The exact lipid mixtures were summarized in Table 3.6 in 3.2.2.2. The mobility of the tracer molecules within the model bilayers was evaluated by a jump distance analysis according to eq. 2. As expected the distributions could well be described by eq. 2 with a single diffusive species only, and yielded a diffusion coefficient of $D = 2.20 \pm 0.02 \mu\text{m}^2/\text{s}$ for DOPC compared to GUVs comprising DPPC with $D = 0.56 \pm 0.02 \mu\text{m}^2/\text{s}$ (Figure 3.11).

3. Results and discussion

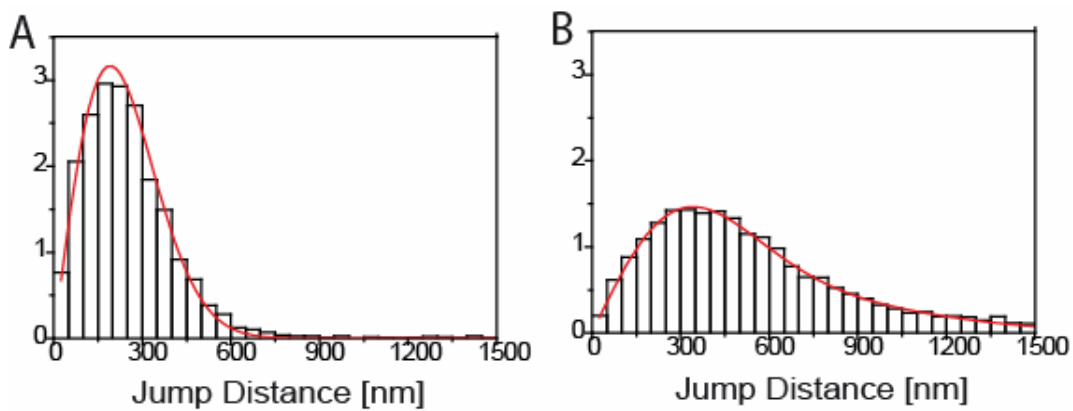


Figure 3.11: Interaction of TAT peptides with neutral model membranes containing PC. Jump distance analysis for TR-DHPE in neutral GUVs: DPPC (A) or DOPC (B). TR-DHPE moves more rapidly within GUVs known to have an unordered phase with a diffusion coefficient D of $2.20 \pm 0.02 \mu\text{m}^2/\text{s}$ compared to GUVs known to comprise an ordered phase ($D = 0.56 \pm 0.01 \mu\text{m}^2/\text{s}$).

3.2.1.1. CLSM imaging of TAT peptide-membrane interaction using neutral GUVs

As previous, to examine the TAT peptide interaction with the model membranes, we incubated the GUVs with R-TAT or AF-TAT contained in glucose solution. Interaction of TAT peptides with neutral GUVs was monitored as a function of time by confocal laser scanning microscopy (Figure 3.12). Over a time period of 30 min the fluorescence at the GUV surface increased upon incubation with 2 μM of R-TAT, but no fluorescence was detected inside of the GUVs. Even in a special case, where a GUV contained several internal membranes, connected to the outer membrane as could be seen in the DIC image, no labelling of the inner membranes was observed (see arrow in Figure 3.12, DIC image at 30 min). The peptides were not able to translocate across the membrane at TAT peptide concentrations up to 2 μM under the given experimental conditions. Similar results were obtained also for AF-TAT.

3. Results and discussion

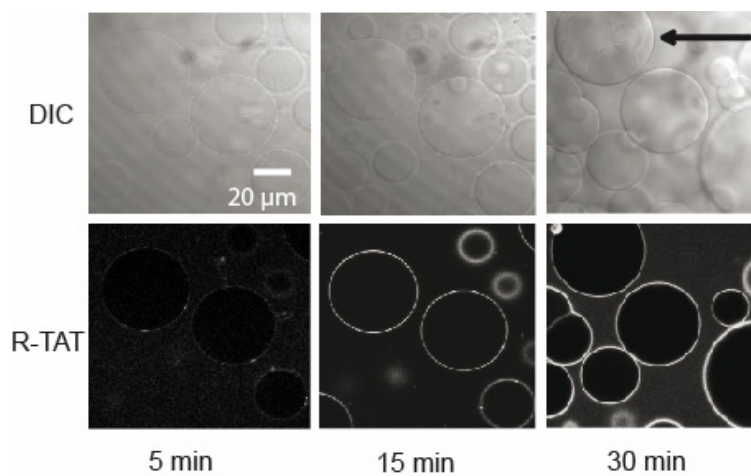


Figure 3.12: Confocal imaging of TAT peptide-membrane interaction with neutral GUVs in glucose solution. The upper panel shows the time series of DIC images of the GUVs and the lower panel illustrates the confocal fluorescence images of the GUVs incubated with 2 μ M R-TAT in the rhodamine fluorescence channel. R-TAT does not translocate, but just accumulates on the GUV membranes. The arrow indicates a GUV containing several internal membranes, which appeared connected to the outer membrane. The inner vesicles were not labelled by the peptide indicating that there was no internalization of TAT.

3.2.1.2. Lateral mobility of single TAT on neutral GUVs surfaces

The model neutral GUVs were incubated with 0.25 nM AF-TAT for 30 min in order to study the mobility of TAT peptides at membrane surface. A respective jump distance analysis clearly demonstrated a significantly higher mobility of AF-TAT compared to membrane-embedded tracer molecules (Table 3.5). The mobility of the AF-TAT peptide on the GUV surface was virtually identical for DOPC- and DPPC-based GUVs within the precision of the measurements. All jump distance histograms could well be fitted using a single diffusion component. The mobility on the neutral GUV surfaces was $D_{TAT} = 5.3 \pm 0.3 \text{ } \mu\text{m}^2/\text{s}$ for GUVs prepared from DPPC/cholesterol and $D_{TAT} = 5.2 \pm 0.1 \text{ } \mu\text{m}^2/\text{s}$ for DOPC/cholesterol containing GUVs. This confirmed the previous results from 3.1., that TAT peptide motion was independent of the internal lipid bilayer structure.

3. Results and discussion

Table 3.5: AF-TAT mobility on GUVs

Sample (Cholesterol 20 mol %)	DPPC	DOPC	DOPC /DPPS = 80-x /x		
			X = 20	X = 30	X = 40
D _{1,SPT} [$\mu\text{m}^2/\text{s}$]	5.3±0.3	5.2±0.1	4.0±0.1	3.9±0.2	4.1±0.2

3.2.2. Interaction of TAT peptides with anionic model membranes

Anionic GUVs were prepared from mixtures of DOPC/DOPS/cholesterol or DPPC/DPPS/cholesterol with a gradually increasing PS content from 20 to 40 mol %, in order to follow the effect of the anionic charge on TAT peptide mobility and possibly translocation.

3.2.2.1. Imaging and tracking of single lipid analogs within anionic GUVs

Following the analysis of lipid tracer mobility in neutral GUVs similar measurements were performed for anionic GUVs containing 40 mol % PS and 20 mol % cholesterol. The lipid tracer TR-DHPE was imaged within anionic liquid-ordered and liquid-disordered GUVs containing DPPC/DPPS and DOPC/DOPS, respectively. As previous, the mobility of the tracer molecules within the bilayers was quantified by a jump distance analysis. The histogram data could well be fitted by a single diffusion component (Figure 3.13). Similar to neutral membranes, TR-DHPE moved more rapidly within GUVs with a liquid-disordered phase with a diffusion coefficient D of 2.01±0.01 $\mu\text{m}^2/\text{s}$ compared to GUVs

3. Results and discussion

with liquid-ordered phase, $D=0.54\pm0.01 \mu\text{m}^2/\text{s}$. The presence of the charged lipid in a high percent did neither change the phase behaviour nor the lipid tracer mobility considerably.

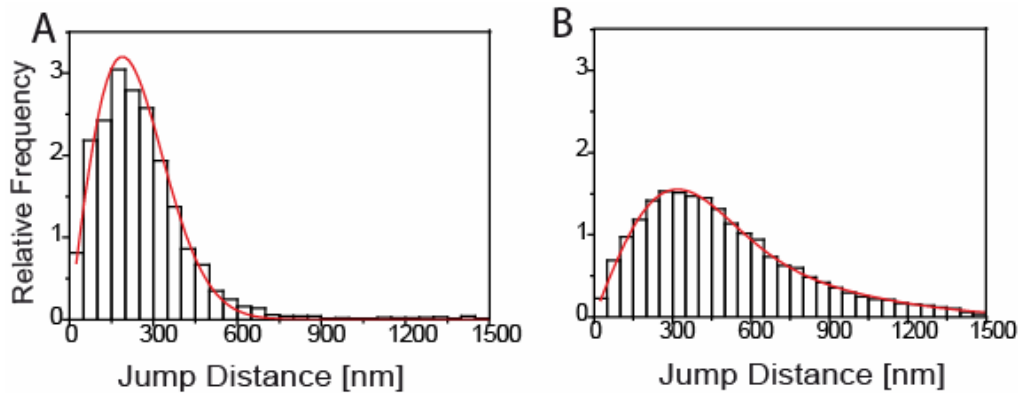


Figure 3.13: Mobility of lipid tracers in anionic model membranes

Jump distance analysis for TR-DHPE in anionic GUVs: (A) DPPC/DPPS and (B) DOPC/DOPS. The anionic charge was 40 mol %.

3.2.2.2. CLSM imaging of TAT peptide-membrane interaction using anionic GUVs

CLSM experiments were performed in DOPC/DOPS/cholesterol or DPPC/DPPS/cholesterol lipid mixtures containing 20, 30 and 40 mol % of PS (Table 3.6 for membrane composition). An increase over 40 mol % of PS resulted in the failure of GUVs formation by electroswelling. Anionic GUVs were incubated with 2 μM AF-TAT containing glucose solution. A distinct labelling of the GUVs was already visible after 5 min for 20% PS and 2 min for 30% and 40% PS. The labelling of the anionic GUVs was significantly stronger than that of neutral GUVs at the same microscope settings. At 40 mol % PS TAT peptide fluorescence was observed within GUVs indicating peptide translocation across the bilayer (Figure 3.14).

3. Results and discussion

Table 3.6: Composition of giant unilamellar vesicles (GUVs).

GUWs (Cholesterol 20 mol %)	Lipids, mol %			
	Saturated		Unsaturated	
	DPPC	DPPS	DOPC	DOPS
neutral	80	-	80	-
anionic	60	20	60	20
	50	30	50	30
	40	40	40	40

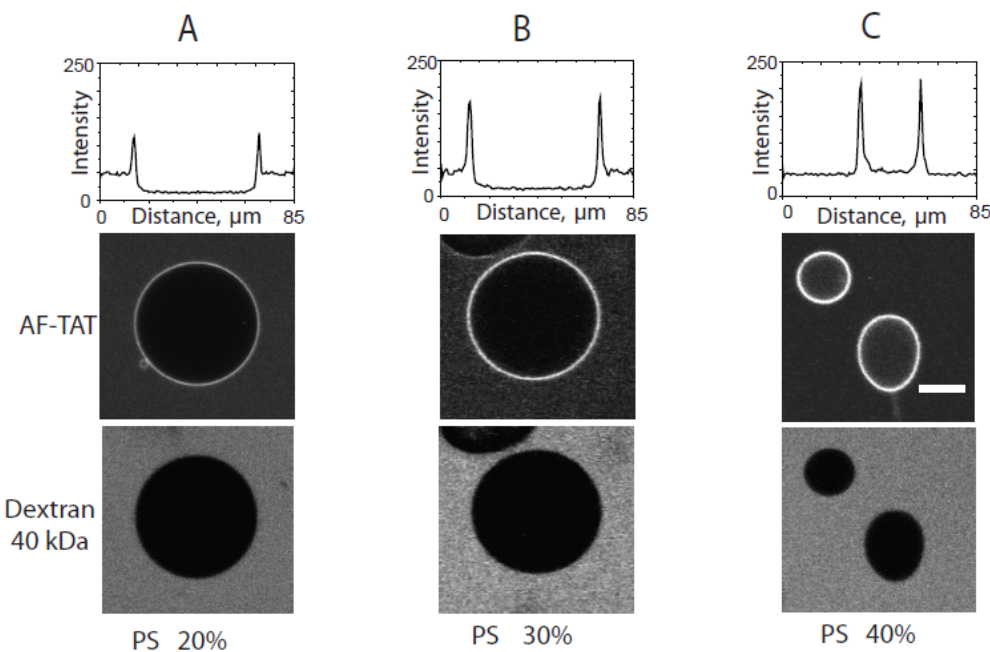


Figure 3.14: Interaction of TAT peptides with anionic model membranes [122] Confocal imaging of TAT peptide labelled with Alexa Fluor 647 interacting with anionic GUVs: (A) membranes with 20 mol % PS, (B) membranes with 30 mol % PS, and (C) membranes containing 40 mol % PS. The upper plots quantify the intensity of fluorescent TAT peptides along a line across the GUVs shown in the images in the central image panel. The internalization of TAT peptide can clearly be seen in (C). All experiments were done in the presence of 40 kDa dextran labelled with fluorescein (lower panel). Time of observation was 30 minutes. Scale bar, 20 μ m.

In order to control the overall membrane integrity, this experiment was performed in the presence of a 40 kDa fluorescein-labelled dextran, which was imaged in a separate

3. Results and discussion

fluorescence channel (Figure 3.14, lower panel). This dextran has a Stokes radius of 4.3 nm [123]; [124] and remained completely excluded from the GUVs at AF-TAT concentrations of 2 μ M. After 20 to 30 min a few vesicles with 40% PS began to deform, break and release their inner content (see Figure 3.14 (C), the lower GUV and Figure 3.15).

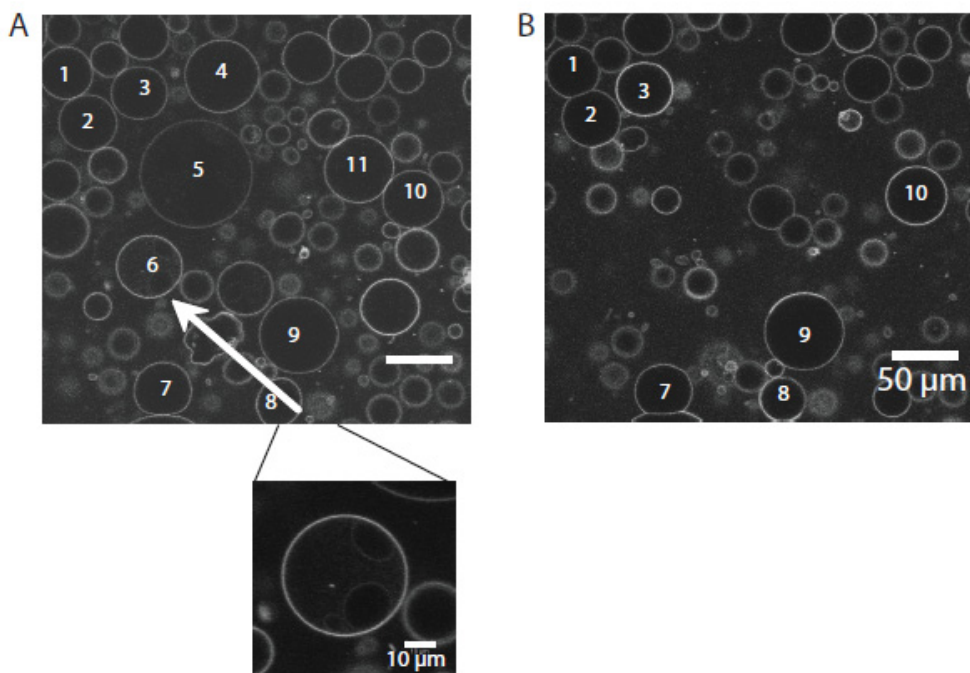


Figure 3.15: Confocal images of GUVs with 40 mol % PS in presence of 2 μ M AF-TAT (A) after 20 min of incubation with the TAT peptide. There was a special case where the TAT import could be well observed in a GUV containing two internal membranes; (B) after 30 min a several GUVs already disappeared.

The CLSM images suggested an increasing interaction of the positively charged peptides with the increasing surface charges in anionic bilayers. Thus, we examined whether amount of anionic charge would have an impact on the TAT mobility on the GUV surface. For SPT experiments, the GUVs comprising 20, 30 and 40 mol % PS were incubated with 0.25 nM AF-TAT for 30 minutes. In all cases the diffusion coefficient was $D=4.0\pm0.2$ μ m²/s without a detectable mobility difference in the absence or presence of translocation (Figure 3.16 (A-C)). A difference, however, was observed for TAT peptide mobility on neutral versus anionic GUVs (Table 3.5). The mobility of TAT on the neutral GUV

3. Results and discussion

surfaces was faster than on the anionic GUVs. The average diffusion coefficient on the neutral GUVs was $D_{SPT}=5.3\pm0.2 \mu\text{m}^2/\text{s}$, whereas it amounted only to $D_{SPT}=4.0\pm0.2 \mu\text{m}^2/\text{s}$ on anionic GUVs indicating an increased binding strength of the cationic peptides to the anionic GUVs.

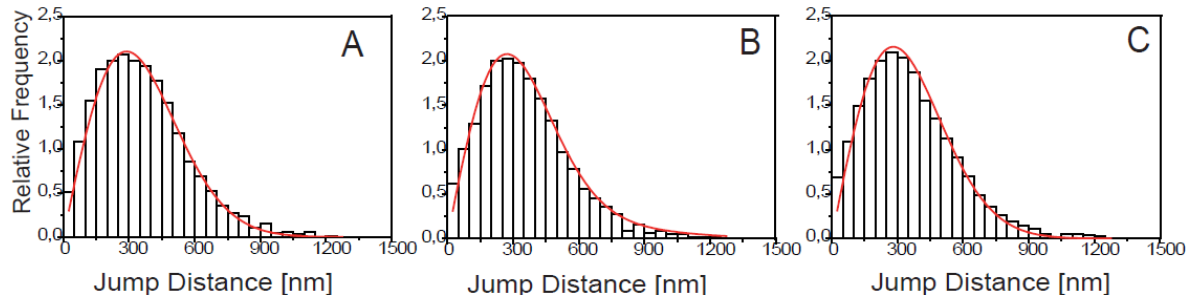


Figure 3.16: The histograms show the analysis of AF-TAT diffusion on anionic GUVs with (A) 20 % PS, (B) 30 %PS, and (C) 40 % PS. [122]

To gain deeper insight into the membrane translocation of TAT peptide in GUVs with 40 mol % PS and to test the hypothesis of a pore formation, we incorporated different water soluble fluorescent tracer molecules with increasing molecular weight (Alexa647-maleimide 1.3 kDa, Alexa546-dextran 3 kDa, Alexa546-dextran 70 kDa) inside the GUVs [125]. If there is any lytic effect induced by the peptide, an efflux of the dyes should be observed by confocal microscope. After peptide addition the tracer fluorescence inside the GUVs was followed as a function of time (Figure 3.17 and 3.18).

Indeed, these experiments revealed the complete release of Alexa647 within 20 minutes. For a few GUVs the break of the membrane was observed in a similar way to the experiments without internal tracers (Figure 3.17(A)). For the 3 kDa dextran, an efflux of 50% from the tracer was observed. In contrast, the 70 kDa dextran molecules remained included in the GUVs. Figure 3.18 shows plots corresponding to internalization of TAT peptide (A) and efflux of tracers (B) in GUV with 40 mol % PS. The measured fluorescence intensity values representing the AF-TAT were normalized to the outside intensity. In Figure 3.18(B) is shown normalized fluorescence intensity for the leakage of tracers loaded inside of GUVs: AF647 maleimide, Alexa546-dextran 3 kDa and Alexa546-dextran 70 kDa.

3. Results and discussion

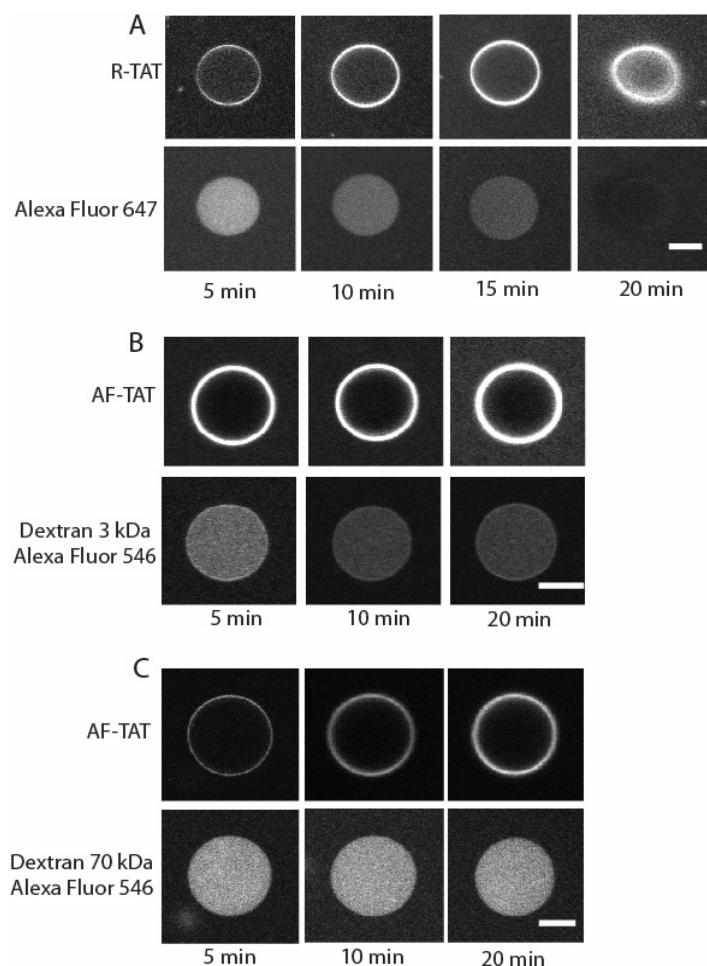


Figure 3.17: Pore formation by TAT peptides in GUVs containing 40 mol% PS.

(A) The upper panel shows the binding and translocation of 2 μ M R-TAT, and the lower panel the leakage of Alexa Fluor 647, and final GUV disruption.

(B) Upper panel, binding and translocation of AF-TAT peptide, lower panel shows the partial release of 3 kDa dextran labelled with Alexa Fluor 546.

(C) Upper panel, AF-TAT, lower panel 70 kDa dextran labelled with Alexa Fluor 546. This large dextran remained included within the GUVs. Scale bar, 20 μ m. [122]

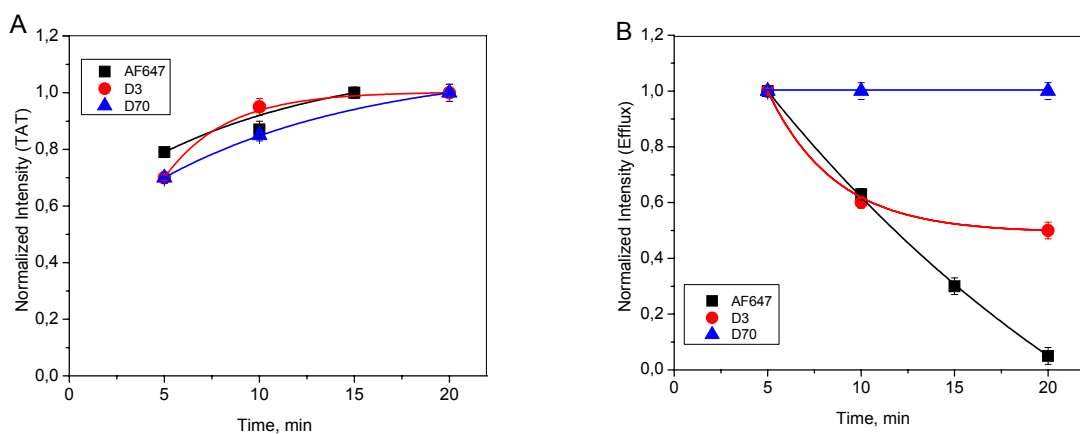


Figure 3.18: Internalization of TAT peptide (A) and efflux of tracers (B) in GUV with 40 mol % PS as presented in Figure 3.18. The solid line represents the exponential fit.

3. Results and discussion

In absence of any TAT, the GUVs were stable even after 24 h, and no fluorescent content was released. To verify that the observed fluorescence decay was not due to photobleaching of the tracers we performed control experiments in similar conditions but without peptides. There was no change in fluorescence intensity for a similar number of images in these experiments (see Figure 3.19). So, we concluded that the previous release of the tracer molecules from the vesicles was due to TAT peptide induced pores in the GUV membranes.

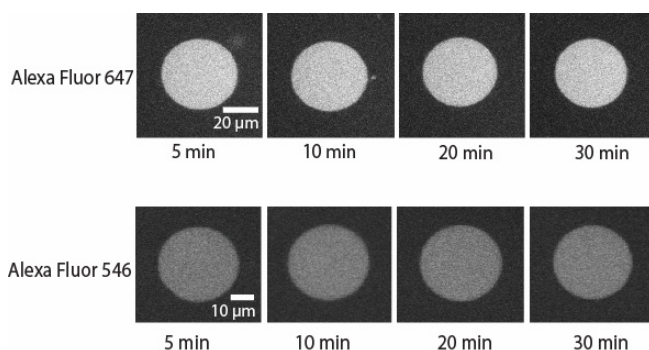


Figure 3.19: Control experiments for Alexa Fluor 647 and Alexa Fluor 546 photobleaching

The images show GUVs loaded with fluorescent markers in the absence of the TAT peptide. The fluorophores were stable; there was no change in fluorescence intensity even after repetitive imaging scans.

3.2.3. Monte Carlo simulations

The Monte Carlo simulations for interaction of TAT peptide with PS membranes were performed for different mol % of anionic lipids, up to 100, according to the model presented in 2.9. The simulations suggested that the probability of peptide to insert in the hydrophobic core of the lipid membrane increases with the content of anionic charge (Figures 3.20 and 3.21). In Figure 3.20 is shown that at 15 mol % PS the peptide is localised in the headgroup region (after 15 Å from the membrane midplane). Over 30 % anionic charge the peptide hydrophobicity (p) increased, meaning that the peptide is situated at the border or inside of hydrophobic core of bilayer.

3. Results and discussion

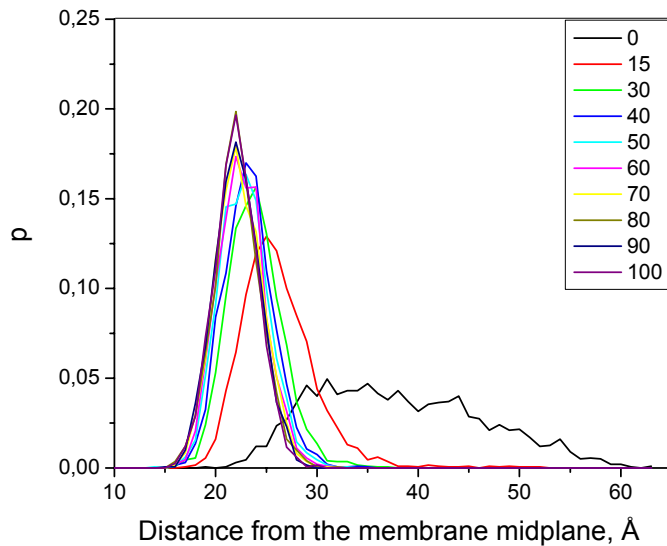


Figure 3.20: The distance distribution of TAT in a membrane containing anionic lipids (0, 15, 30, 40, 50, 60, 70, 80, 90, 100 mol % PS).

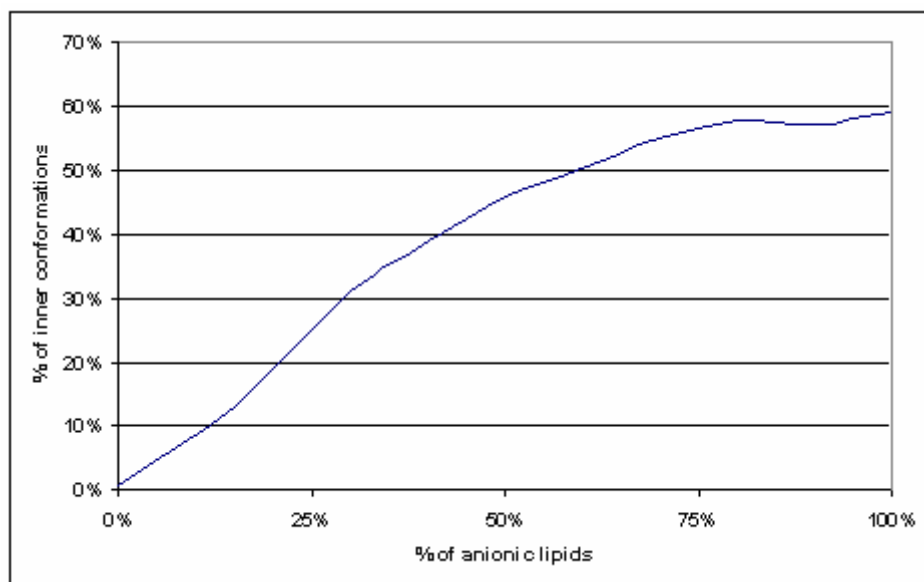


Figure 3.21: Inner conformations versus ratio of anionic lipids. Inner conformations are considered at least adsorbed to the membrane.

Figure 3.21 shows the plot of inner conformation against the content of PS. Inner conformation implies that the peptide is at least adsorbed on the membrane. At anionic content of 40%, the probability of the peptide to be inserted in the hydrophobic core is

3. Results and discussion

almost 50%, so the possibility of translocation is highly increased compared to neutral or containing 15 mol % PS membranes. In conclusion, if the amount of anionic charge is high enough, this could be a sufficient condition to favour the translocation. Interestingly, even for pure anionic membranes the translocation was not 100 %, maximum being 60 %. For the theoretical model of the membrane see Figure 2.7.

3.2.4. Discussion

The experiments from chapter 3.1 revealed stronger interactions of TAT peptide with membrane containing anionic lipids comparing to neutral ones. Therefore the content of PS from GUVs composition was gradually increased up to 40 mol %.

Again, to have a reference for peptides mobility, the diffusion of the lipid tracer molecule TR-DHPE, within the membranes of GUVs made from lipid mixtures based on PC and PS was analysed by high-speed and high-sensitivity single molecule tracking. We found that the mobility of the tracer in membranes containing 40 mol % PS is 0.54 ± 0.01 and $2.01\pm0.01 \mu\text{m}^2/\text{s}$ for liquid-ordered and liquid-disordered phases, respectively. The diffusion coefficients did not differ in anionic membranes containing up to 40 mol % PS comparing to neutral ones for the same hydrophobic chains confirming that the anionic charge of the headgroup does not significantly modify lipid mobility.

To analyse the general features of TAT peptide interaction with the chosen model membrane systems the GUVs were incubated with red-fluorescent TAT peptides in glucose solution, in presence of 40 kDa green-fluorescent dextran molecules for checking overall integrity of the vesicles. TAT peptides were not able to traverse the membrane at concentrations up to 2 μM in GUVs with 20-30 mol % PS since no fluorescence was detected within the vesicles. In this case, imaging of single TAT peptide molecules on the surface of the GUVs revealed that the peptide mobility was significantly higher than that of the lipids and not depending on the lipid phase confirming previous results from chapter 3.1 that TAT peptides are not inserted but rather floating on the membrane. But, when the molar ratio of the anionic lipid PS in the model membrane was increased to 40 mole % TAT peptides were observed inside of GUVs. Also, in some cases, the vesicles

3. Results and discussion

became so unstable that they broke and released their content. Simultaneously, the mobility of the peptides was measured by SPT. Even at the highest anionic charge concentration examined –with ongoing peptide translocation– a further reduction of TAT mobility compared with 20 or 30 mol % PS was not observed.

It has been suggested by computer simulations that TAT peptides may form pores within membranes [18], [20]. If TAT peptides can induce pores into GUV membranes, then small molecules should be able to flow across the membranes. To test this possibility, we performed efflux experiments with small fluorescent molecules. Indeed, GUVs comprising 40% PS in their membrane and containing the dye Alexa 647 released these 1.3 kDa tracer molecules within 20 minutes after peptide addition. Approximately 50% of the fluorescent 3 kDa dextran tracer was released from GUVs within 30 minutes of incubation with 2 μ M TAT. In contrast to these small molecules, 70 kDa dextran molecules remained within the GUVs. These observations suggested that the induced pores are small, up to 2 nm in diameter. Based on single molecule and confocal results we concluded that the TAT peptides first accumulate and associate to the membrane due to the electrostatic interactions. At a certain concentration pores were formed, which allowed peptides and tracers to pass. The life time of the pores must be extremely short, because they were not observable by single molecule tracking. These results for TAT peptides confirmed recent data obtained by Herce et al. for another CPP and TAT peptide too [20]. They demonstrated the flow of ions across and thus the presence of pores within a black lipid membrane system in the presence of nona-arginine and TAT peptide. Also, the theoretical simulations showed a good agreement with our experimental observations. The calculations suggested a deeper insertion of TAT in the hydrophobic core while the content of anionic lipids is increased, pointing to the possibility of peptide translocation.

3.3. Interaction of TAT peptides with model membranes containing lipids inducing a negative curvature (PE)

PE contains a primary amine group and PC a choline group. This leads to a small headgroup and a negative intrinsic curvature for PE unlike to the zero intrinsic curvature of "cylinder-shaped" PC. Also PS has a "cylindrical shape" with zero intrinsic curvature. PE is often found concentrated in the inner leaflet of membranes and plays an important role in the membrane fusion mechanism and vesicle formation [126]. For this reason, PE is associated with a wide variety of biological functions including cell division, growth, reproduction, and motility [127]; [128]. In bacterial membranes is the most abundant phospholipid (see Table 1.3 for composition of *E. coli*). PE has a role in bacterial growth, function of enzymes as folding of lactose permease. In most cases it acts like protein chaperones that assist the non-covalent folding or unfolding and the assembly or disassembly of other macromolecular structures, without appearing in these structures when they perform the normal biological functions [129].

Table 3.7: Composition of GUVs membrane containing PE

GUVs (Cholesterol 20 mol %)	Lipids, mol %			
	Saturated		Unsaturated	
	DPPC	DPPE	DOPC	DOPE
	70	10	70	10
	60	20	60	20
	50	30	50	30

Since the previous experiments suggested that TAT interacts with lipid head groups rather than with the hydrophobic core, we investigated if the differences between PC and PE could induce changes in peptide mobility. It was not possible to generate vesicles by

3. Results and discussion

electroformation from pure PE. Therefore, we prepared mixtures of PC/chol and PE. The prepared GUVs contained 10, 20 or 30 mol % PE and 20 mol % of cholesterol (Table 3.7).

3.3.1. Diffusion of single lipid analogs in model membranes containing PE

The analysis of lipid tracer mobility in PE containing GUVs was done in a similar way to the experiments presented in the previous chapters. We examined two different lipid compositions, with liquid-ordered and liquid-disordered phases, containing DPPC/DPPE/cholesterol and DOPC/DOPE/cholesterol respectively, both with 30 % of PE. In spite of the fact that the hydrophobic core was identical to the GUVs containing PC and PS examined previously, now we observed significantly lower diffusion coefficients, *i.e.* 0.41 ± 0.02 and $0.63 \pm 0.02 \mu\text{m}^2/\text{s}$ (Figure 3.22). Obviously, the negative curvature of the phosphoethanolamine caused a distortion of the membrane topology which diminished lipid mobility significantly, especially for unsaturated lipids.

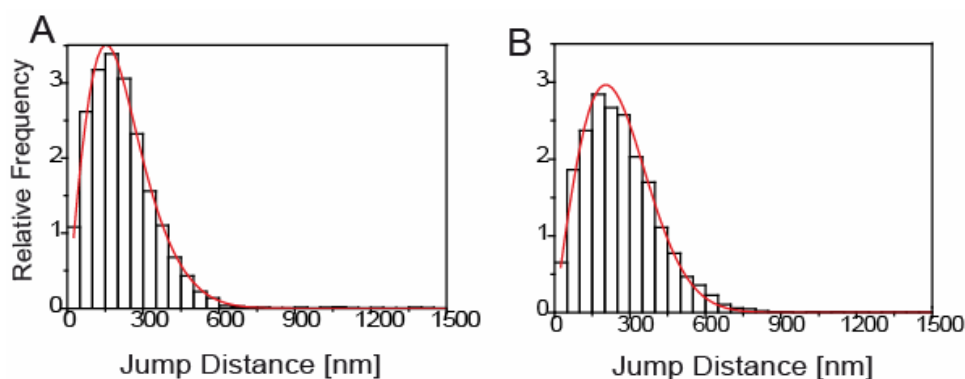


Figure 3.22: Mobility of lipid tracers on model membranes containing PE

Jump distance analysis for TR-DHPE in GUV membranes containing 30 mol % PE: (A) DPPC/DPPE/chol; (B) DOPC/DOPE/chol. The mobility of the tracer was significantly reduced in comparison to the PS and PC membranes discussed above. D found for (A) was $0.63 \pm 0.02 \mu\text{m}^2/\text{s}$ and $0.41 \pm 0.02 \mu\text{m}^2/\text{s}$ for (B)

3.3.2. CLSM imaging of TAT peptide-GUVs interaction

GUVs prepared from DOPC/DOPE/cholesterol and DPPC/DPPE/cholesterol were incubated with 2 μ M AF-TAT in presence of fluorescein-labelled 40 kDa dextran to control the overall integrity of the bilayer. GUVs with molar fractions of PE from 10 mol% to 30 mol % were examined. For 10% of PE we observed no visible peptide translocation, only accumulation on the membrane. Starting with 20 and 30% PE a clear TAT peptide translocation was observed after 30 min (Figure 3.23 A, B and C).

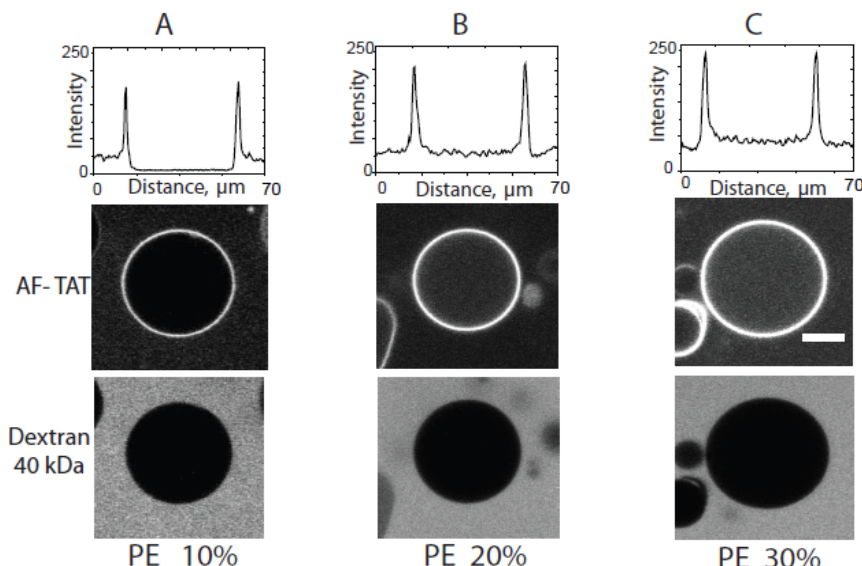


Figure 3.23: Interaction of TAT peptides with model membranes containing PE [122] Confocal imaging of AF-TAT peptide interaction with GUV membranes comprising (A) 10 mol % PE, (B) 20 mol% PE and (C) 30 mol % PE. The upper plots show the intensity of TAT peptide fluorescence along the central line of the images below. Internalization of TAT peptides can clearly be seen in (B) and (C). All experiments were done in the presence of 40 kDa FITC-dextran in the outer medium (lower panel). Observation time was 30 minutes after peptide addition. Scale bar, 20 μ m.

In the upper panel from Figure 3.23 (B and C), it appeared that the peptide reached a higher concentration within the GUV than outside, which is obviously against thermodynamic principles. Control experiments revealed that this was due to the fact that different sugars were inside and outside of the GUVs. The presence of sucrose instead of glucose in the medium results in 80% increase in fluorescence intensity of the dye (Figure

3. Results and discussion

3.24). The sugar-dependent fluorescence of dyes such as FITC or TRITC can even be used to quantify glucose concentrations [130].

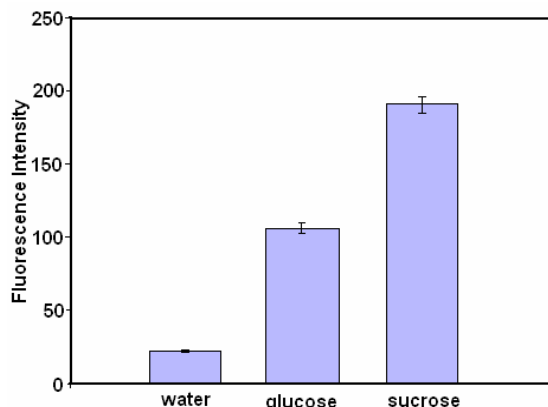


Figure 3.24: A comparison of fluorescence intensity for Alexa-Fluor 647 in water and sugars. Addition of sugars dramatically increases the fluorescence intensity of the dye at the same concentration. Also, the concentration of sugars is identical, 250 mM.

To check whether the translocation occurred due to pore formation, similar leakage experiments as in the case of GUVs containing PS were performed (Figure 3.25). The GUVs were filled up with Alexa Fluor 647 maleimide, 3 kDa and 70 kDa-dextran. After incubation with 2 μ M AF-TAT, Alexa Fluor 647 dye molecules were completely released from GUVs containing 30 mol % PE within 20 min. However, both fluorescent dextrans, 3 kDa and 70 kDa, did not pass the respective GUV membranes. With these experiments we confirmed that the presence of TAT peptide induced pores in GUVs. In addition, we found that TAT peptides induce differently sized pores in PE comparing to PS containing membranes. The fluorescent 3 kDa dextran was released from PS but not from PE comprising GUVs.

Figure 3.26 shows the plots corresponding to internalization of TAT peptide (A) and efflux of tracers incorporated inside of GUVs (B) in GUV with 30 mol % PE. The measured fluorescence intensity values representing the AF-TAT were normalized to the outside intensity. It should be mentioned here that it was difficult to quantify the amount of internalised peptide or released tracers due to difference in fluorescence intensity for glucose and sucrose.

3. Results and discussion

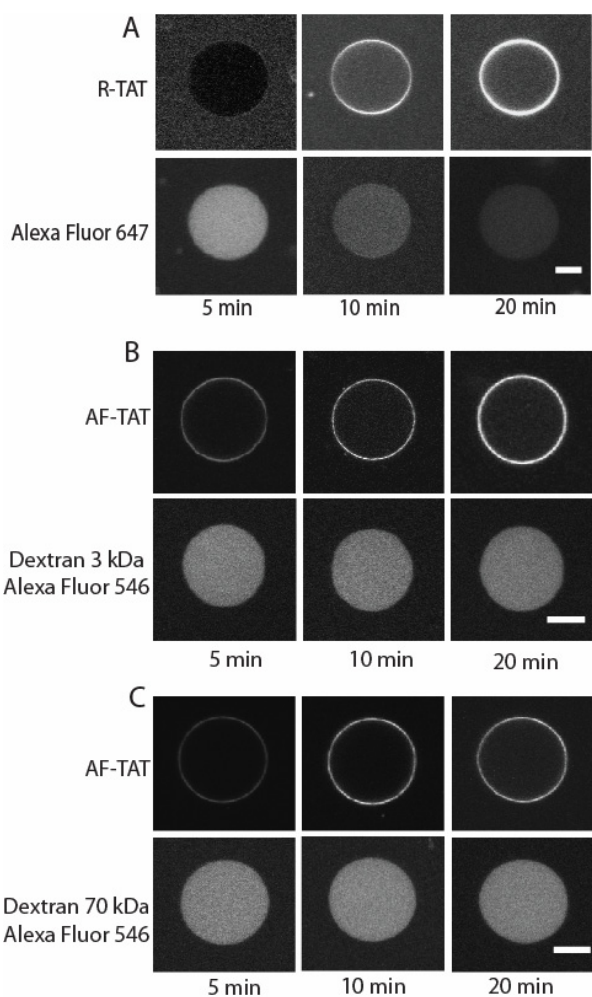


Figure 3.25: Pore formation of TAT peptides in membranes containing 30 mol % PE [122]

(A) The upper panel shows the internalization of R-TAT, and the lower panel shows the efflux of Alexa Fluor 647 from GUVs comprising 30 mol % PE.

(B) Upper panel, internalization of AF-TAT; lower panel, no efflux of Alexa Fluor 546 labelled 3 kDa dextran molecules was detected.

(C) Upper panel, internalization of AF-TAT; lower panel, no efflux of Alexa Fluor 546 labelled 70 kDa dextran molecules was detected. Scale bar, 20 μ m.

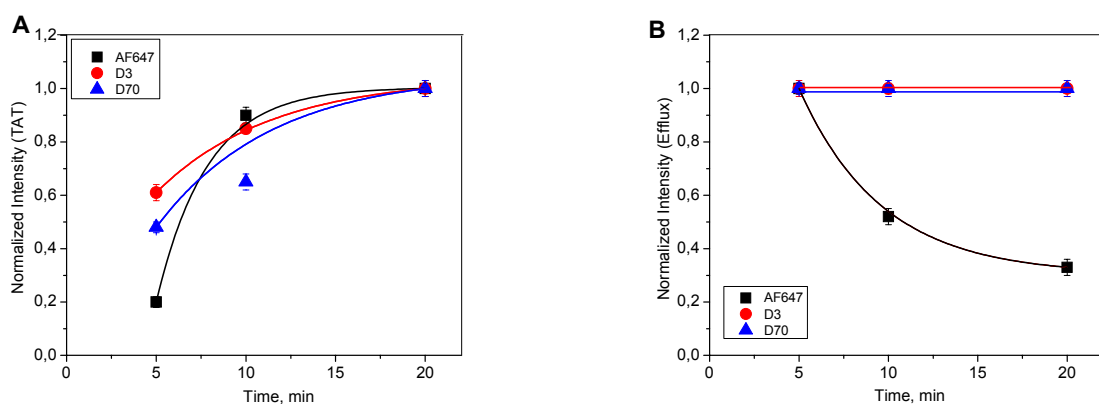


Figure 3.26: Internalization of TAT peptide (A) and efflux of tracers (B) in GUVs with 30 mol % PE as presented in Figure 3.25. The solid line represents the exponential fit.

3.3.3. Lateral mobility of single TAT on the GUVs surface

To determine the mobility of peptides, SPT experiments were performed on GUVs containing 10, 20 or 30 mol % PE after an incubation with 0.25 nM AF-TAT in glucose for 30 minutes. Single AF-TAT trajectories were recorded, and the mobility characteristics were quantified by means of jump distance histograms (Figure 3.27 A, B and C). For 10 % PE, where no peptide translocation occurred, the mobility was similar to that on neutral GUVs, suggesting alike to this case, that the peptide was not incorporated into but floating on the membrane. Instead, for 20 % PE molar ratios, where a distinct TAT translocation was observed by confocal microscopy, the jump distance histogram was clearly bi-modal, and two diffusion coefficients were required for a satisfactory fit of the data. The higher coefficient, $D_1 = 5.2 \pm 0.1 \mu\text{m}^2/\text{s}$, was similar to the values determined for TAT peptides moving on the GUVs surface. Interestingly, the second coefficient, $D_2 = 0.3 \pm 0.1 \mu\text{m}^2/\text{s}$, was even lower than the lipid mobility (Table 3.8). For GUVs with 30 % PE, the diffusion coefficients were even more reduced. The histogram for 10 mol % PE showed a very small fraction for a second component with a reduced mobility (Figure 3.27 (A)). Therefore the jump distance histogram was fitted with two diffusion coefficients. To reduce fitting parameter correlation, for the second fit, the diffusion value was fixed to 0.3 and the found fraction was only 4 %.

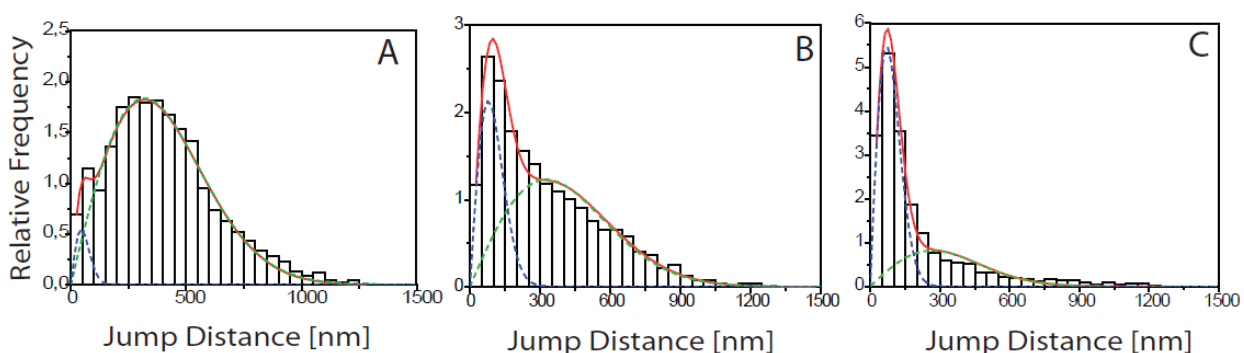


Figure 3.27: Interaction of TAT peptides with model membranes containing PE.

The histograms show the analysis of AF-TAT diffusion on the respective GUVs with (A) 10 % PE, (B) 20 %PE, and (C) 30 % PS. Scale bar, 10 μm . [122]

3. Results and discussion

Table 3.8: AF-TAT peptide mobility on PE containing GUVs (DOPC /DPPE =80-x /x)

Sample (Cholesterol 20 mol %)	D _{1,SPT} [μm ² /s]	Fraction 1	D _{2,SPT} [μm ² /s]	Fraction 2
X = 10	5.2±0.1	0.96	*0.3	0.04
X = 20	5.3±0.2	0.67	0.4±0.1	0.33
X = 30	3.6±0.6	0.36	0.3±0.1	0.64

* For this fit, the diffusion value was fixed to 0.3 to reduce fitting parameter correlation

The presence of two distinct diffusion coefficients indicated that TAT peptides first attach to the membrane in relatively loose manner as in the other cases, probably due to the partially negative charge of PE. Then they could form some large molecular aggregates on or within the membranes, which comprise several lipid molecules.

Therefore, a step forward to verify the possibility of aggregates formation would be to monitor the effect of TAT on the bilayer and to analyse the dynamic of lipids in the presence of 2 μM unlabelled peptide. So, we performed experiments with both saturated and unsaturated lipid chains in membranes containing 30 mol % PE labelled with the tracer TR-DHPE in glucose solution were 2 μM B-TAT were added. Surprisingly, the mobility of the lipids in PE membranes was not changed in presence of TAT, the diffusion coefficients being D=0.67 μm²/s for DOPC/DOPE/chol and D=0.44 μm²/s for DPPC/DPPE/chol (see Figure 3.28 for jump distance histograms).

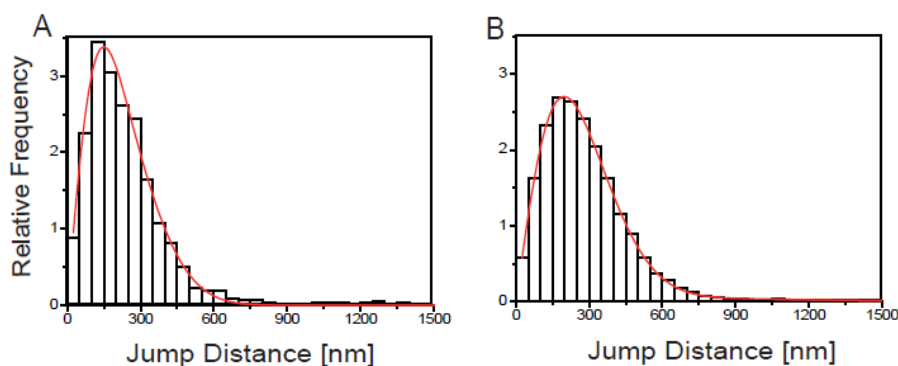


Figure 3.28: Interaction of B-TAT peptides with model membranes containing 30 mol % PE labelled with TR-DHPE. The histograms show the analysis of TR-DHPE diffusion in the respective GUVs comprising (A) DPPC/DPPE/chol and (B) DOPC/DOPE/chol.

3. Results and discussion

A second component corresponding to aggregates mobility was not identified. So, the hydrophobic core of the membrane seems not to be affected by the TAT.

Since the lower diffusion coefficient is not a consequence of lipids aggregates, then it should reflect the peptide mobility. Analysing the trajectories for TAT in GUVs with different mol % PE, these are comparable with those of the tracer lipids in 10 % PE membranes. Instead, for 20 and 30 mol %, the trajectories are shorter and more confined (Figure 3.29). We can conclude that the mobility of TAT peptide is slowed down in GUVs with higher content of PE and the second diffusion coefficient represents TAT mobility.

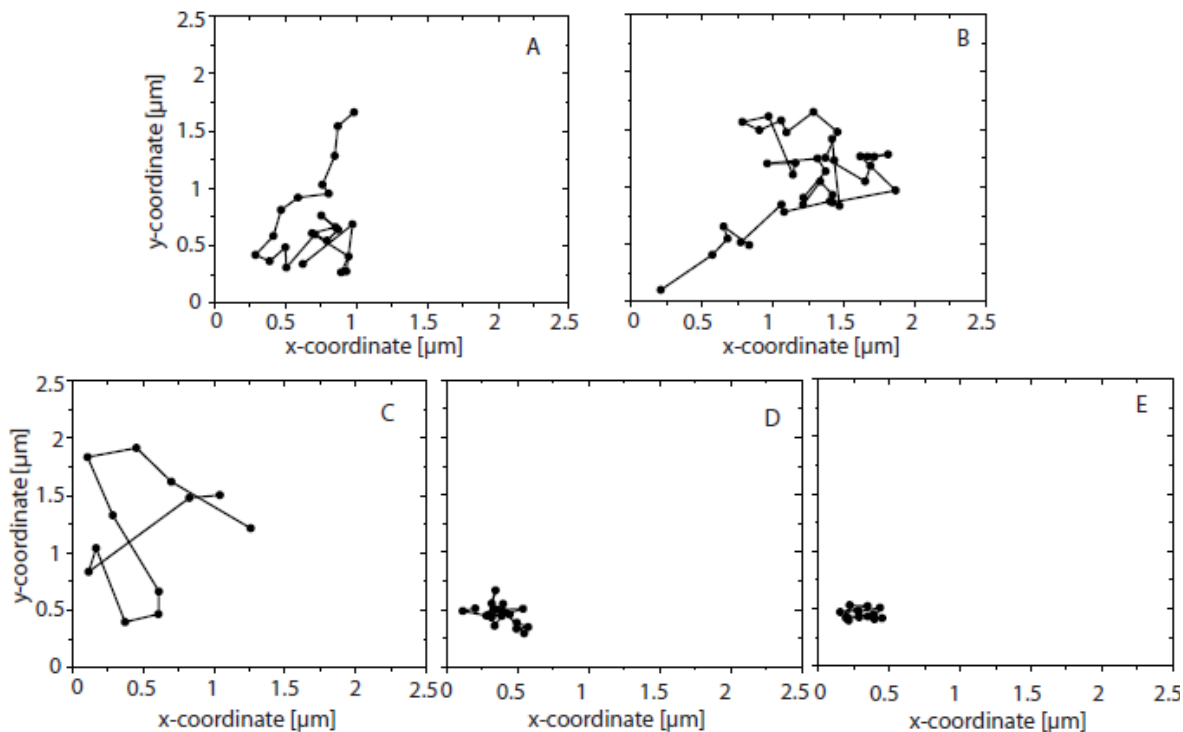


Figure 3.29: Plots of two-dimensional diffusion trajectory of the tracer **TR-DHPE** in saturated membranes containing PE (A), unsaturated GUVs with PE (B) and the trajectories for **AF-TAT** peptide in membranes containing 10 mol % PE (C), 20 mol % PE (D) and 30 mol % PE (E)

3.3.4. Discussion

To have a reference for peptide diffusion, the mobility of the lipid tracer molecule TR-DHPE, within the membranes of GUVs made from lipid mixtures based on PC and PE was analysed by single molecule tracking. We found that in membranes containing PE and PC the tracer molecules had lower diffusion coefficients compared to PC or PC/PS mixtures, although the used lipids contained the same hydrophobic chain. For liquid-ordered membranes the mobility was $0.41 \mu\text{m}^2/\text{s}$ and for disordered membranes it was reduced to $0.63 \mu\text{m}^2/\text{s}$. Obviously, PE introduced severe distortions of the membrane structure [131]. PE has a relatively small headgroup, which results in a significantly lower area per lipid leading to a high order of the hydrocarbon lipid tails and corresponding low lipid mobility. Furthermore, comparative studies of PE and PC using $^2\text{H-NMR}$ showed that PE molecules tend to form inter- and intramolecular hydrogen bonds, including association with other lipid types [132]. The amine group as a hydrogen-donor can strongly interact with other phosphate/carbonyl groups or water, which functions as hydrogen-acceptors. Probably, these strong intermolecular interactions cause a further reduction of lipid mobility.

To follow the general features of TAT peptides interaction with the model membranes we incubated pre-formed GUVs with AF-TAT peptides and 40 kDa FITC-dextran contained in glucose solution. Starting with 20 mol % of PE, the internalization of TAT was observed. Further increasing the PE mole fraction to 30 % yielded a higher translocation rate. However, any GUV destruction was not detected. Small tracer molecules were released from the GUVs, but neither 3 nor 70 kDa dextrans. So the size of pores induced in PE membranes should be smaller than in PS containing GUVs, up to 1.3 nm in diameter. The pore formation was not observable by single molecule tracking, probably due to extremely short life time. These results for TAT peptides are in agreement with recent data obtained by Herce et al. [20]. They demonstrated the flow of ions across and thus the presence of pores within a black lipid membrane system in the presence of nona-arginine and TAT peptide.

Unlike anionic membranes with high content of PS, single molecule tracking of fluorescent TAT peptides on the surface of PE containing GUVs revealed two distinct

3. Results and discussion

mobile fractions. One fraction had a distinct reduced mobility, $D=0.3 \mu\text{m}^2/\text{s}$, and the other mobile fraction showed the mobility of TAT “floating” on the membrane with $D=5.2 \mu\text{m}^2/\text{s}$. The fraction of the slow mobility component increased by a factor of 3 when the PE content in the membrane was increased from 10 to 30%. Also at 10 mol % PE a very small fraction of the slow component was identified (only 4 %), suggesting that the peptide is inserted in the membrane but the concentration is not enough to form pores and translocate. Interestingly, this slow fraction was even less mobile than the lipids themselves in these membranes. This slow diffusion coefficient suggested the presence of large molecular complexes comprising TAT peptides and lipids. The experiments with labelled lipids and B-TAT 2 μM showed that peptide binding does not compromise the mobility of the lipid bilayer. Similar results were obtained with SAXS by [19] were, even at lipid: peptide ratio high as 1.15:1, the PE membrane was not affected by the peptide (Figure 3.28).

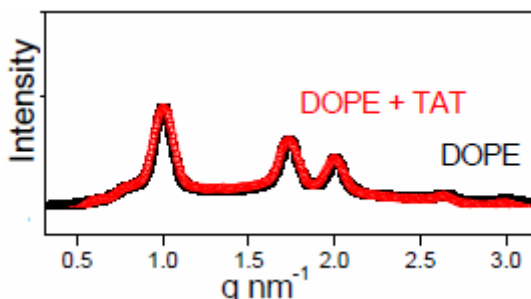


Figure 3.30: The native inverted hexagonal diffraction pattern of DOPE (black) remains unchanged upon addition of TAT CPP (red). The two diffraction patterns can be superimposed [19].

This observation excluded the hypothesis that lipid aggregates like micelles were formed. Instead, the TAT peptide could bind to the PE headgroup by hydrogen bonds in a structure similar to a pore formation, inducing a decrease in peptide mobility. At certain peptide concentration, a pore could be generated and would be open for a while, to allow the efflux of tracer molecules. This hypothesis was sustained by examination of the TAT trajectories which were more confined in membranes containing at least 20 mol % PE.

The Monte Carlo simulations were not performed for this situation because the model implies planar membranes and the effect of curvature induced by PE can not be simulated.

3.4. Interaction of TAT peptides with model membranes at physiological salt concentration

From bacteria to mammals, biological processes take place in salt solution. Maintaining a delicate balance of ions, biomembranes interact with different ion species. Considering the biological relevance of salt ions, the most important ones include Na^+ , K^+ , Cl^- , Ca^{2+} and Mg^{2+} . Monovalent ions such as Na^+ and K^+ are relevant in modulating the properties of plasma membrane. The divalent Ca^{2+} plays an important role in signal transduction pathways where it functions as second messenger signalling, *e.g.* in contraction of all muscle cell types, and it is a very good “cytosolic buffer” being stored inside of the cells in mitochondrial membranes or in the endoplasmatic reticulum [67].

All previous experiments (chapters 3.1-3.3) were done in sucrose/glucose solutions with all ions excluded from the medium. These conditions are though difficult to compare directly with those from live cell experiments. Hence, experiments in presence of salt solutions in order to approximate physiological conditions were also performed. For that, the GUVs generated from zwitterionic PC and anionic PS (20 mol %) with 20 mol % cholesterol were transferred into glucose solution containing 100 mM sodium chloride (NaCl).

3.4.1. Diffusion of single lipid analogs in model membranes in presence of 100 mM NaCl

Similar to previous experiments, in order to obtain a reference for bilayer mobility, the lipids were mixed with the tracer TR-DHPE (10^{-7} mol %). The jump distance analysis showed that the diffusion coefficients for saturated and unsaturated chains remained almost unchanged in presence of 100 mM NaCl compared to the desalted conditions (see Table 3.9 and Figure 3.31). Thus in neutral membranes, TR-DHPE moved more rapidly

3. Results and discussion

within GUVs known to comprise an unordered phase with a diffusion coefficient of $D=2.07\pm0.07 \text{ }\mu\text{m}^2/\text{s}$ compared to GUVs with an ordered phase, $D=0.51\pm0.01 \text{ }\mu\text{m}^2/\text{s}$. Similar in anionic membranes, TR-DHPE diffused faster within GUVs with an unordered phase with a diffusion coefficient of $D=2.0\pm0.07 \text{ }\mu\text{m}^2/\text{s}$ compared to GUVs, which had an ordered lipid phase, $D=0.50\pm0.01 \text{ }\mu\text{m}^2/\text{s}$.

Table 3.9: TR-DHPE mobility within GUVs in 100 mM NaCl

GUVs, 20 mol % chol NaCl 100 mM	$D_{SPT}, [\mu\text{m}^2/\text{s}]$			
	Saturated		Unsaturated	
	DPPC	DPPC/DPPS	DOPC	DOPC/DOPS
	0.51±0.01	0.50±0.01	2.07±0.07	2.0±0.07

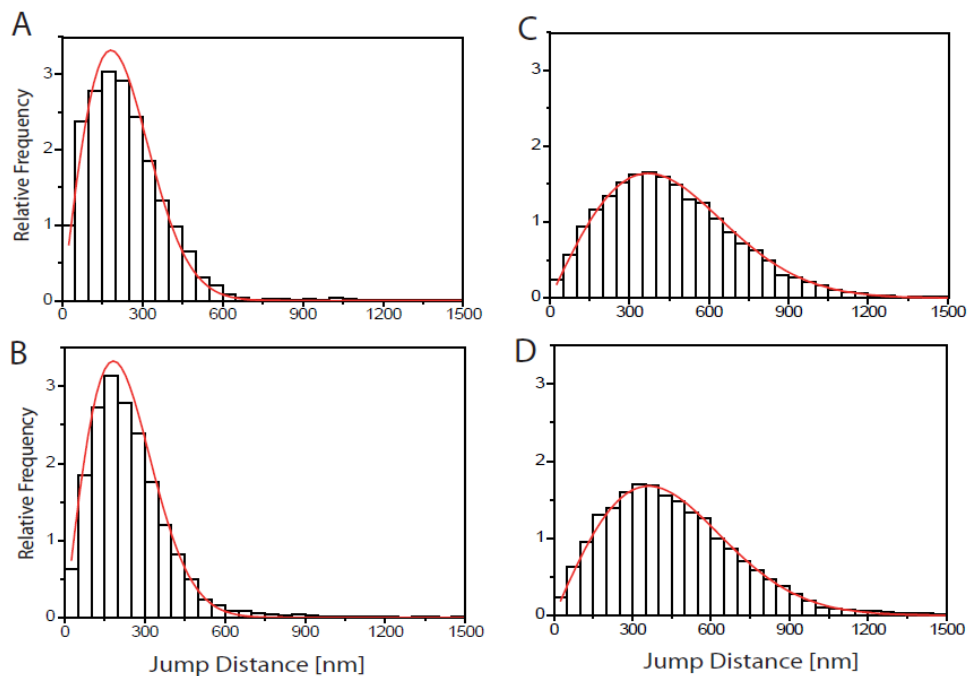


Figure 3.31: Analysis of TR-DHPE diffusion in neutral and anionic GUVs in 100 mM NaCl

(A) jump distance analysis for TR-DHPE in neutral GUVs with liquid-ordered lipid phase; (B) jump distance analysis for TR-DHPE in anionic GUVs with liquid-ordered lipid phase; (C) jump distance analysis for TR-DHPE in neutral GUVs with liquid-disordered lipid phase; (D) jump distance analysis for TR-DHPE in anionic GUVs with liquid-disordered lipid phase.

3.4.2. CLSM imaging of TAT peptide-GUVs interaction in NaCl solution

To observe the general interaction between TAT peptide and model membranes under the new conditions, the GUVs were incubated with 2 μ M AF-TAT and dextran molecules with molecular weight of 40 kDa labelled with FITC in glucose solution containing 100 mM NaCl. Neutral or anionic GUVs, with saturated and unsaturated hydrophobic chains were examined. In contrast to the “unsalted” conditions experiments, AF-TAT translocation into GUVs was observed already after a few minutes. Besides this, in a physiological NaCl solution TAT binding to GUVs was completely abrogated. Figure 3.32 shows an experiment for anionic GUVs prepared from DOPC/DPPC/DOPS/Chol = 30/30/20/20 incubated with 2 μ M of AF-TAT.

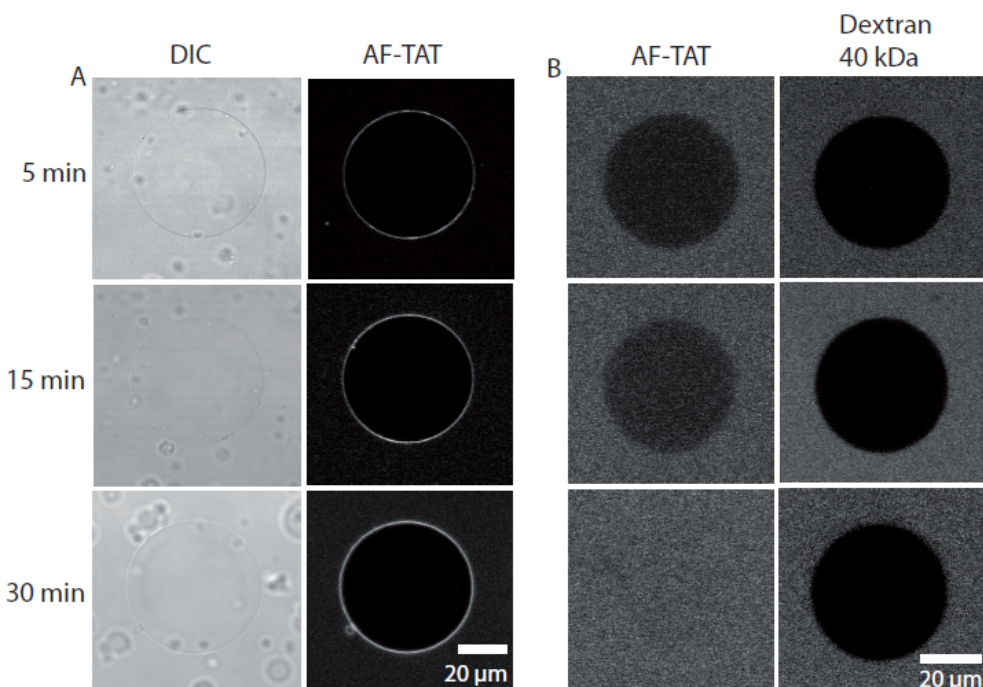


Figure 3.32: TAT peptide interaction with GUVs. Confocal images of the anionic GUVs incubated with 2 μ M AF-TAT in a glucose solution (A) and glucose solution containing 100 mM NaCl and 4 μ M 40 kDa FITC-dextran (B).

3. Results and discussion

Figure 3.32 (A) shows for comparison interaction between GUVs and TAT peptide in glucose solution without any salt in the external medium. In Figure 3.32 (B), in presence of 100 mM NaCl AF-TAT rapidly translocated across the GUV membrane (left panel). It took about 30 min until the AF-TAT concentration completely equilibrated inside and outside the GUVs. Similar results were obtained for neutral GUVs. To verify the intactness of GUVs, the experiment was performed in the presence of a 40 kDa fluorescein-labelled dextran, which was imaged in a separate fluorescence channel (right panel).

3.4.2.1. Influx of tracers in presence of TAT peptide

Since we observed that behaviour of TAT peptide was completely different in salt solution for the same composition of GUVs and the same peptide concentration, additional experiments were performed in order to understand this difference. So, neutral and anionic vesicles were incubated simultaneously with 2 μ M TAT peptide and tracers with different molecular weights: Lucifer Yellow, Alexa Fluor 488, 4 kDa and 40 kDa FITC-labelled dextrans. The purpose was to check whether the TAT peptide translocation was due to pore formation.

Generally, the translocation speed of TAT peptide varied widely between different vesicles. In an experiment with several GUVs of different diameters, incubated with 2 μ M TAT peptide and Lucifer Yellow one could observe that under the same conditions the translocation of peptides and tracers occurred with different velocities (Figure 3.33). Lucifer Yellow was a dye with a molecular weight of 386 Da and it was internalized simultaneously with AF-TAT. In absence of the peptide it remained excluded from GUVs. Peptide translocation was not GUVs size dependent. The vesicles (1 and 3) and (2 and 4) respectively had the same diameter, but only 1 and 4 were fully loaded with TAT peptide or tracer after 30 minutes.

3. Results and discussion

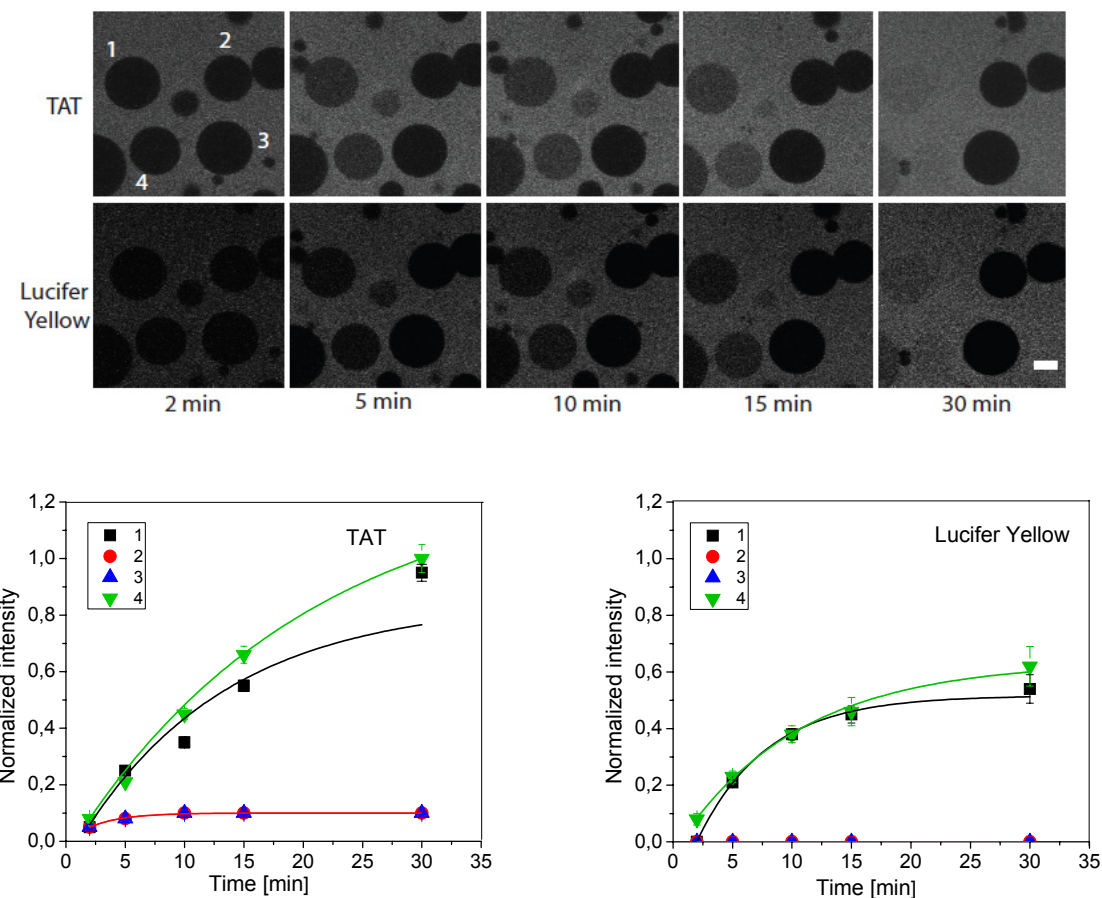


Figure 3.33: Internalization of TAT peptide and Lucifer Yellow in GUVs in presence of NaCl 100 mM. In the lower panel the measured fluorescence intensity values were normalized to the external intensity. The solid line represents the exponential fit. Scale bar 20 μm.

Similar results were obtained for Alexa Fluor 488. AF-TAT peptides equilibrated across the GUVs membrane within 30 min. Also the small dye AF488 was internalized, as expected (Figure 3.35). Beside this, a certain internalization of the 4 kDa dextran was observed (Figures 3.34 and 3.35). Like in the experiments from previous chapters, no influx of FITC-dextran 40 kDa was registered.

To be sure that the observed effect of dye internalization occurred only due to possibly pore formation induced by TAT peptide, control experiments without the peptide were done. As expected, there was no influx of the tracers in GUVs in absence of TAT (data not shown).

3. Results and discussion

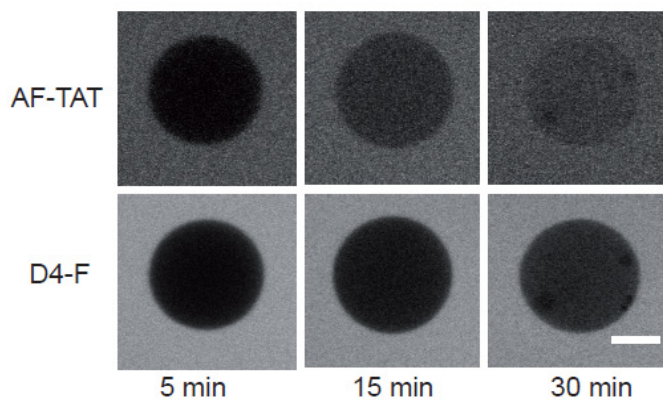


Figure 3.34: Internalization of TAT peptide and FITC-dextran 4 kDa in presence of 100 mM NaCl in a neutral GUV. The plots of normalized fluorescence intensity are depicted in Figure 3.35 A. Scale bar 20 μm

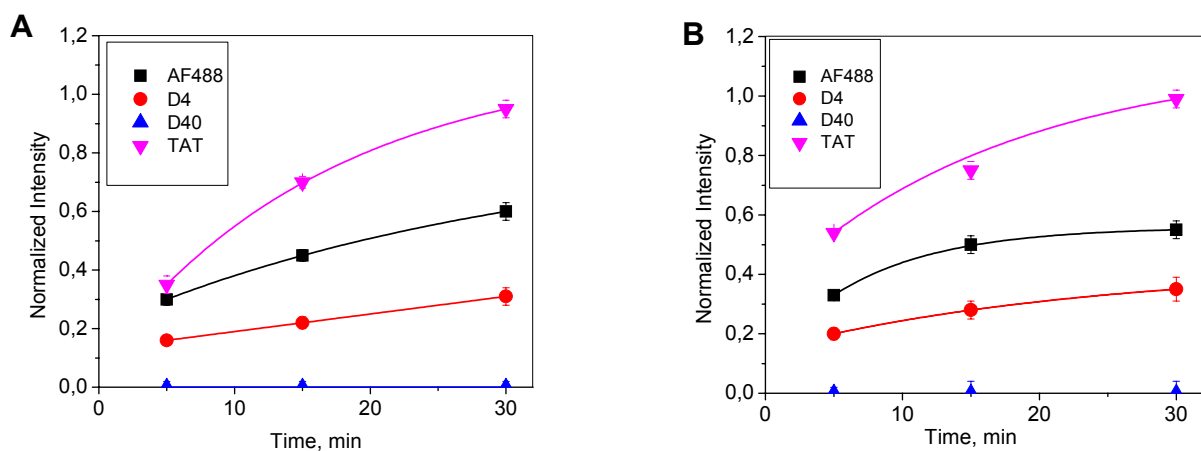


Figure 3.35: Internalization of TAT peptide and tracers in GUV in presence of NaCl 100 mM.
 (A) Translocation in neutral GUVs (DOPC/DPPC/chol); (B) Translocation in anionic GUVs (DOPC/DPPS/chol). The measured fluorescence intensity values corresponding to AF-TAT and dye accumulation inside of GUVs were normalized to the external intensity. The solid line represented an exponential fit. The data points were averaged for 5 vesicles.

3. Results and discussion

3.4.2.2. Efflux of tracers in presence of TAT peptide

To acquire more about the translocation way, similar leakage experiments as in case of GUVs containing PS or PE were performed. Fluorescent tracers with different molecular weights (Alexa488-maleimide, 1.3 kDa, Alexa546-dextran 3 kDa and Alexa546-dextran 70 kDa) were incorporated inside the GUVs. After incubation with 2 μ M AF-TAT, Alexa Fluor 488 dye molecules were completely released within 20 minutes from both neutral and anionic GUVs (Figures 3.36, 3.37 and 3.38). The dextrans (3 kDa and 70 kDa) did not pass the GUVs membranes (Figures 3.37 and 3.38). For these tracers the data points were averaged for 5 vesicles.

In the case of the small dyes, besides release of AF488, the GUVs were completely loaded with TAT within 20 min. For the bigger tracers which remained inside of the vesicles, the internalization of the peptide was less efficient for the same period of time (Figures 3.37 and 3.38).

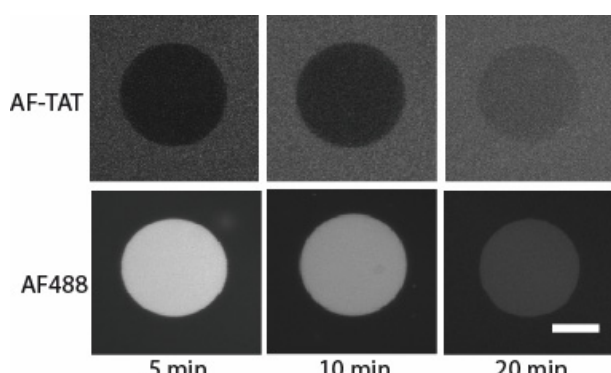


Figure 3.36: Pore formation in DOPC/DPPC/chol (neutral) membranes in 100 mM NaCl
The upper panel shows the internalization of AF-TAT and the lower panel presents the efflux of Alexa Fluor 488 from GUVs. The fluorescence intensity for both influx of TAT and efflux of the tracer is depicted in Figure 3.37. Scale bar 20 μ m.

3. Results and discussion

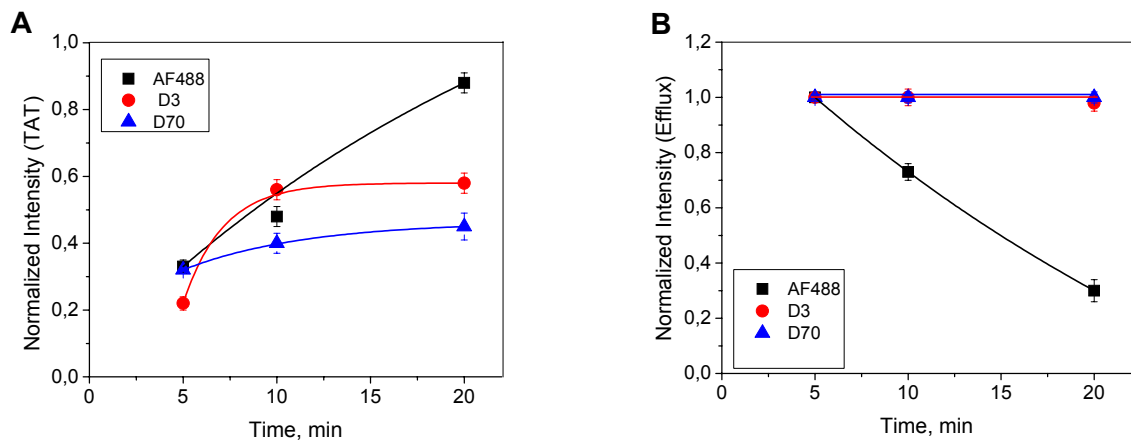


Figure 3.37: Internalization of TAT peptide in neutral GUVs (DOPC/DPPC/chol) and efflux of tracers in presence of 100 mM NaCl. (A) The measured fluorescence intensity values corresponding to the AF-TAT accumulation inside of GUVs were normalized to the external intensity. The solid line represents the result of an exponential fit. (B) Normalized fluorescence intensity for tracers with different sizes loaded inside of GUVs as indicated in the legend: AF488, 3 kDa Alexa546-dextran and 70 kDa Alexa546-dextran.

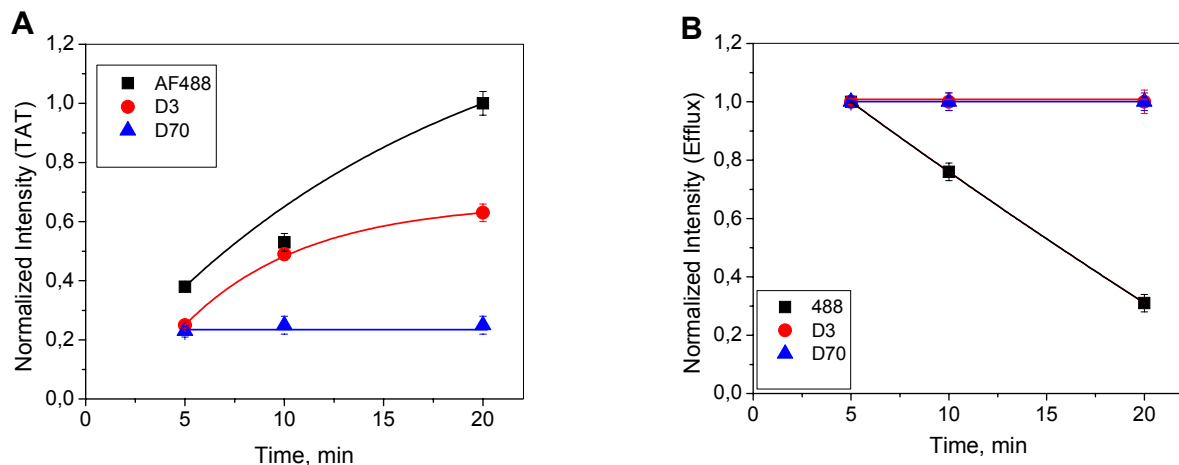


Figure 3.38: Internalization of TAT peptide in anionic GUVs (DOPC/DPPS/chol) and efflux of tracers in presence of NaCl 100 mM. (A) The measured fluorescence intensity values corresponding to the AF-TAT accumulation inside of GUVs were normalized to the external intensity. The solid line represents the exponential fit. (B) Normalized fluorescence intensity for tracers with different sizes loaded inside of GUVs. The data points were averaged for 5 vesicles.

3. Results and discussion

To confirm that the observed fluorescence decay was not due to photobleaching, control experiments for AF488, without peptides were performed. There was no change in fluorescence intensity for a similar number of images in these experiments (data not shown). The control experiments for the tracers were presented in Chapter 3.2, Figure 3.19.

These experiments revealed again that generally, the translocation speed varied widely between different vesicles. Figure 3.39(A) exhibits a GUV with several internal vesicles, loaded with AF488. In the presence of 2 μ M AF-TAT, the internalization of the peptide was observed (right) but the tracer efflux occurred at different rates. While the tracer was released from 2 vesicles, one is still fully loaded after 20 min. Figure 3.39 (B) shows the translocation of R-TAT (right) and the release of AF647 (left) after 20 min. Here are presented three GUVs with different diameters and one of them contains an internal membrane.

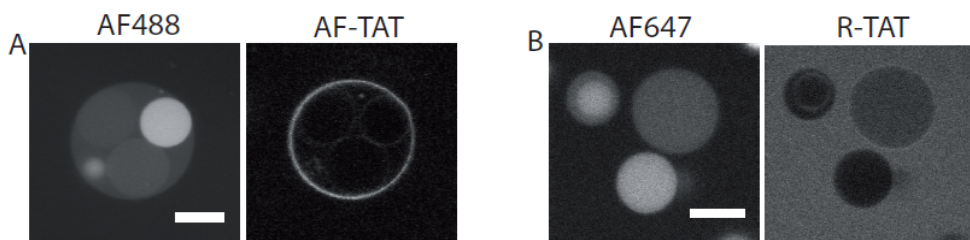


Figure 3.39: Internalization of TAT peptide and efflux of tracers in 100 mM NaCl after 20 min. (A) A GUV with several inner vesicles loaded with AF488 (left) and AF-TAT peptide (right) 2 μ M; (B) GUVs containing AF647 tracer (left) and translocation of R-TAT (right). Details are given in the text. Scale bar 20 μ m.

3.4.2.3. Influence of cholesterol on TAT peptide translocation

In a further experiment, cholesterol was excluded to check whether it plays a decisive role in TAT peptide behaviour. Figure 3.40 shows the efflux of AF488 in presence of 2 μ M AF-TAT and 100 mM NaCl. The result was similar to the experiments with cholesterol. Also, the simultaneous internalization of TAT with small dyes was checked (Figure 3.41)

3. Results and discussion

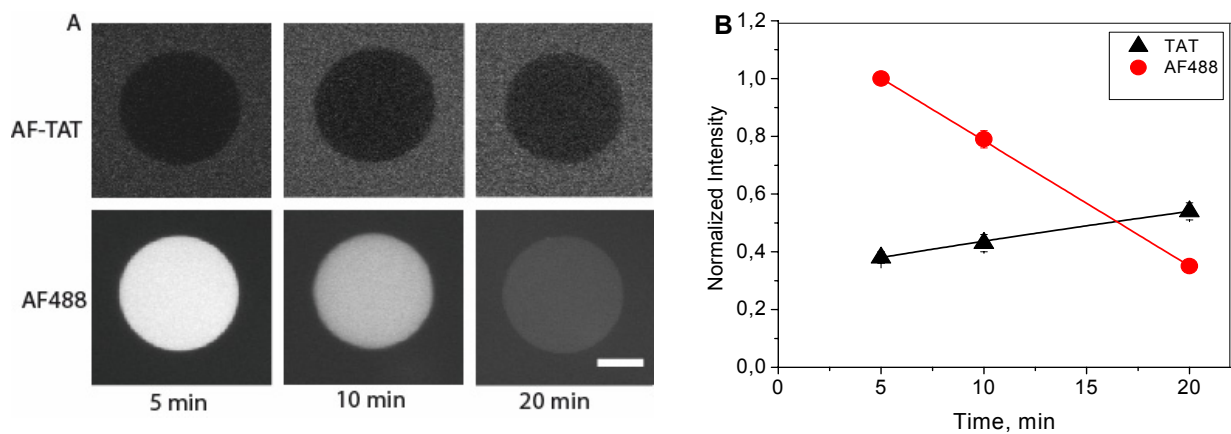


Figure 3.40: Pore formation in DOPC/DPPC = 80/20 (neutral) GUV in NaCl 100 mM
 (A) Upper panel shows the internalization of AF-TAT and the lower panel presents the efflux of Alexa Fluor 488 from GUVs. Scale bar 20 μ m. The fluorescence intensity for both influx of TAT and efflux of the tracer is depicted in (B).

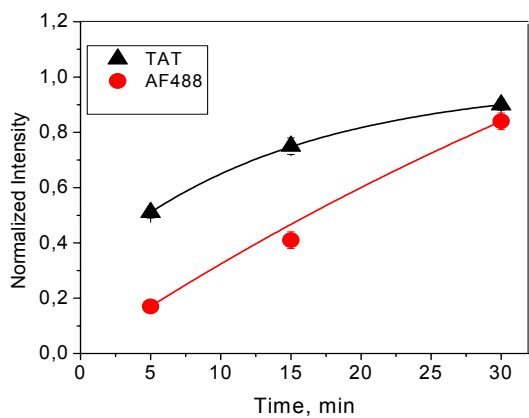


Figure 3.41: Internalization of TAT peptide and AF488 in DOPC/DPPC = 50/50 (neutral) GUV in presence of 100 mM NaCl. The data points were averaged for 5 vesicles.

3.4.2.4. Influence of other ion types on TAT peptide translocation

To verify whether specific ions played a decisive role in translocation process of TAT peptide in physiological salt condition, some other salts at the same concentration (100 mM) were tested (Figure 3.42).

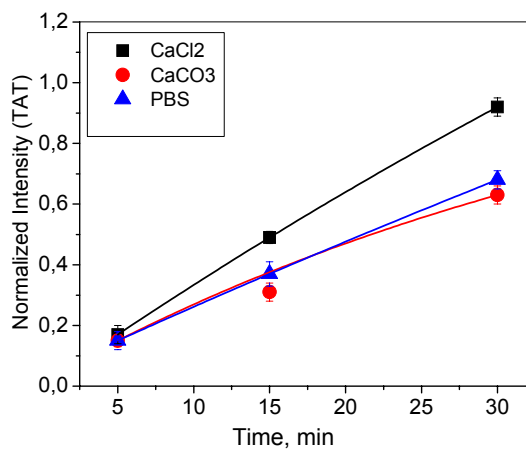


Figure 3.42: Internalization of TAT peptide in DOPC/DPPS/chol=60/20/20 (anionic) GUVs in presence of 100 mM salt solution. The data points were averaged for 5 vesicles.

CaCl₂ is a salt which contains bivalent cations and CaCO₃ has bivalent both, cations and anions comparing to NaCl with monovalent ions. Phosphate buffered saline (PBS) is a buffer solution commonly used in biological research. It is a salt solution containing sodium chloride, sodium phosphate, potassium chloride and potassium phosphate. The osmolarity and ion concentrations of the solution match those of the human body. The observed effect on TAT translocation was similar to NaCl for all these salt solutions (Figure 3.42). This observation leaded to the conclusion that the ion type and valence did not influence the internalization process.

3.4.3. Lateral mobility of TAT peptide on GUVs in NaCl solution

We also attempted to measure the dynamics of the TAT peptide on GUV surfaces in the glucose medium containing 100 mM NaCl. Notably, it was not possible to detect or visualize any TAT signals neither on anionic nor in neutral GUVs under these conditions, using frame rates up to 450 frame/s. Also confocal imaging did not show any accumulation of peptides on GUVs membrane either.

The diffusion constant of TAT peptides in pure buffer can be estimated based on the Stokes-Einstein equation [133]:

$$D = \frac{k_B T}{6\pi\eta r} \quad (7)$$

where D is the diffusion coefficient,

K_B is Boltzmann's constant,

T is the absolute temperature,

η is viscosity

r is the radius of the spherical particle

For TAT peptide the radius is $r=0.7$ nm (calculate with software from http://www.calctool.org/CALC/prof/bio/protein_length), glucose solution viscosity is 1.25 cP [134], k_B is 1.38×10^{-23} J/K, T is 298 K. The estimated value for diffusion coefficient was $D_{TAT, sol}=249 \mu\text{m}^2/\text{s}$ which was too fast to be observed at the employed imaging frame rates [109].

It was not possible to observe the peptide on the surface of GUVs, but still SPT could offer information about changes of membrane mobility during the translocation process. For that, the membranes were marked with TR-DHPE 10^{-7} mol %. The GUVs created in this way were added in a solution containing 2 μM B-TAT (unlabelled) and 100 mM NaCl. Simultaneously, comparable experiments without ions were performed. The aim was to check whether the dynamic of membrane was changed in presence of TAT (without ions) and TAT/NaCl solutions.

3.4.3.1. Diffusion of single lipid analogs in GUVs in presence of 2 μ M B-TAT

The experiments with labelled GUVs and 2 μ M B-TAT revealed that saturated membranes (neutral and anionic) were not affected by the high concentration of TAT peptide (see Table 3.10 and Figure 3.43). For a better comparison, the values for diffusion coefficients of the lipids without peptide (see chapter 3.2.1) were included in Table 3.10.

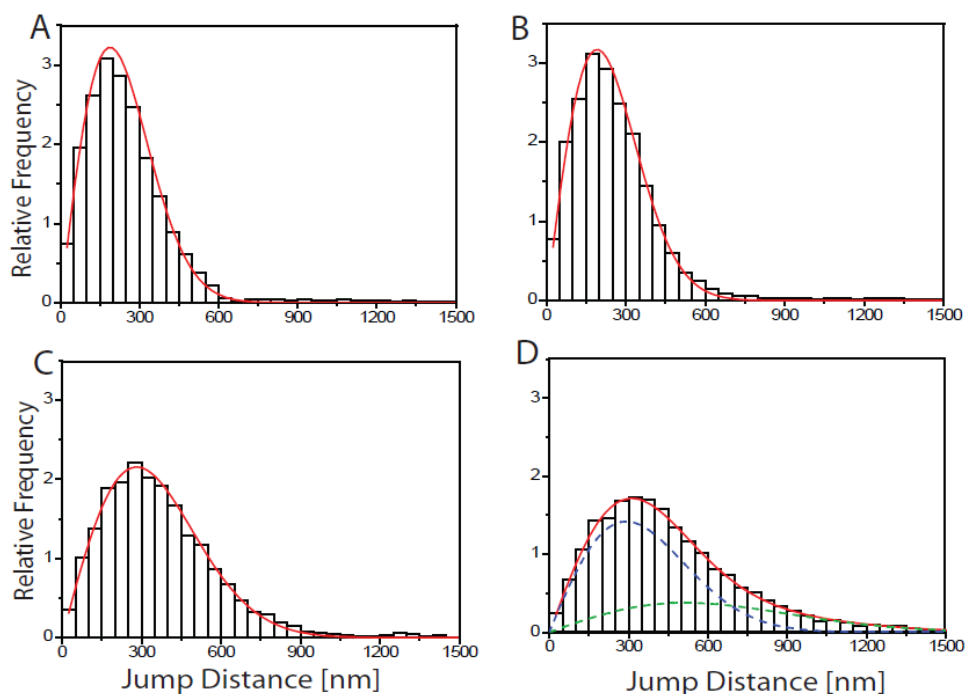


Figure 3.43: Analysis of TR-DHPE diffusion on neutral and anionic GUVs in presence of 2 μ M B-TAT. (A) jump distance analysis for TR-DHPE in neutral GUVs with liquid-ordered phase; (B) jump distance analysis for TR-DHPE in anionic GUVs with liquid-ordered phase; (C) jump distance analysis for TR-DHPE in neutral GUVs with liquid-disordered phase; (D) jump distance analysis for TR-DHPE in anionic GUVs with liquid-disordered phase.

Surprisingly, in unsaturated GUVs several changes were observed in presence of 2 μ M B-TAT. In neutral DOPC/chol vesicles, the diffusion coefficient was slowed down to $D=1.21\pm0.07 \text{ } \mu\text{m}^2/\text{s}$ compared to $D=2.2\pm0.02 \text{ } \mu\text{m}^2/\text{s}$ in the absence of the peptide (see section 3.2.1). Possibly, the positively charged peptides interact with the headgroup of several lipids and induce formation of lipid clusters structures. As a consequence the diffusion coefficient of unsaturated lipids is reduced. Probably, this effect was not

3. Results and discussion

observed in saturated bilayers because these lipids were more ordered and less susceptible to form such clusters. The anionic DOPC/DOPS/chol GUVs showed two diffusion coefficients: $D_1=1.31\pm0.06 \text{ }\mu\text{m}^2/\text{s}$ and $D_2=4.44\pm0.60 \text{ }\mu\text{m}^2/\text{s}$. The first one was alike mobility of neutral lipids and the second was similar to TAT peptide mobility (shown in chapter 3.2.1, Table 3.5). The presence of D_2 could be explained by a possible association of TAT peptide with the lipid tracer TR-DHPE and it reflects TAT diffusion coefficient on model membranes. This aspect was not observed in neutral unsaturated membranes probably because positively TAT is electrostatically more attracted to negatively charged PS lipids.

Table 3.10: TR-DHPE mobility within GUVs in a solution containing 2 μM B-TAT and 100 mM NaCl

Sample	$D_{SPT}, [\mu\text{m}^2/\text{s}]$				
	DPPC	DPPC/DPPS	DOPC	DOPC/DOPS	
B-TAT	0.54 \pm 0.01	0.56 \pm 0.01	1.21 \pm 0.07	1.31 \pm 0.06 (71%)	4.44 \pm 0.62 (29%)
B-TAT/NaCl	0.51 \pm 0.01	0.53 \pm 0.01	2.23 \pm 0.12	2.32 \pm 0.09	
Lipids mobility	0.56 \pm 0.01	0.54 \pm 0.01	2.20 \pm 0.02	2.01 \pm 0.01	

3.4.3.2. Tracking of single lipid analogs in GUVs in presence of 2 μM B-TAT and 100 mM NaCl

Comparable experiments in salt solution, showed no change in the lipids mobility of the saturated and unsaturated GUVs (Table 3.10 and Figure 3.44). In 100 mM NaCl, the mobility of lipid tracers in DOPC/chol or DOPC/DOPS/chol membranes was not affected by the TAT peptide. This could be explained by a charge compensation of TAT with anions from the medium. On the other hand this was not surprising since CLSM experiments showed the absence of peptide membrane staining in salt solution, the

3. Results and discussion

determinant factor for changing mobility of unsaturated lipids (see Figures 3.4, 3.12 and 3.32).

In presence of 2 μM B-TAT and 100 mM NaCl, TR-DHPE moved more rapidly within neutral GUVs known to comprise an unordered phase with a diffusion coefficient of $D=2.23\pm0.12 \text{ }\mu\text{m}^2/\text{s}$ compared to GUVs with an ordered phase, $D=0.51\pm0.01\text{ }\mu\text{m}^2/\text{s}$. Similar, TR-DHPE diffuse faster within anionic GUVs with an unordered phase with a diffusion coefficient of $D=2.32\pm0.09 \text{ }\mu\text{m}^2/\text{s}$ compared to GUVs, which exhibit an ordered phase, $D=0.53\pm0.01 \text{ }\mu\text{m}^2/\text{s}$. All these data corresponded to diffusion coefficients of lipid tracers in model membranes in absence of TAT and salt ions.

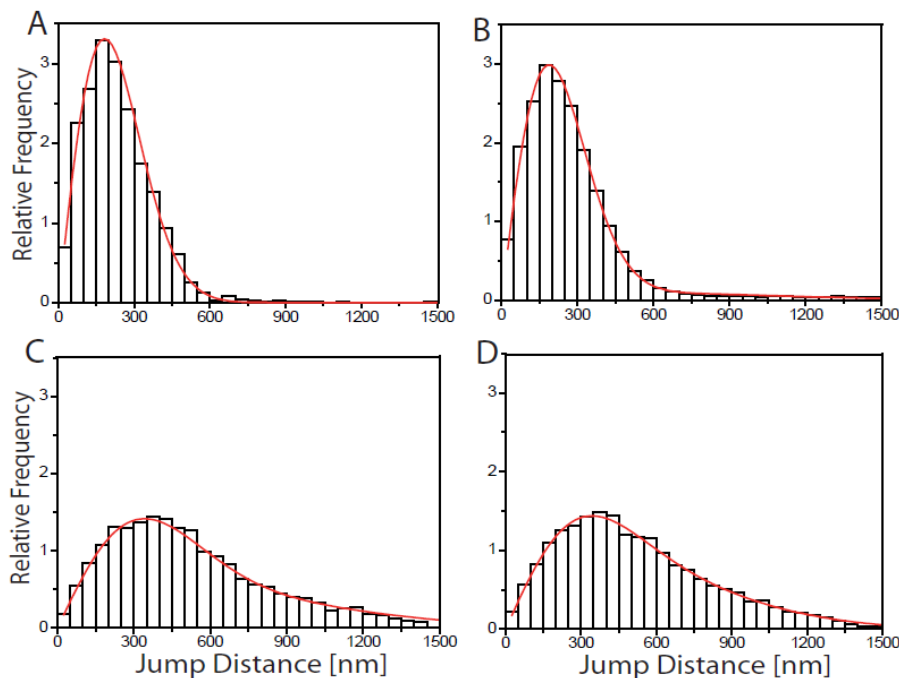


Figure 3.44: Analysis of TR-DHPE diffusion on neutral and anionic GUVs in presence of 2 μM B-TAT and 100 mM NaCl. ((A) jump distance analysis for TR-DHPE in neutral GUVs with liquid-ordered phase; (B) jump distance analysis for TR-DHPE in anionic GUVs with liquid-ordered phase; (C) jump distance analysis for TR-DHPE in neutral GUVs with liquid-disordered phase; (D) jump distance analysis for TR-DHPE in anionic GUVs with liquid-disordered phase.

3.4.4. Monte Carlo simulations

Monte Carlo simulations were performed for both neutral and anionic membranes for different NaCl concentrations: 0.001 M, 0.005 M, 0.02 M, 0.1 M and 0.154 M (Figure 3.45). The theoretical simulation showed no peptide internalization for any solution of different concentrations.

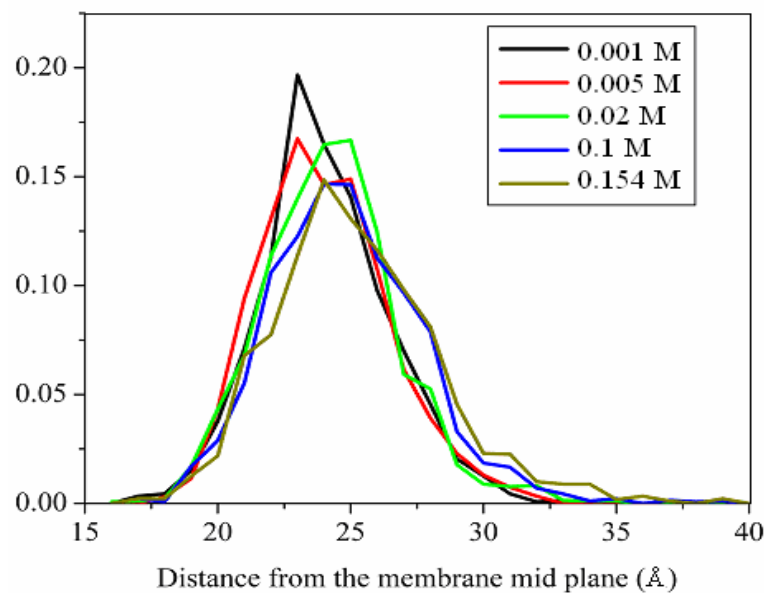


Figure 3.45: Distance distribution of TAT peptide from the membrane midplane for different concentration of NaCl solution.

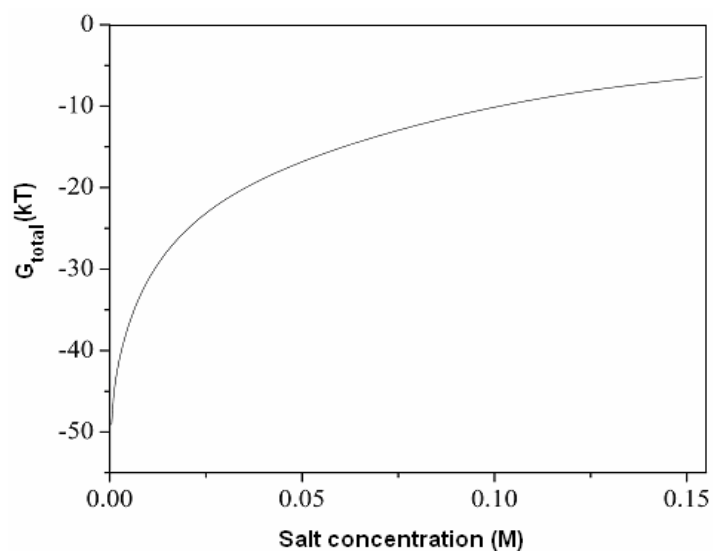


Figure 3.46: Peptide binding energy to the membrane as function of salt concentration.

3. Results and discussion

Apparently Na^+ ions shielded the membrane surface charge and TAT peptide was simply floating on the membrane. The simulations revealed that the binding strength of the peptide decreased with increasing of salt concentration (Figure 3.46). Thus the probability for translocation was reduced with increasing salt concentration.

Altogether, the Monte Carlo simulations did not support or offer an explanation for TAT peptide translocation in salt solutions. On the other hand, this theoretical model had limitations [135] as explained in section 2.9. Both the peptide and membrane were described using a reduced representation. For the peptide, each residue was represented by two interactions sites. The simplicity made the simulations computationally possible. This involved inaccuracies in the calculations, especially those related to the solvation free energy (eq. 4), which strongly depended on the location of each atom. Moreover, for different ions species, only the charge and not the spatial volume of the ion was taken in account, so it did not allow studies of specific peptide-lipid interactions in atomic detail. Hydrogen bonds and salt bridges between the peptide and lipid, as well as the exact stereochemistry of the interaction were not taken into consideration. These limitations could be the reason for the discrepancy between experiment and computations.

3.4.5. Discussion

Similar to the previous experiments, to have a reference, the mobility of the tracer TR-DHPE within GUVs membrane made from saturated and unsaturated, anionic and neutral lipids, was evaluated. The result showed that the diffusion coefficients of lipid tracers in all situations remained unchanged in presence of 100 mM NaCl compared to the desalted condition. So, the membrane viscosity was not affected by ions at this concentration. This observation was actually expected. Petrache et al. [136] demonstrated with X-ray diffraction experiments that monovalent salts do not affect the membrane structure below 1 M concentration. This result was confirmed later by EPR spectroscopy and DSC [137]. At concentration higher than 1 M both monovalent and divalent cations led to a significant increase in chain order, membrane thickness and membrane rigidity. These effects were more pronounced for CaCl_2 than for monovalent salts.

3. Results and discussion

CLSM experiments showed that physiological salt solutions dramatically changed the TAT peptide interaction with GUVs membranes. Any visible TAT binding to GUVs of all employed compositions was completely lost. The peptides now translocated efficiently into the GUV interior. However, in a previous study, a passive translocation of TAT into GUVs incubated with peptide in buffer solution was also observed [56]. In confocal images no membrane staining was detected, and also the extremely sensitive single molecule microscope did not reveal any trace of peptides on the GUVs surface.

The experiments with GUVs loaded with differently sized dyes pointed to the pore formation mechanism in the presence of 2 μM TAT and 100 mM NaCl. The result was similar for neutral and anionic, liquid-ordered and liquid-disordered membranes. Also, the same experimental evidence was registered for GUVs without cholesterol and for other salt solutions at the same concentration, 100 mM (CaCl₂, CaCO₃ or PBS).

In the SPT experiments for a membrane tracer in presence of 2 μM unlabelled TAT in glucose solution, no change in diffusion coefficients for liquid ordered membranes was detected. On the other hand, for neutral liquid-disordered GUVs a decrease in the mobility ($D = 1.21 \pm 0.06 \text{ } \mu\text{m}^2/\text{s}$) suggested possibility of clusters formation induced by TAT accumulated on the membrane. In the anionic DOPC/DOPS/chol GUVs two diffusion coefficients were found. $D_1 = 1.31 \pm 0.27 \text{ } \mu\text{m}^2/\text{s}$ was similar to the mobility of the membrane and $D_2 = 4.44 \pm 0.11 \text{ } \mu\text{m}^2/\text{s}$ was close to peptide mobility. This value indicated a possible association of accumulated TAT on anionic membranes with the tracer TR-DHPE.

When GUVs labelled with TR-DHPE were added in glucose/NaCl solution containing 2 μM B-TAT, the values for diffusion coefficients remained unchanged for both saturated and unsaturated lipid chains.

TAT peptide contained 6 arginines and 2 lysines, which made it highly cationic. It was clear that molecules of such high charge density cannot traverse the biological or artificial membranes at physiological pH without the presence of counterions. It should be noted that arginines (and also lysines) were strongly hydrophilic and their high pKa values ensured that they did remain protonated at relevant physiological conditions (see Figure 3.47).

3. Results and discussion

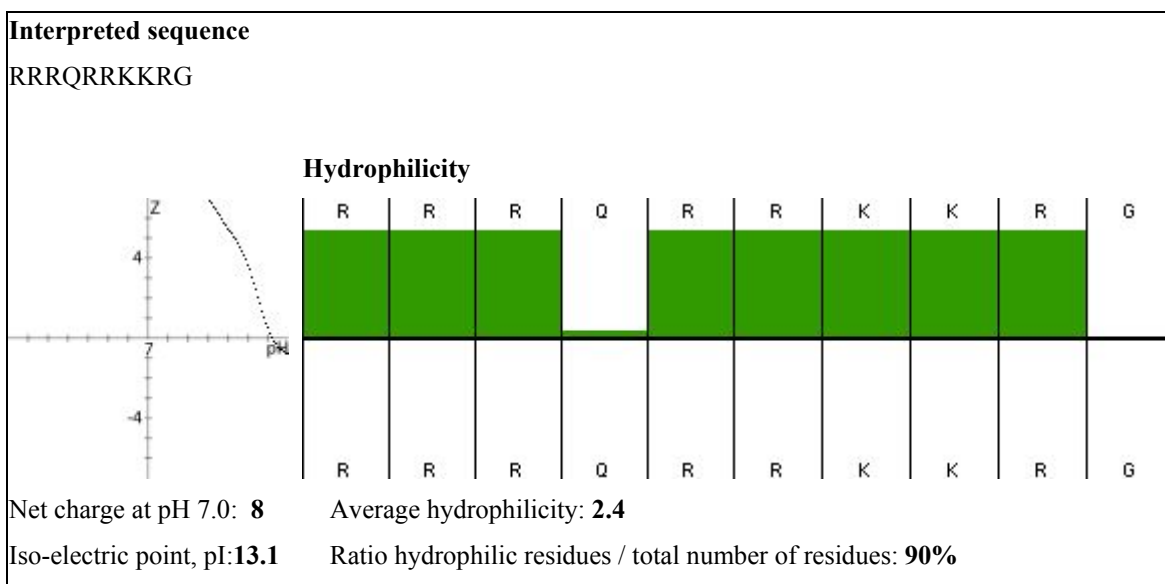


Figure 3.47: Hydrophilicity of TAT peptide estimated with the calculator based on Hoop-Woods scale from <http://www.innovagen.se/custom-peptide-synthesis/peptide-property-calculator.asp>

It has been suggested that membrane transport of arginine-rich peptides like TAT may be accomplished by charge neutralisation at the membrane surface, possibly by the interaction with sufficiently hydrophobic counter-ions such as anionic phospholipids [138], [139]. The resulting ion-pairs might be membrane soluble due to the hydrophobic character of the phospholipid tails and hence able to travel across the membrane and enter the GUVs.

The guanidinium groups from arginine had the property to form bidentate hydrogen bonds. It was shown that a guanidinium group had a very weak association with a counterion such as a phosphate group in an aqueous environment (~ 0.2 kcal/mol) [140]. When the guanidinium group approached the surface of a lipid bilayer and local polarity decreased, its association with a phosphate counter ion increased dramatically ($\sim 2.6\text{-}6.0$ kcal/mol)[141]. While the complex moved into less polar membrane, this association was further strengthened. Figure 3.48 shows a schematic association of the guanidinium groups with the membrane constituents [142].

The mechanism of ion pairing with the hydrophobic lipids was proved by water-octanol partitioning of arginine oligomers upon addition of sodium laurate, a surrogate for a membrane constituent [138]. The same authors proposed that the driving force for the passage of such ion pair complexes across the membrane was the membrane potential.

3. Results and discussion

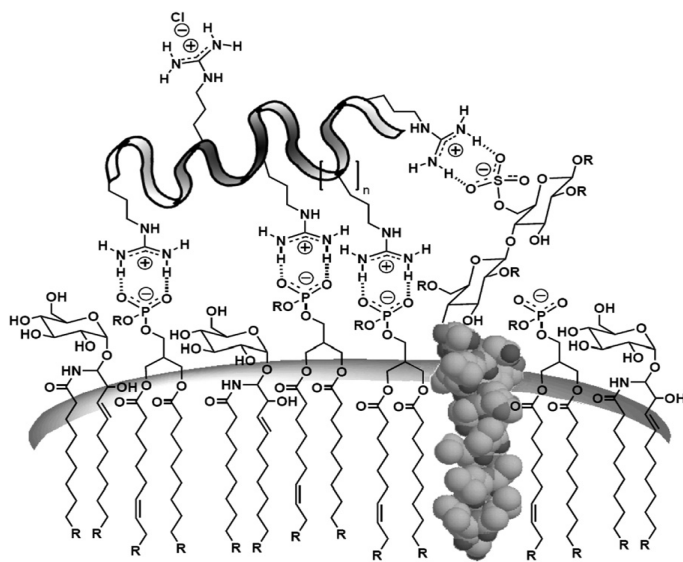


Figure 3.48: Representative associations of TAT based guanidinium transporter with anionic cell membrane constituents [142]

In this study, in glucose solution no internalization was observed, just accumulation of TAT on the membrane. Instead, in the presence of salt solution, the peptides freely diffused into GUVs. Based on these observations and theoretical understanding, the suggested mechanism of traslocation is as follows:

In glucose solution, the positively charged TAT peptides were attracted by the negative charges in GUVs membrane and they started to form associations through guanidinium groups with phosphate groups. According to Gouy-Chapman model of the double layer, the membrane surface has an electric potential called Zeta potential. In anionic GUVs the membrane surface was negatively charged but even zwitterionic lipids PC had a Zeta potential of -2.3 ± 2.0 mV [143]. In presence of TAT, some negative charges were compensated by forming the mentioned ion-pairs and thus the potential in external leaflet of GUVs decrease comparing to the internal one. So, a membrane potential could be induced. In absence of salt ions, this potential was either on equilibrium or not enough to favour peptides translocation (see Figure 3.49). When 100 mM NaCl was added, the small Na^+ ions were more accessible to the membrane and to compensate the negative charges. Obviously, this salt concentration was not enough to neutralize all the charges and some of them were compensated by ion-pairing with the guanidinium groups of TAT peptide. In this case, the difference between Zeta potential of bilayer surfaces was even higher than in glucose solution. So, one could expect to a greater membrane potential which favoured

3. Results and discussion

TAT peptide translocation (Figure 3.49). Moreover, this proposed mechanism could explain the differences apperead in traslocation speed of TAT peptides (see sections 3.4.2.1 and 3.4.2.2.). GUVs with a different membrane potential induced peptides internalization with different speeds, depending on potential value.

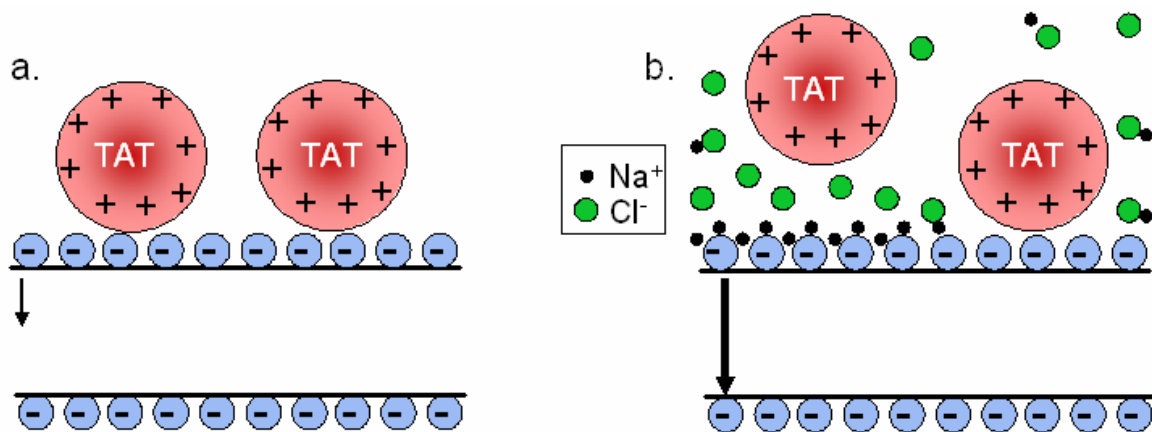


Figure 3.49: Schematic associations of TAT peptide with membrane surface in **a.** glucose solution and **b.** glucose solution containing 100 mM NaCl

4. NKCS- A study extended to antimicrobial peptides

Studies on interaction of TAT peptide with model membranes pointed to a pore formation mechanism similar to antibiotic peptides [19],[20], supported as well by the results from the chapter 3. Therefore, an extension of the studies to antimicrobial peptides, which supposedly act by membrane pore formation, should be most elucidative. NKCS, a derivative of NK-2 peptide is a promising member of peptide antibiotics [60]. It has efficient activity against both Gram negative and Gram positive bacteria. Two short derivatives, NKCS-[15-27] and NKCS-[15-27S] are included to study the partial activity of NKCS. Bacterial plasma membranes mainly consist of phosphoethanolamine (PE) and a high amount of anionic lipids like phosphatidylglycerol (PG) (see Table 1.3 for *E. coli*). Hence, for the next experiments we prepared GUVs consisting of PC, PE and PG. This research was done in cooperation with Agnieszka Rzeszutek and Regine Willumeit from GKSS Research Center, Geesthacht, Germany.

4.1. Results and discussion

4.1.1. Diffusion of single lipids analogs in model membranes

In order to obtain a reference for the measurements on model membranes we started out by studying the dynamics of the model bilayer systems. For that, the mobility of fluorescent lipid tracer TR-DHPE in GUVs of different lipid compositions was measured by single particle tracking. Three different sets of experiments were performed: GUVs created from DOPC representing the mammalian membrane, DOPC/POPE = 60/40 mol % and DOPC/POPG = 70/30 mol % respectively, to mimic the bacterial membrane.

The GUVs were generated by electroformation; therefore it was not possible to obtain vesicles from pure PE or pure PG. The results revealed that DOPC and DOPC/POPG mixture exhibits a very similar dynamic behaviour and lipids in DOPC/POPE membrane had a lower mobility compared with the other two (Table 4.1 and Figure 4.2 A for DOPC/POPG and DOPC/POPE).

Table 4.1: TR-DHPE mobility within GUVs

Sample	DOPC	DOPC/POPG	DOPC/POPE
$D_{SPT} [\mu\text{m}^2/\text{s}]$	5.3 ± 0.4	5.0 ± 0.2	3.7 ± 0.2

4.1.2. CLSM imaging of NKCS peptide-GUVs interaction

The GUVs prepared from DOPC, DOPC/POPG and DOPC/POPE were incubated with glucose containing 2 μM of NKCS, NKCS-[15-27] or NKCS-[15-27S] in order to verify the interaction of the peptides with the model membranes. To check the integrity of the GUVs, the experiments were performed in presence of FITC labelled dextran, 40 kDa, as in case of TAT peptide. The experiments showed no peptide internalization or accumulation on the pure DOPC membrane for NKCS and its shorter variants. Instead, for GUVs prepared from PE and PG lipids mixtures, both internalization and accumulation on the membrane were observed.

To test the hypotheses of pore formation, different fluorescent tracer molecules with increasing molecular weight (Alexa Fluor 488-maleimide, 0.64 kDa, Alexa Fluor 546-dextran 3 kDa; Alexa Fluor 546-dextran 70 kDa) were incorporated inside of the GUVs. After peptide addition the tracer fluorescence inside the GUVs was followed as a function of time. The observations after 30 minutes are summarized in the Table 4.2.

The experiments revealed, as expected, no efflux of the tracers from GUVs consist of DOPC for all 3 peptides. Also, no fluorescence was detected inside of these vesicles. In GUVs prepared from DOPC/POPG mixture, the internalization of all 3 peptides but no dye release was registered for NKCS-[15-27] and NKCS-[15-27S]. Only NKCS seems to induce small pores, since the dye release was observed only for AF488 in PG based

4. NKCS- A study extended to antimicrobial peptides

GUVs. Instead, the experiments revealed the complete release of Alexa488 and Alexa546-dextran 3 kDa within 30 minutes from DOPC/POPE membranes in presence of NKCS. For NKCS-[15-27] and NKCS-[15-27S], the tracers remained inside of GUVs in spite of the fact that peptides were internalized. Figure 4.1 shows the interaction of NKCS with GUVs prepared from DOPC, DOPC/POPG and DOPC/POPE loaded with 3 kDa dextran.

Table 4.2: Effects of NKCS peptides on GUVs loaded with different tracers

	NKCS	NKCS-[15-27]	NKCS-[15-27S]
DOPC			
Peptide influx	–	–	–
AF488 efflux	–	–	–
Peptide influx	–	–	–
Dextran 3 kDa efflux	–	–	–
Peptide influx	–	–	–
Dextran 70 kDa efflux	–	–	–
DOPC/POPG			
Peptide influx	+	+	+
AF488 efflux	+	–	–
Peptide influx	+	+	+
Dextran 3 kDa efflux	–	–	–
Peptide influx	+	+	+
Dextran 70 kDa efflux	–	–	–
DOPC/POPE			
Peptide influx	+	+	+
AF488 efflux	+	–	–
Peptide influx	+	+	+
Dextran 3 kDa efflux	+	–	–
Peptide influx	+	+	+
Dextran 70 kDa efflux	–	–	–

In order to examine the influence of ions present in the medium, a set of experiments with GUVs that were transferred not into glucose solution, but into 100 mM NaCl containing

glucose were performed. As before, the interaction of NKCS and its shorter variants with DOPC, DOPC/POPG and DOPC/POPE GUVs was tested. The experiments showed the same results as in the absence of salt solution (Table 4.2).

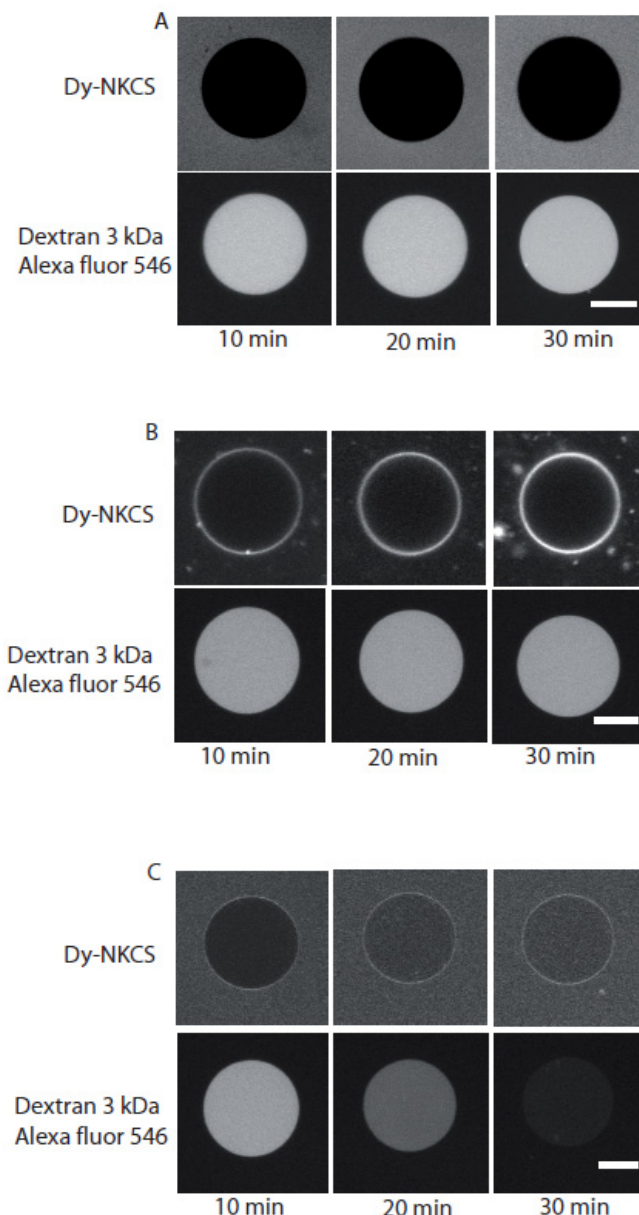


Figure 4.1: Translocation and pore formation by NKCS peptide in GUVs
 (A) Incubation of GUVs prepared from DOPC. The upper panel shows no internalization or accumulation of NKCS in these GUVs. The lower panel shows no leakage of dextrans 3 kDa labelled with Alexa Fluor 546.
 (B) The upper panel shows the binding and translocation of 2 μ M Dy-NKCS in GUVs formed by DOPC/POPG. The lower panel shows no leakage of dextrans 3 kDa labelled with Alexa Fluor 546.
 (C) Upper panel, binding and translocation of NKCS peptide, lower panel shows the release of 3 kDa dextran labelled with Alexa Fluor 546 from GUVs formed by DOPC/POPE. Scale bar, 20 μ m.

4.1.3. Lateral mobility of single NKCS on the GUVs surface

As in case of TAT peptide, SPT experiments of single fluorescently labelled NKCS peptides were performed on GUVs. For that the vesicles were incubated in glucose for 30 minutes with 0.5 nM Dy-NKCS. Parallel, experiments for shorter sequences of NKCS were done. Single Dy-peptides trajectories were recorded and the mobility characteristics were quantified by means of the jump distance histograms (see Figure 4.2 C and F for NKCS). Table 4.3 shows the diffusion coefficients for NKCS, NKCS-[15-27] and NKCS-[15-27S] peptides in GUVs prepared from DOPC, DOPC/POPG and DOPC/POPE respectively.

The peptides showed the same mobility on DOPC membranes as lipids. Also, in order to register enough events generating the jump distance histograms, the concentration of the peptide was increased to 1 nM. This observation confirmed at the single molecule level as well, there is no interaction of NKCS with PC membranes.

Table 4.3: NKCS peptides mobility on GUVs

Sample	NKCS	NKCS 15-27	NKCS 15-27S
DOPC			
$D_{SPT} [\mu\text{m}^2/\text{s}]$	5.6 ± 0.1	5.2 ± 0.2	5.0 ± 0.2
DOPC/POPG			
$D_{1,SPT} [\mu\text{m}^2/\text{s}]$	4.9 ± 0.3	4.4 ± 0.3	4.7 ± 0.3
Fraction 1	0.59	0.69	0.71
$D_{2,SPT} [\mu\text{m}^2/\text{s}]$	1.1 ± 0.1	0.8 ± 0.1	1.1 ± 0.1
Fraction 2	0.41	0.31	0.29
DOPC/POPE			
$D_{1,SPT} [\mu\text{m}^2/\text{s}]$	5.2 ± 0.7	5.2 ± 0.7	5.9 ± 0.5
Fraction 1	0.7	0.69	0.80
$D_{2,SPT} [\mu\text{m}^2/\text{s}]$	1.3 ± 0.3	0.9 ± 0.4	0.9 ± 0.3
Fraction 2	0.3	0.21	0.20

4. NKCS- A study extended to antimicrobial peptides

For GUVs prepared from DOPC/POPG and DOPC/POPE the jump distance histograms were clearly bi-modal, and two diffusion coefficients were required for a satisfactory fit of the data. One diffusion coefficient was similar to mobility of lipids and the other was much more reduced.

To monitor the effect of antimicrobial peptides on the bilayer, the mobility of lipids in the presence of 2 μM unlabelled peptide was analysed. For that, GUVs labelled with the tracer TR-DHPE were added in glucose solution containing 2 μM unlabelled peptides. The diffusion coefficients for lipids were presented in Table 4.4. The histograms for TR-DHPE in DOPC/POPG and DOPC/POPE in presence of NKCS were illustrated in Figure 4.2 B and E respectively.

Table 4.4: TR-DHPE mobility on GUVs incubated with 2 μM unlabelled peptides

Sample	NKCS	NKCS 15-27	NKCS 15-27S
DOPC			
$D_{\text{SPT}} [\mu\text{m}^2/\text{s}]$	5.4 ± 0.2	5.4 ± 0.2	5.1 ± 0.3
DOPC/POPG			
$D_{\text{SPT}} [\mu\text{m}^2/\text{s}]$	3.6 ± 0.3	3.8 ± 0.3	3.9 ± 0.2
DOPC/POPE			
$D_{1,\text{SPT}} [\mu\text{m}^2/\text{s}]$	5.0 ± 0.6	5.8 ± 0.7	5.7 ± 0.6
Fraction 1	0.57	0.60	0.53
$D_{2,\text{SPT}} [\mu\text{m}^2/\text{s}]$	1.2 ± 0.1	1.3 ± 0.3	1.4 ± 0.2
Fraction 2	0.43	0.40	0.47

In these experiments DOPC mobility was not affected by the presence of 2 μM peptides. DOPC/POPG dynamic was reduced and only one component was required to fit the histograms in contrast to DOPC/POPE which showed the same diffusion coefficients as for peptides (Table 4.4).

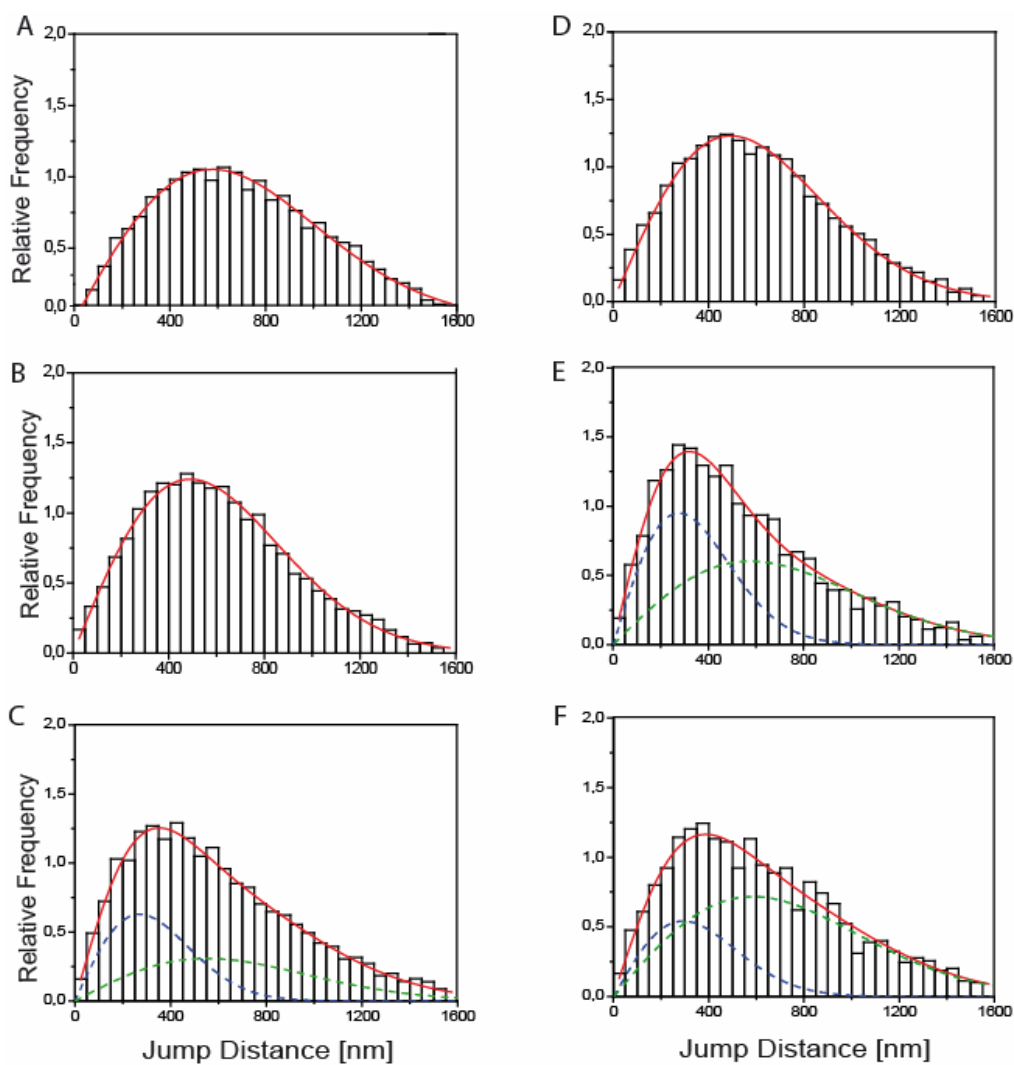


Figure 4.2: (A) and (D) Jump distance analysis for TR-DHPE in GUVs prepared from DOPC/POPG and DOPC/POPE. (B) and (E) Jump distance analysis for TR-DHPE in PG and PE GUVs in presence of 2 μ M unlabelled NKCS. (C) and (F) Jump distance analysis for 0.5 nM NKCS on GUVs formed by DOPC/POPG and DOPC/POPE respectively.

4.1.4. Discussions

The dynamics of the model bilayer systems -DOPC representing the mammalian membrane, DOPC/POPE = 60/40 mol % and DOPC/POPG = 70/30 mol % respectively, mimicking the bacterial membrane- were studied. These experiments provide us with a reference for the diffusion coefficients of model membranes. The evaluation of recorded movies revealed that DOPC and DOPC/POPG mixtures exhibit a very similar dynamic behaviour ($D=5.3\pm0.4 \mu\text{m}^2/\text{s}$ and $D=5.0\pm 0.2\mu\text{m}^2/\text{s}$). This result was not surprising since

both DOPC and POPG are in liquid-crystalline phase at experiments temperature. The membrane consisting of DOPC/POPE had a lower mobility compared with the other two ($D=3.7\pm0.2 \mu\text{m}^2/\text{s}$). This result was expected since PE has a relatively small headgroup, which leads to significantly lower area per lipid and in consequence to a high order of the hydrocarbon lipid tails and corresponding low lipid mobility, as explained in 3.3.4. Besides this, PE was in gel phase at room temperature and PC in the liquid-crystalline phase, so a high order was expected. Though, it was not possible to identify 2 diffusion coefficients corresponding to the different lipid phases. Probably, because the PE domains are too thin to produce a distinct mobility (see Figure 2.2.B from Chapter 2). It should be mentioned here that GUVs were prepared without cholesterol which led to a considerably higher diffusion coefficient for DOPC. In previous study for TAT peptide, mobility for PC/chol membranes was $2.01\pm0.01 \mu\text{m}^2/\text{s}$. This observation was consistent with the results reported in literature, which showed that incorporation of cholesterol into phospholipids membrane increased the bilayer thickness and reduced its mobility [87].

The CLSM experiments revealed after incubation of GUVs prepared from DOPC with $2\mu\text{M}$ NKCS, NKCS-[15-27] and NKCS-[15-27S], no peptide import or accumulation on membrane. Also, the experiments with GUVs loaded with different tracers showed no dye release, suggesting no interaction with DOPC and implicitly with mammalian membranes. These results were supported by Andra et al. [62]. The authors detected by FRET and CD no interaction of PC liposomes with NKCS (named NK27 in their paper). Furthermore, after particle tracking of NKCS and its variants on DOPC membranes, the diffusion coefficients were very similar to those of the membrane, even at high peptide concentration ($2 \mu\text{M}$). This means that only sporadically and for short time the peptide is attached to the membrane, but without any relevant interaction.

In DOPC/POPG membranes, the internalization and accumulation on the GUVs of all three peptides was observed. The efflux experiments showed the release solely for AF488 tracer and NKCS. It seems that only this peptide is able either to induce small pores in PG membranes or changes in diffusion constant of the membrane which could lead to the dye release. From SPT experiments instead we could conclude that there is no difference in the behaviour of all three peptides. We found two diffusion coefficients, one comparable to the bilayer mobility and the second significantly reduced, pointing to peptide insertion into membrane. This idea is supported by the fact that at high concentration of unlabelled

4. NKCS- A study extended to antimicrobial peptides

peptide, the mobility of lipids in the membrane is reduced from $D=5.0\pm0.2$ to $D=3.6\pm0.5$ $\mu\text{m}^2/\text{s}$. Also, the FRET and CD experiments performed by Andra et al. [62] suggested that NKCS is intercalated in PG liposomes.

NKCS, NKCS-[15-27] and NKCS-[15-27S] were internalized into GUVs formed by DOPC/POPE as well. They showed also an accumulation on the membrane. Similar to PG experiments, the efflux of tracer was observed only for NKCS, but this time besides AF488 3 kDa dextran was released too. SPT experiments revealed a deeper insertion compared to PG membranes of the peptides into bilayer, since the diffusion coefficients for lipid at high concentration of unlabelled peptide are comparable with those of the peptide on GUVs. Also the percent of slower component was increased as well.

Similar results were obtained in presence of 100 mM NaCl, showing that essential for peptide activity was the direct interaction with the phospholipids and not existent ions in the medium.

We should underline here that bilayer mobility in presence of 2 μM **B-TAT** (unlabelled) was not changed unlike NKCS. Therefore, because the NKCS peptide induces considerable modifications in lipids mobility in GUVs prepared from PG and PE, besides the pore formation mechanism, a possible explanation for dye release could be also the changed diffusion constants of the membranes.

Altogether, we can conclude that TAT peptide behave similar to NKCS, inducing pores in PE and anionic membranes (PS for TAT and PG for the antimicrobial peptides). Also, for PE based GUVs, two diffusion coefficients were detected for both types of peptides, suggesting a deep insertion of peptide into the membrane and a similar mechanism. Instead, in PG membranes, NKCS and its shorter variants showed two diffusion coefficients, in contrast to TAT peptide mobility on GUVs containing PS, whose jump distance histograms were fitted with a single component. This observation could indicate a possibly different mechanism of action for CPPs and antimicrobial peptides in anionic membranes. A noticeable difference between TAT and NKCS was in GUVs prepared from PC, only the first one showing interaction and accumulation on this type of membrane. While for the CPP-TAT the ions from medium seemed to play a very important role for peptide translocation, NKCS activity was not affected in any way by 100 mM salt solution.

5. Summary and Outlook

The present thesis is a detailed study on interaction of cell-penetrating TAT peptides with model membranes in different experimental conditions. The first part of the study was focused on direct interaction between TAT peptides and lipids with all ions excluded from the medium. We found that while lipid mobility varied clearly with the phase state of the membranes, the peptide mobility was independent on membrane hydrophobic core, but dependent on lipid headgroups. Confocal experiments showed that TAT peptide accumulated without translocation on surface of neutral GUVs formed by PC and cholesterol and on anionic GUVs with a content of PS between 15-30 mol %. Introduction of a higher amount of anionic lipids (40 mol %) resulted in peptide translocation. In some cases TAT provoked membrane destabilization leading to vesicle disruption, an effect which could be assigned to a carpet-like lysis mechanism. Furthermore, a clear translocation across membranes containing 20 mol % of lipids known to induce a negative curvature (PE) was observed. In both cases, TAT peptides were capable to form nanometres-sized pores, which could be passed by small but not large dye tracer molecules.

In the second part of the thesis, the influence of ions on TAT peptides translocation was studied. CLSM experiments showed that in presence of 100 mM NaCl solution the TAT interaction with the GUVs membrane was completely altered. Any detectable TAT binding to GUVs was entirely lost while the peptides translocated efficiently into the vesicles interior. The experiments with GUVs loaded with dyes of different molecular weights sustained again a pore formation in presence of 2 μ M TAT and 100 mM NaCl. The result was similar for neutral and anionic, liquid-ordered and liquid-disordered membranes. Also, there was no difference in TAT behaviour for GUVs without cholesterol or in case of other salt solutions at the same concentration, 100 mM (CaCl₂, CaCO₃ or PBS). In this case we assumed that TAT formed ion-pairs between the guanidinium groups and phosphate counter ions from lipid headgroups and then a membrane potential enabled the peptides translocation and pore formation.

To summarize, we found that internalization of TAT in membrane depends on: amount of charge in the headgroups, negative curvature of involved lipids, e.g molar ratio of PE, ions

5. Summary and Outlook

present in the medium. In all cases where the translocation was observed, a pore formation by TAT can be concluded.

In the last part of this thesis interaction of NKCS antimicrobial peptides, which supposedly act by membrane pore formation, with model membranes was studied. We observed that TAT peptides behaved similar to NKCS, inducing pores in PE and anionic membranes (PS for TAT and PG for the antimicrobial peptides). A clear difference between TAT and NKCS was in GUVs prepared from PC, only CPPs showing interaction and accumulation on this type of membrane. Also for TAT the ions from medium seemed to play a very important role for peptide translocation, but NKCS activity was not influenced by 100 mM salt solution.

TAT peptides represent a powerful tool for the development of cell-permeable agents. Their property to deliver a broad variety of cargoes inside of the cells is well-known. A perspective for this thesis might be to study the interaction of TAT peptide conjugated to different types of molecules with GUVs. This could clarify hypotheses that passive mechanism of translocation is valid for small molecules, while big cargoes attached to TAT are internalised by active endocytosis.

The experiments presented in this thesis showed that TAT peptides internalization is favoured by PE and PS. PE is a lipid frequently occurring in bacterial membranes and PS is a lipid present at high concentration in the outer membrane leaflet of cancer cells. A further study might be to test TAT for antimicrobial properties and anticancer activity. So, besides numerous applications of TAT peptide as powerful delivery agent for biology, imaging and biotechnology, these additional applications for therapeutics and medicine should be considered as well.

6. Acknowledgements

My sincerest thanks go to Prof. Dr. Ulrich Kubitscheck, for giving me the opportunity to do my PhD studies in this interesting field. I appreciated his constant guidance during the thesis project, his confidence, and the interesting discussions on my project.

I am grateful to Prof. Beate Klösgen for stimulating scientific discussions and kind suggestions.

Additionally, I want to thank the members of my PhD Committee, Prof. Rudolf Merkel and Prof. Hans-Georg Sahl for a constructive criticism of the thesis.

I thank to Gisela Tünnemann and M. Cristina Cardoso, Max Delbrück Center for Molecular Medicine, Berlin, for kindly providing us the R-TAT and B-TAT peptide samples.

I thank to Agnieszka Rzeszutek and Regine Willumeit from GKSS Research Centre, Geesthacht, Germany for providing the NKCS peptides and for stimulating discussions.

I thank for collaboration, input and interesting discussions on my PhD project to colleagues from BIOCONTROL network.

I want to thank Yana Gofman for performing the Monte Carlo simulations.

I want to express my sincere thanks to the former and present colleagues who created an atmosphere of friendship and made life enjoyable during my PhD work.

Special thanks to our department secretaries, Beate Bongart and Ilka Technau for their never-ending patience in administrative matters.

My beloved husband Alin has patiently supported me through ups and downs of the thesis project. Without his love and understanding attitude this work would have been much harder.

Tin sa le multumesc parintilor meu, Ermina si Vasile, pentru sprijnul si incurajarile lor.

This study was financially supported by the European Commission under the 6th Framework Programme through the Marie-Curie Action BIOCONTROL, contract number MCRTN – 33439.

Thank you!

7. References

1. Dietz, G.P. and M. Bahr, *Delivery of bioactive molecules into the cell: the Trojan horse approach.* Mol Cell Neurosci, 2004. **27**(2): p. 85-131.
2. Richard, J.P., et al., *Cell-penetrating peptides. A reevaluation of the mechanism of cellular uptake.* J Biol Chem, 2003. **278**(1): p. 585-90.
3. Schwarze, S.R., K.A. Hruska, and S.F. Dowdy, *Protein transduction: unrestricted delivery into all cells?* Trends Cell Biol, 2000. **10**(7): p. 290-5.
4. Lindgren, M., et al., *Cell-penetrating peptides.* Trends Pharmacol Sci, 2000. **21**(3): p. 99-103.
5. Derossi, D., G. Chassaing, and A. Prochiantz, *Trojan peptides: the penetratin system for intracellular delivery.* Trends Cell Biol, 1998. **8**(2): p. 84-7.
6. Fischer, R., et al., *Break on through to the other side-biophysics and cell biology shed light on cell-penetrating peptides.* Chembiochem, 2005. **6**(12): p. 2126-42.
7. Drin, G., et al., *Studies on the internalization mechanism of cationic cell-penetrating peptides.* J Biol Chem, 2003. **278**(33): p. 31192-201.
8. Fittipaldi, A., et al., *Cell membrane lipid rafts mediate caveolar endocytosis of HIV-1 Tat fusion proteins.* J Biol Chem, 2003. **278**(36): p. 34141-9.
9. Ferrari, A., et al., *Caveolae-mediated internalization of extracellular HIV-1 tat fusion proteins visualized in real time.* Mol Ther, 2003. **8**(2): p. 284-94.
10. Kaplan, I.M., J.S. Wadia, and S.F. Dowdy, *Cationic TAT peptide transduction domain enters cells by macropinocytosis.* J Control Release, 2005. **102**(1): p. 247-53.
11. Khalil, I.A., et al., *High density of octaarginine stimulates macropinocytosis leading to efficient intracellular trafficking for gene expression.* J Biol Chem, 2006. **281**(6): p. 3544-51.
12. Duchardt, F., et al., *A comprehensive model for the cellular uptake of cationic cell-penetrating peptides.* Traffic, 2007. **8**(7): p. 848-66.
13. Mayor, S. and R.E. Pagano, *Pathways of clathrin-independent endocytosis.* Nat Rev Mol Cell Biol, 2007. **8**(8): p. 603-12.

7. References

14. Ziegler, A. and J. Seelig, *Interaction of the protein transduction domain of HIV-1 TAT with heparan sulfate: binding mechanism and thermodynamic parameters.* Biophys J, 2004. **86**(1 Pt 1): p. 254-63.
15. Ziegler, A. and J. Seelig, *Binding and clustering of glycosaminoglycans: a common property of mono- and multivalent cell-penetrating compounds.* Biophys J, 2008. **94**(6): p. 2142-9.
16. Patel, L.N., J.L. Zaro, and W.C. Shen, *Cell penetrating peptides: intracellular pathways and pharmaceutical perspectives.* Pharm Res, 2007. **24**(11): p. 1977-92.
17. Prochiantz, A., *Messenger proteins: homeoproteins, TAT and others.* Curr Opin Cell Biol, 2000. **12**(4): p. 400-6.
18. Herce, H.D. and A.E. Garcia, *Molecular dynamics simulations suggest a mechanism for translocation of the HIV-1 TAT peptide across lipid membranes.* Proc Natl Acad Sci U S A, 2007. **104**(52): p. 20805-10.
19. Mishra, A., et al., *HIV TAT forms pores in membranes by inducing saddle-splay curvature: potential role of bidentate hydrogen bonding.* Angew Chem Int Ed Engl, 2008. **47**(16): p. 2986-9.
20. Herce, H.D., et al., *Arginine-rich peptides destabilize the plasma membrane, consistent with a pore formation translocation mechanism of cell-penetrating peptides.* Biophys J, 2009. **97**(7): p. 1917-25.
21. Shai, Y., *Mode of action of membrane active antimicrobial peptides.* Biopolymers, 2002. **66**(4): p. 236-48.
22. Jenssen, H., P. Hamill, and R.E. Hancock, *Peptide antimicrobial agents.* Clin Microbiol Rev, 2006. **19**(3): p. 491-511.
23. Zasloff, M., *Antimicrobial peptides of multicellular organisms.* Nature, 2002. **415**(6870): p. 389-95.
24. Frankel, A.D. and C.O. Pabo, *Cellular uptake of the tat protein from human immunodeficiency virus.* Cell, 1988. **55**(6): p. 1189-93.
25. Green, M. and P.M. Loewenstein, *Autonomous functional domains of chemically synthesized human immunodeficiency virus tat trans-activator protein.* Cell, 1988. **55**(6): p. 1179-88.
26. Anderson, D.C., et al., *Tumor cell retention of antibody Fab fragments is enhanced by an attached HIV TAT protein-derived peptide.* Biochem Biophys Res Commun, 1993. **194**(2): p. 876-84.
27. Fawell, S., et al., *Tat-mediated delivery of heterologous proteins into cells.* Proc Natl Acad Sci U S A, 1994. **91**(2): p. 664-8.

7. References

28. Wender, P.A., et al., *The design, synthesis, and evaluation of molecules that enable or enhance cellular uptake: peptoid molecular transporters*. Proc Natl Acad Sci U S A, 2000. **97**(24): p. 13003-8.
29. Tunnemann, G., et al., *Cargo-dependent mode of uptake and bioavailability of TAT-containing proteins and peptides in living cells*. Faseb J, 2006. **20**(11): p. 1775-84.
30. Dietz, G.P., et al., *Application of a blood-brain-barrier-penetrating form of GDNF in a mouse model for Parkinson's disease*. Brain Res, 2006. **1082**(1): p. 61-6.
31. Zhao, M., et al., *Differential conjugation of tat peptide to superparamagnetic nanoparticles and its effect on cellular uptake*. Bioconjug Chem, 2002. **13**(4): p. 840-4.
32. Polyakov, V., et al., *Novel Tat-peptide chelates for direct transduction of technetium-99m and rhenium into human cells for imaging and radiotherapy*. Bioconjug Chem, 2000. **11**(6): p. 762-71.
33. Sebbage, V., *Cell-penetrating peptides and their therapeutic applications*. Bioscience Horizons, 2009. **2**(1): p. 64-72.
34. Santra, S., et al., *Rapid and effective labeling of brain tissue using TAT-conjugated CdS:Mn/ZnS quantum dots*. Chem Commun (Camb), 2005(25): p. 3144-6.
35. Ruan, G., et al., *Imaging and tracking of tat peptide-conjugated quantum dots in living cells: new insights into nanoparticle uptake, intracellular transport, and vesicle shedding*. J Am Chem Soc, 2007. **129**(47): p. 14759-66.
36. Fretz, M.M. and G. Storm, *TAT-peptide modified liposomes: preparation, characterization, and cellular interaction*. Methods Mol Biol, 2010. **605**: p. 349-59.
37. Torchilin, V.P., et al., *TAT peptide on the surface of liposomes affords their efficient intracellular delivery even at low temperature and in the presence of metabolic inhibitors*. Proc Natl Acad Sci U S A, 2001. **98**(15): p. 8786-91.
38. Torchilin, V.P. and T.S. Levchenko, *TAT-liposomes: a novel intracellular drug carrier*. Curr Protein Pept Sci, 2003. **4**(2): p. 133-40.
39. Torchilin, V.P., *Recent approaches to intracellular delivery of drugs and DNA and organelle targeting*. Annu Rev Biomed Eng, 2006. **8**: p. 343-75.
40. Berry, C.C., *Intracellular delivery of nanoparticles via the HIV-1 tat peptide*. Nanomed, 2008. **3**(3): p. 357-65.
41. Rothbard, J.B., et al., *Arginine-rich molecular transporters for drug delivery: role of backbone spacing in cellular uptake*. J Med Chem, 2002. **45**(17): p. 3612-8.

7. References

42. Tunnemann, G., et al., *Live-cell analysis of cell penetration ability and toxicity of oligo-arginines*. J Pept Sci, 2008. **14**(4): p. 469-76.
43. Wadia, J.S., R.V. Stan, and S.F. Dowdy, *Transducible TAT-HA fusogenic peptide enhances escape of TAT-fusion proteins after lipid raft macropinocytosis*. Nat Med, 2004. **10**(3): p. 310-5.
44. Vives, E., P. Brodin, and B. Lebleu, *A truncated HIV-1 Tat protein basic domain rapidly translocates through the plasma membrane and accumulates in the cell nucleus*. J Biol Chem, 1997. **272**(25): p. 16010-7.
45. Richard, J.P., et al., *Cellular uptake of unconjugated TAT peptide involves clathrin-dependent endocytosis and heparan sulfate receptors*. J Biol Chem, 2005. **280**(15): p. 15300-6.
46. Potocky, T.B., A.K. Menon, and S.H. Gellman, *Cytoplasmic and nuclear delivery of a TAT-derived peptide and a beta-peptide after endocytic uptake into HeLa cells*. J Biol Chem, 2003. **278**(50): p. 50188-94.
47. Terrone, D., et al., *Penetratin and related cell-penetrating cationic peptides can translocate across lipid bilayers in the presence of a transbilayer potential*. Biochemistry, 2003. **42**(47): p. 13787-99.
48. Vogel, B.E., et al., *A novel integrin specificity exemplified by binding of the alpha v beta 5 integrin to the basic domain of the HIV Tat protein and vitronectin*. J Cell Biol, 1993. **121**(2): p. 461-8.
49. Derossi, D., et al., *Cell internalization of the third helix of the Antennapedia homeodomain is receptor-independent*. J Biol Chem, 1996. **271**(30): p. 18188-93.
50. Ziegler, A., et al., *The cationic cell-penetrating peptide CPP(TAT) derived from the HIV-1 protein TAT is rapidly transported into living fibroblasts: optical, biophysical, and metabolic evidence*. Biochemistry, 2005. **44**(1): p. 138-48.
51. Ter-Avetisyan, G., et al., *Cell entry of arginine-rich peptides is independent of endocytosis*. J Biol Chem, 2009. **284**(6): p. 3370-8.
52. Marshak, D.R., T.J. Lukas, and D.M. Watterson, *Drug-protein interactions: binding of chlorpromazine to calmodulin, calmodulin fragments, and related calcium binding proteins*. Biochemistry, 1985. **24**(1): p. 144-50.
53. Tiriveedhi, V. and P. Butko, *A fluorescence spectroscopy study on the interactions of the TAT-PTD peptide with model lipid membranes*. Biochemistry, 2007. **46**(12): p. 3888-95.
54. Ziegler, A., et al., *Protein transduction domains of HIV-1 and SIV TAT interact with charged lipid vesicles. Binding mechanism and thermodynamic analysis*. Biochemistry, 2003. **42**(30): p. 9185-94.

7. References

55. Shaw, J.E., et al., *Cationic peptide-induced remodelling of model membranes: direct visualization by in situ atomic force microscopy*. J Struct Biol, 2008. **162**(1): p. 121-38.
56. Thoren, P.E., et al., *Membrane binding and translocation of cell-penetrating peptides*. Biochemistry, 2004. **43**(12): p. 3471-89.
57. Bonomo, R.A., *Multiple antibiotic-resistant bacteria in long-term-care facilities: An emerging problem in the practice of infectious diseases*. Clin Infect Dis, 2000. **31**(6): p. 1414-22.
58. Matsuzaki, K., *Why and how are peptide-lipid interactions utilized for self-defense? Magainins and tachyplesins as archetypes*. Biochim Biophys Acta, 1999. **1462**(1-2): p. 1-10.
59. Hancock, R.E. and H.G. Sahl, *Antimicrobial and host-defense peptides as new anti-infective therapeutic strategies*. Nat Biotechnol, 2006. **24**(12): p. 1551-7.
60. Andra, J. and M. Leippe, *Candidacidal activity of shortened synthetic analogs of amoebapores and NK-lysin*. Med Microbiol Immunol, 1999. **188**(3): p. 117-24.
61. Schroder-Borm, H., et al., *Molecular basis for membrane selectivity of NK-2, a potent peptide antibiotic derived from NK-lysin*. Biochim Biophys Acta, 2003. **1612**(2): p. 164-71.
62. Andra, J., et al., *Rationale for the design of shortened derivatives of the NK-lysin-derived antimicrobial peptide NK-2 with improved activity against Gram-negative pathogens*. J Biol Chem, 2007. **282**(20): p. 14719-28.
63. van Meer, G., D.R. Voelker, and G.W. Feigenson, *Membrane lipids: where they are and how they behave*. Nat Rev Mol Cell Biol, 2008. **9**(2): p. 112-24.
64. Gorter, E. and F. Grendel, *On Bimolecular Layers of Lipoids on the Chromocytes of the Blood*. J Exp Med, 1925. **41**(4): p. 439-443.
65. Singer, S.J. and G.L. Nicolson, *The fluid mosaic model of the structure of cell membranes*. Science, 1972. **175**(23): p. 720-31.
66. Sackmann, E., *Thermo-elasticity and adhesion as regulators of cell membrane architecture and function*. J. Phys.: Condens. Matter, 2006. **18**: p. R785–R825.
67. Alberts, B., Johnson, A., Lewis, J., Raff, M., Roberts, K., Walter, P., *Molecular Biology of the Cell*. 4th ed. 2002, NY, USA: Garland Science. 583-593.
68. Tocanne, J.F., et al., *Lipid domains and lipid/protein interactions in biological membranes*. Chem Phys Lipids, 1994. **73**(1-2): p. 139-58.

7. References

69. Devaux, P.F., *Static and dynamic lipid asymmetry in cell membranes*. Biochemistry, 1991. **30**(5): p. 1163-73.
70. H. Hauser, G.P., *The structure of biological membranes*. second edition ed. Lipid Structure, ed. P.L.Y. ed. 2002, CRC Press, USA: Ph. L. Yeagle ed. 1-52.
71. Muller, P. and A. Herrmann, *Rapid transbilayer movement of spin-labeled steroids in human erythrocytes and in liposomes*. Biophys J, 2002. **82**(3): p. 1418-28.
72. Israelachvili, J.N., *Intermolecular and surface forces*. second edition ed, ed. A.P. Limited. 1992, London, UK.
73. Dan, N. and S.A. Safran, *Effect of lipid characteristics on the structure of transmembrane proteins*. Biophys J, 1998. **75**(3): p. 1410-4.
74. Hubner, S., et al., *Enhancement of phosphoinositide 3-kinase (PI 3-kinase) activity by membrane curvature and inositol-phospholipid-binding peptides*. Eur J Biochem, 1998. **258**(2): p. 846-53.
75. Burack, W.R., et al., *Changes in vesicle morphology induced by lateral phase separation modulate phospholipase A2 activity*. Biochemistry, 1997. **36**(34): p. 10551-7.
76. Huttner, W.B. and J. Zimmerberg, *Implications of lipid microdomains for membrane curvature, budding and fission*. Curr Opin Cell Biol, 2001. **13**(4): p. 478-84.
77. Nikaido, H., *Molecular basis of bacterial outer membrane permeability revisited*. Microbiol Mol Biol Rev, 2003. **67**(4): p. 593-656.
78. Andra, J., et al., *Enhancement of endotoxin neutralization by coupling of a C12-alkyl chain to a lactoferricin-derived peptide*. Biochem J, 2005. **385**(Pt 1): p. 135-43.
79. Klösgen, B., *Conformation of fluid lipid membranes in lipid bilayers. Structure and interaction*, J.K.a.T.G. eds, Editor. 2001, Springer Verlag, Germany.
80. Tang, Q. and M. Edidin, *Lowering the barriers to random walks on the cell surface*. Biophys J, 2003. **84**(1): p. 400-7.
81. Schutz, G.J., et al., *Single molecule microscopy of biomembranes (review)*. Mol Membr Biol, 2000. **17**(1): p. 17-29.
82. Schwille, P., J. Korlach, and W.W. Webb, *Fluorescence correlation spectroscopy with single-molecule sensitivity on cell and model membranes*. Cytometry, 1999. **36**(3): p. 176-82.

7. References

83. Sekar, R.B. and A. Periasamy, *Fluorescence resonance energy transfer (FRET) microscopy imaging of live cell protein localizations*. J Cell Biol, 2003. **160**(5): p. 629-33.
84. Gawrisch, K., *The dynamics of membrane lipids in The structure of biological membranes*. 2005, USA: Philip L. Eagle.
85. Heimburg, T., *Thermal Biophysics of Membranes*. 2007, Berlin: Wiley-VCH.
86. Marsh, D., *General features of phospholipid phase transitions*. Chem Phys Lipids, 1991. **57**(2-3): p. 109-20.
87. Mouritsen, O.G. and K. Jorgensen, *Dynamical order and disorder in lipid bilayers*. Chem Phys Lipids, 1994. **73**(1-2): p. 3-25.
88. Veatch, S.L. and S.L. Keller, *Organization in lipid membranes containing cholesterol*. Phys Rev Lett, 2002. **89**(26): p. 268101.
89. Rog, T., et al., *Ordering effects of cholesterol and its analogues*. Biochim Biophys Acta, 2009. **1788**(1): p. 97-121.
90. Bangham, A.D., M.M. Standish, and J.C. Watkins, *Diffusion of univalent ions across the lamellae of swollen phospholipids*. J Mol Biol, 1965. **13**(1): p. 238-52.
91. Angelova, M.I.a.D., D. S., *Liposome electroformation*. Faraday Discuss.Chem. Soc. , 1986. **81**: p. 303-311.
92. Rodriguez, N., F. Pincet, and S. Cribier, *Giant vesicles formed by gentle hydration and electroformation: a comparison by fluorescence microscopy*. Colloids Surf B Biointerfaces, 2005. **42**(2): p. 125-30.
93. Menger, F.M. and J.S. Keiper, *Chemistry and physics of giant vesicles as biomembrane models*. Curr Opin Chem Biol, 1998. **2**(6): p. 726-32.
94. Menger, F.M., Angelova, M. I., *Giant Vesicles: Imitating the Cytological Processes of Cell Membranes*. Acc. Chem. Res., 1998. **31**: p. 789-797.
95. Dimova, R., Aranda, S., Bezlyepkina, N., Nikolov, V., Riske, K., and Lipowsky, R., *A practical guide to giant vesicles. Probing the membrane nanoregime via optical microscopy*. J. Phys.: Condens. Matter, 2006. **18**: p. 1151-1176.
96. Noireaux, V. and A. Libchaber, *A vesicle bioreactor as a step toward an artificial cell assembly*. Proc Natl Acad Sci U S A, 2004. **101**(51): p. 17669-74.
97. Montes, L.R., et al., *Giant unilamellar vesicles electroformed from native membranes and organic lipid mixtures under physiological conditions*. Biophys J, 2007. **93**(10): p. 3548-54.

7. References

98. Shimanouchi, T., H. Umakoshi, and R. Kuboi, *Kinetic study on giant vesicle formation with electroformation method.* Langmuir, 2009. **25**(9): p. 4835-40.
99. Bucher, P.F., A.; Luisi, P. L.; Oberholzer, T.; Walde, P., *Giant Vesicles as Biochemical Compartments: The Use of Microinjection Techniques.* Langmuir 1998. **14**: p. 2712-2721.
100. Deshayes, S., Morris, M.C., Divita, G., Heitz, F., *Interactions of Cell-Penetrating Peptides with Model Membranes* in *Handbook of Cell Penetrating Peptides.* 2006, Taylor & Francis Group, LLC
101. Veatch, S.L. and S.L. Keller, *Separation of liquid phases in giant vesicles of ternary mixtures of phospholipids and cholesterol.* Biophys J, 2003. **85**(5): p. 3074-83.
102. Scherfeld, D., N. Kahya, and P. Schwille, *Lipid dynamics and domain formation in model membranes composed of ternary mixtures of unsaturated and saturated phosphatidylcholines and cholesterol.* Biophys J, 2003. **85**(6): p. 3758-68.
103. Valeur, B., *Molecular Fluorescence. Principles and Applications.* 2001: Wiley CH. 354-355.
104. Murphy, B.M., *Fundamentals of light microscopy and electronic imaging.* 2001: John Willey & Sons.
105. Webb, D.S.a.W., *Background Rejection and Signal-to-Noise Optimization in the Confocal and Alternative Fluorescence Microscopes.* Applied Optics, 1994. **33**: p. 603-610.
106. Lemasters, J.J., et al., *Measurement of electrical potential, pH, and free calcium ion concentration in mitochondria of living cells by laser scanning confocal microscopy.* Methods Enzymol, 1995. **260**: p. 428-44.
107. Barak, L.S. and W.W. Webb, *Diffusion of low density lipoprotein-receptor complex on human fibroblasts.* J Cell Biol, 1982. **95**(3): p. 846-52.
108. Saxton, M.J. and K. Jacobson, *Single-particle tracking: applications to membrane dynamics.* Annu Rev Biophys Biomol Struct, 1997. **26**: p. 373-99.
109. Siebrasse, J.P., Kubitscheck, U., *Single Molecule Tracking for Studying Nucleocytoplasmic Transport and Intranuclear Dynamics,* in *The Nucleus: Chromatin, Transcription, Envelope, Proteins, Dynamics, and Imaging* 2009, Humana Press. p. 343-361.
110. Kubitscheck, U., et al., *Nuclear transport of single molecules: dwell times at the nuclear pore complex.* J Cell Biol, 2005. **168**(2): p. 233-43.

7. References

111. Grunwald, D., et al., *Intranuclear binding kinetics and mobility of single native U1 snRNP particles in living cells*. Mol Biol Cell, 2006. **17**(12): p. 5017-27.
112. Kubitscheck, U., Kues, T., Hoekstra, A., *Visualization and tracking of single molecules within cells*. GIT Laboratory journal, 2002. **6**(6): p. 293-295
113. Kahya, N., et al., *Probing lipid mobility of raft-exhibiting model membranes by fluorescence correlation spectroscopy*. J Biol Chem, 2003. **278**(30): p. 28109-15.
114. Abramoff, M.D., Magelhaes, P. J., and Ram, S. J. , *Image Processing with ImageJ*. Biophot. Int., 2004. **11**: p. 36-42.
115. Crank, J., *The Mathematics of Diffusion*. 1975, Oxford, U.K.: Clarendon Press.
116. Shental-Bechor, D., T. Haliloglu, and N. Ben-Tal, *Interactions of cationic-hydrophobic peptides with lipid bilayers: a Monte Carlo simulation method*. Biophys J, 2007. **93**(6): p. 1858-71.
117. Kessel, A., et al., *Interactions of hydrophobic peptides with lipid bilayers: Monte Carlo simulations with M2delta*. Biophys J, 2003. **85**(6): p. 3431-44.
118. Schmidt, T., Schütz, G. J., Baumgartner,W., Gruber, H. J., and Schindler, H., *Characterization of photophysics and mobility of single molecules in a fluid lipid membrane*. J. Chem. Phys., 1995. **99**: p. 17662-17668.
119. Murcia, M.J., S. Garg, and C.A. Naumann, *Single-molecule fluorescence microscopy to determine phospholipid lateral diffusion*. Methods Mol Biol, 2007. **400**: p. 277-94.
120. Petrache, H.I., Harries, D., Parsegian, V. A., *Alteration of lipid membrane rigidity by cholesterol and its metabolic precursors*. Macromol. Symp., 2005. **219**: p. 39-50.
121. Ciobanasu, C., et al., *Cell-penetrating HIV1 TAT peptides float on model lipid bilayers*. Biochemistry, 2009. **48**(22): p. 4728-37.
122. Ciobanasu, C., Siebrasse, J. P. and Kubitscheck, U., *Cell penetrating HIV1 TAT peptides can generate pores in model membranes*. Biophysical Jurnal, 2010. **99**(1): p. 153-162
123. Persky, B. and M.J. Hendrix, *Artificial matrix barriers: a diffusion study utilizing dextrans and microspheres*. Anat Rec, 1990. **228**(1): p. 15-22.
124. Yao, Y. and A.M. Lenhoff, *Determination of pore size distributions of porous chromatographic adsorbents by inverse size-exclusion chromatography*. J Chromatogr A, 2004. **1037**(1-2): p. 273-82.

7. References

125. Ambroggio, E.E., et al., *Direct visualization of membrane leakage induced by the antibiotic peptides: maculatin, citropin, and aurein*. Biophys J, 2005. **89**(3): p. 1874-81.
126. Birner, R., et al., *Roles of phosphatidylethanolamine and of its several biosynthetic pathways in *Saccharomyces cerevisiae**. Mol Biol Cell, 2001. **12**(4): p. 997-1007.
127. Opekarova, M., I. Robl, and W. Tanner, *Phosphatidyl ethanolamine is essential for targeting the arginine transporter Can1p to the plasma membrane of yeast*. Biochim Biophys Acta, 2002. **1564**(1): p. 9-13.
128. Kearns, D.B., J. Robinson, and L.J. Shimkets, *Pseudomonas aeruginosa exhibits directed twitching motility up phosphatidylethanolamine gradients*. J Bacteriol, 2001. **183**(2): p. 763-7.
129. Cronan, J.E., *Bacterial membrane lipids: where do we stand?* Annu Rev Microbiol, 2003. **57**: p. 203-24.
130. Chaudhary, A., et al., *Evaluation of glucose sensitive affinity binding assay entrapped in fluorescent dissolved-core alginate microspheres*. Biotechnol Bioeng, 2009. **104**(6): p. 1075-85.
131. Leekumjorn, S. and A.K. Sum, *Molecular simulation study of structural and dynamic properties of mixed DPPC/DPPE bilayers*. Biophys J, 2006. **90**(11): p. 3951-65.
132. Boggs, J.M., *Lipid intermolecular hydrogen bonding: influence on structural organization and membrane function*. Biochim Biophys Acta, 1987. **906**(3): p. 353-404.
133. Berg, H.C., *Random Walks in Biology*. 1983, New Jersey: Princeton University Press.
134. Lide, D.R., *CRC Handbook of Chemistry and Physics, 85th Edition*, ed. D.R. Lide. 2004, Maryland, USA CRC Press.
135. Gordon-Grossman, M., et al., *A combined pulse EPR and Monte Carlo simulation study provides molecular insight on peptide-membrane interactions*. J Phys Chem B, 2009. **113**(38): p. 12687-95.
136. Petrache, H.I., et al., *Salt screening and specific ion adsorption determine neutral-lipid membrane interactions*. Proc Natl Acad Sci U S A, 2006. **103**(21): p. 7982-7.
137. Pabst, G., et al., *Rigidification of neutral lipid bilayers in the presence of salts*. Biophys J, 2007. **93**(8): p. 2688-96.

7. References

138. Rothbard, J.B., T.C. Jessop, and P.A. Wender, *Adaptive translocation: the role of hydrogen bonding and membrane potential in the uptake of guanidinium-rich transporters into cells*. Adv Drug Deliv Rev, 2005. **57**(4): p. 495-504.
139. Sakai, N., et al., *Direct observation of anion-mediated translocation of fluorescent oligoarginine carriers into and across bulk liquid and anionic bilayer membranes*. Chembiochem, 2005. **6**(1): p. 114-22.
140. Springs, B., Haake, P., *Equilibrium-constants for association of guanidinium and ammonium-ions with oxyanions—effect of changing basicity of oxyanion*. Bioorg. Chem., 1977. **6**: p. 181–190.
141. Onda, M., Yoshihara,K., Koyano,H., Ariga,K., and and T. Kunitake, *Molecular Recognition of Nucleotides by the Guanidinium Unitat the Surface of Aqueous Micelles and Bilayers. A Comparison of Microscopic and Macroscopic Interfaces*. J. Am. Chem. Soc., 1996. **118**: p. 8524-8530.
142. Wender, P.A., et al., *The design of guanidinium-rich transporters and their internalization mechanisms*. Adv Drug Deliv Rev, 2008. **60**(4-5): p. 452-72.
143. Willumeit, R., et al., *Structural rearrangement of model membranes by the peptide antibiotic NK-2*. Biochim Biophys Acta, 2005. **1669**(2): p. 125-34.

Curriculum vitae and list of publications

Personal details:

Name	Vasilica-Corina Ciobanaru
Date of birth	-
Place of birth	Roman, Romania

Education:

April 2007-	PhD student at Institute for Physical and Theoretical Chemistry,
April 2010	Rheinische Friedrich-Wilhelms University Bonn, Germany
	research assistant at Department of Natural and Synthetic Polymers,
November 2003-	Faculty of Chemical Engineering, "Gh. Asachi" Technical
March 2007	University, Iasi, Romania
	M.Sci. in Chemistry and Biochemistry of Heterocyclic Compounds,
July 2003	Faculty of Chemistry „Al. I. Cuza” University, Iasi, Romania
	B.Sci., Chemistry-Physics, Faculty of Chemistry „Al.I.Cuza”
July 2001	University, Iasi, Romania
	High School “Roman-Voda”, Chemistry-Biology, Roman, Romania
June 1997	

List of publications:

Corina Ciobanaru, Enno Harms, Gisela Tünnemann, M. Cristina Cardoso and Ulrich Kubitscheck, *Cell-penetrating HIV1 TAT peptides float on model lipid bilayers*, Biochemistry, 2009, **48** (22), p. 4728–4737

Corina Ciobanaru, Jan Peter Siebrasse and Ulrich Kubitscheck, *Cell penetrating HIV1 TAT peptides can form pores in model membranes*, Biophysical Journal, 2010, **99** (1), p. 153-162

Corina Ciobanaru, Agnieszka Rzeszutek, Vincent Raussens, Ulrich Kubitscheck and Regine Willumeit, *Interaction of antimicrobial peptide NKCS with the model membrane of Escherichia coli*, in preparation

List of figures

Figure 1.1: Pathways of active entry into cells.....	11
Figure 1.2: Translocation mediated by the formation of inverted micelles.....	13
Figure 1.3: Models proposed for the membrane permeation of membrane-active antimicrobial peptides.....	14
Figure 1.4: Secondary structure of TAT peptide.....	15
Figure 1.5: The secondary structure of NKCS.....	21
Figure 1.6: The secondary structure of NKCS-[15-27].....	22
Figure 1.7: A schematic representation of plasma membrane.....	23
Figure 1.8: Examples of membrane lipids.....	25
Figure 1.9: Illustration of the parameter p on lipid aggregate structures.....	26
Figure 1.10: Lipid structures.....	27
Figure 1.11: Lipid bilayer phases.....	29
Figure 1.12: Principle of lipid swelling.....	32
Figure 2.1: A cartoon of the electroformation chamber.....	37
Figure 2.2: Confocal images of GUVs labelled by Bodipy-PC.....	38
Figure 2.3: Principle of confocal microscopy.....	39
Figure 2.4: Setup for single molecule fluorescence microscope.....	42
Figure 2.5: Nanolocalization of single molecules.....	44
Figure 2.6: MSD as a function of time.....	46
Figure 2.7: The model of membrane structure employed in Monte Carlo simulations....	50
Figure 3.1: Single TR-DHPE molecules diffusing within the GUV membrane.....	54
Figure 3.2: TR-DHPE diffusion on neutral and anionic GUVs.....	55
Figure 3.3: Analysis of TR-DHPE diffusion on neutral and anionic GUVs.....	57
Figure 3.4: Time series of TAT peptide interaction with anionic GUVs in glucose.....	59
Figure 3.5: Single R-TAT peptide on the GUV surface.....	60
Figure 3.6: MSD plot of R-TAT diffusion on neutral and anionic GUVs.....	61

List of figures

Figure 3.7: Analysis of R-TAT diffusion on neutral and anionic GUVs	63
Figure 3.8: Confocal images of GUVs labelled by R-TAT.....	63
Figure 3.9: Distribution of the trajectory lengths on neutral and anionic GUVs.....	64
Figure 3.10: Distance distribution of TAT peptide from the membrane midplane.....	66
Figure 3.11: Interaction of TAT peptides with neutral model membranes.....	69
Figure 3.12: Imaging of TAT peptide-membrane interaction with neutral GUVs	70
Figure 3.13: Mobility of lipid tracers in anionic model membranes.....	72
Figure 3.14: Interaction of TAT peptides with anionic model membranes.....	73
Figure 3.15: Confocal images of GUVs (40 mol% PS) and AF-TAT.....	74
Figure 3.16: The histograms for AF-TAT diffusion on anionic GUVs	75
Figure 3.17: Pore formation by TAT peptides in GUVs containing 40 mol % PS.....	76
Figure 3.18: Internalization of TAT peptide and efflux of tracers	76
Figure 3.19: Control experiments for photobleaching.....	77
Figure 3.20: The distance distribution of TAT in membranes containing anionic lipids..	78
Figure 3.21: Inner conformations versus ratio of anionic lipids.....	78
Figure 3.22: Mobility of lipid tracers on model membranes containing PE.....	82
Figure 3.23: Interaction of TAT peptides with model membranes containing PE.....	83
Figure 3.24: Fluorescence intensity of Alexa-Fluor 647 in water and sugars.....	84
Figure 3.25: Pore formation of TAT peptides in membranes containing 30 mol % PE... <td>85</td>	85
Figure 3.26: Internalization of TAT peptide (A) and efflux of tracers (B) in GUV with 30 mol % PE.....	85
Figure 3.27: Interaction of TAT peptides with model membranes containing PE.....	86
Figure 3.28: Interaction of B-TAT peptides with model membranes.....	87
Figure 3.29: Plots of two-dimensional diffusion trajectory of the tracer TR-DHPE and AF-TAT peptide.....	88
Figure 3.30: The inverted hexagonal diffraction pattern of DOPE and with TAT CPP....	90
Figure 3.31: Analysis of TR-DHPE diffusion in neutral and anionic GUVs.....	92
Figure 3.32: TAT peptide interaction with GUVs.....	93

List of figures

Figure 3.33: Internalization of TAT peptide and Lucifer Yellow in GUVs	95
Figure 3.34: Internalization of TAT peptide and FITC-dextran 4 kDa in GUVs	95
Figure 3.35: Internalization of TAT peptide and tracers in GUV.....	95
Figure 3.36: Pore formation in neutral membranes in100 mM NaCl.....	97
Figure 3.37: Internalization of TAT peptide and efflux of tracers in neutral GUVs.....	98
Figure 3.38: Internalization of TAT peptide and efflux of tracers in anionic GUVs.....	98
Figure 3.39: Internalization of TAT peptide and efflux of tracers in 100 mM NaCl.....	99
Figure 3.40: Pore formation in DOPC/DPPC = 80/20 GUV in NaCl 100 mM.....	100
Figure 3.41: Internalization of TAT peptide and AF488 in DOPC/DPPC =50/50.....	100
Figure 3.42: Internalization of TAT peptide in DOPC/DPPS/chol=60/20/20.....	101
Figure 3.43: Analysis of TR-DHPE diffusion on neutral and anionic GUVs.....	103
Figure 3.44: Analysis of TR-DHPE diffusion on neutral and anionic GUVs.....	105
Figure 3.45: Distance distribution of TAT peptide from the membrane midplane for different concentration of NaCl solution.....	106
Figure 3.46: Dependence of binding energy of the peptide on salt concentration.....	106
Figure 3.47: Hydrophilicity of TAT peptide.....	109
Figure 3.48: Representative associations of TAT based guanidinium transporter with anionic cell membrane constituents.....	110
Figure 3.49: Schematic associations of TAT peptide with membrane surface in a. glucose solution and b. glucose solution containing 100 mM NaCl.....	111
Figure 4.1: Translocation and pore formation by NKCS peptide in GUVs.....	115
Figure 4.2: Jump distance analysis for TR-DHPE and NKCS in GUVs prepared from DOPC/POPG and DOPC/POPE.....	118

List of tables

Table 1.1: Comparison of the amino acid sequences of the antibiotic peptides NK-2 and 3 derivatives used in this study	21
Table 1.2: Properties of the peptides.....	22
Table 1.3: Approximate lipid composition of different cell membranes.....	24
Table 3.1: Composition of giant unilamellar vesicles (GUVs).....	53
Table 3.2: TR-DHPE mobility within GUVs.....	55
Table 3.3: DiI-C ₁₈ mobility within GUVs.....	56
Table 3.4: R-TAT peptide mobility on GUVs.....	62
Table 3.5: AF-TAT mobility on GUVs.....	71
Table 3.6: Composition of giant unilamellar vesicles (GUVs).....	73
Table 3.7: Composition of membranes containing PE.....	81
Table 3.8: AF-TAT peptide mobility on PE containing GUVs.....	87
Table 3.9: TR-DHPE mobility within GUVs in 100 mM NaCl.....	92
Table 3.10: TR-DHPE mobility within GUVs in a solution containing 2 µM B-TAT and 100 mM NaCl.....	104
Table 4.1: TR-DHPE mobility within GUVs.....	113
Table 4.2: Effects of NKCS peptides on GUVs loaded with different tracers.....	114
Table 4.3: NKCS peptides mobility on GUVs.....	116
Table 4.4: TR-DHPE mobility on GUVs incubated with 2 µM unlabelled peptides.....	117